CONTROLLED LAGRANGIAN PARTICLE TRACKING: ANALYZING THE PREDICTABILITY OF TRAJECTORIES OF AUTONOMOUS AGENTS IN OCEAN FLOWS

A Dissertation
Presented to
The Academic Faculty

By

Klementyna Szwaykowska

In Partial Fulfillment
of the Requirements for the Degree
Doctor of Philosophy
in
Electrical and Computer Engineering

School of Electrical and Computer Engineering
Georgia Institute of Technology
December 2013

CONTROLLED LAGRANGIAN PARTICLE TRACKING: ANALYZING THE PREDICTABILITY OF TRAJECTORIES OF AUTONOMOUS AGENTS IN OCEAN FLOWS

Approved by:

Dr. Fumin Zhang, Advisor
Assoc. Professor, School of ECE
Georgia Institute of Technology

Dr. Catherine Edwards
Asst. Professor
Skidaway Institute of Oceanography

Dr. Erik Verriest
Professor, School of ECE
Georgia Institute of Technology

Dr. Chin-Hui Lee
Professor, School of ECE
Georgia Institute of Technology

Dr. Magnus Egerstedt
Professor, School of ECE
Georgia Institute of Technology

Date Approved: November 2013

ACKNOWLEDGMENTS

This thesis would not have been possible without the help and support of the many wonderful people I have had the privilege of meeting and working with over the course of my graduate studies. I would like to take this opportunity to thank them, though it would be impossible to list them all by name.

A great deal of thanks, first and foremost, goes to my graduate advisor Dr. Fumin Zhang, who introduced me to the fascinating world of underwater robotics, which so perfectly blends my twin interests in physics and control. His help and advice have been invaluable to me, and his unwavering enthusiasm has guided and inspired me throughout my studies here at Georgia Tech.

I would like to thanks my thesis committee members: Dr. Verriest, Dr. Egerstedt, Dr. Edwards, and Dr. Lee. Thank you for your time and valuable suggestions.

I would especially like to thank Dr. Edwards, who has been a real mentor and friend to me over the years. Her encouragement has meant a lot to me and her advice has never failed me. When disaster struck (as it sometimes did) during our field experiments, she was the guiding voice at the other end of the phone or email line in the darkest hours of the night, telling us in a calm and reasonable way how to handle situations that I had never anticipated (remoras, amorous sea-turtles, mysterious error codes, etc.).

My labmate and collaborator Dongsik Chang also deserves a lot of thanks for handling software issues and piloting the gliders during the hardest conditions. Thanks is also due to the wonderful people at Webb technical support, who fielded our questions day or night, and all our collaborators at Skidaway and UNC.

Finally, from the bottom of my heart, I would like to thank my parents, Q and Alex, and all my friends from Arizona, California, and Georgia (especially the PM and my labmates here at Georgia Tech). You guys have always supported me and made me feel like I knew what I was doing.

TABLE OF CONTENTS

LIST OF TABLES

LIST OF FIGURES

SUMMARY

Use of model-based path planning and navigation is a common strategy in mobile robotics. However, navigation performance may degrade in complex, time-varying environments under model uncertainty because of loss of prediction ability for the robot state over time. Exploration and monitoring of ocean regions using autonomous marine robots is a prime example of an application where use of environmental models can have great benefits in navigation capability. Yet, in spite of recent improvements in ocean modeling, errors in model-based flow forecasts can still significantly affect the accuracy of predictions of robot positions over time, leading to impaired path-following performance. In developing new autonomous navigation strategies, it is important to have a quantitative understanding of error in predicted robot position under different flow conditions and control strategies.

The main contributions of this thesis include development of an analytical model for the growth of error in predicted robot position over time and theoretical derivation of bounds on the error growth, where error can be attributed to drift caused by unmodeled components of ocean flow. Unlike most previous works, this work explicitly includes spatial structure of unmodeled flow components in the proposed error growth model. It is shown that, for a robot operating under flow-canceling control in a static flow field with stochastic errors in flow values returned at ocean model gridpoints, the error growth is initially rapid, but slows when it reaches a value of approximately twice the ocean model gridsize. Theoretical values for mean and variance of error over time under a station-keeping feedback control strategy and time-varying flow fields are computed. Growth of error in predicted vehicle position is modeled for ocean models whose flow forecasts include errors with large spatial scales. Results are verified using data from several extended field deployments of Slocum autonomous underwater gliders, in Monterey Bay, CA in 2006, and in Long Bay, SC in 2012 and 2013.

CHAPTER 1

INTRODUCTION

The ocean is the last great frontier remaining on Earth. In an age when travel to the most remote regions on the planet is made possible (and in many cases easy) by technology, and the entire surface of the earth is covered by a global network of imaging satellites, the world's oceans remain, to a large extent, forbidding and impenetrable. And yet, the ocean is essential to our lives: it serves as a source of food, a highway for trade, and an important factor in determining global weather and climate. Understanding marine processes is crucial in a wide range of applications, from fisheries management to wildlife conservation to marine search and rescue and weather and climate forecasting. Mobile sensor networks may be very effectively used for exploration and monitoring of hostile environments like the ocean. Use of mobile sensors to better understand complex physical, chemical, and biological marine processes may perhaps be considered one of the most exciting challenges for field robotics and control in the coming years. This goal, however, requires overcoming a number of technical challenges, including effective motion planning and navigation in unstructured, time-varying flows.

1.1 Statement of the Problem

In recent years, improvements in computing power have led to the creation of increasingly accurate and high-resolution numerical ocean general circulation models (OGCMs), which can be used to study various physical ocean processes. Even so, missing physics, unstable dynamics, unknown boundary conditions, and numerical errors often lead to large errors in the OGCM output data [1]. The modeling performance of OGCMs can be significantly improved by assimilation of field measurements into the models [2, 3].

Mobile sampling networks of autonomous vehicles are particularly well-suited to this task. Using a small fleet of autonomous vehicles, it is possible to track an evolving flow

feature (such as an eddy), that would otherwise require a very large, dense array of traditional, moored platforms to sample at an equivalent resolution [4]. It is, furthermore, relatively easy and inexpensive to scale the number of deployed vehicles to improve sampling resolution and coverage [5].

Slow-moving vehicles are commonly utilized in ocean monitoring missions to minimize energy expenditure and extend mission duration; thus drift from ambient flow becomes an important component of the vehicle dynamics. OGCMs can therefore be highly useful in path-planning and navigation of autonomous vehicles in the ocean [6, 7, 8, 9]. In path-planning applications, use of predictive models allows vehicle operators to find optimal trajectories by taking advantage of spatial and temporal variations in the flow dynamics. In navigation of underwater vehicles, subsurface localization may be an issue, as signals from the global positioning system (GPS) cannot penetrate below the surface of the water; vehicles therefore frequently rely on dead-reckoning to follow a desired trajectory while underwater. Predictive models can be used to add flow corrections in the dead-reckoned positions of vehicles, allowing for better path-following performance.

Uncertainty in the environmental model limits the ability to accurately predict vehicle positions over time, and thus leads to degraded performance in both path-planning and navigation applications. This error may be decreased by shortening the duration of dives for underwater navigation [10]. However, one very naturally desires to use as long a dive duration as possible: this allows maximal use of mission time for data collection and pursuit of mission goals; furthermore, there is the additional motivation that while on the surface, the vehicle runs the risk of colliding with a boat [8, 10] and is subject to wind drift [11, 12]. Therefore, given an ocean model with known prediction accuracy, it is important to know bounds on the resulting error in predicted vehicle position over time. The main question addressed in this dissertation is: given a known model for error in the forecast ocean flow, what is the resulting error in predicted vehicle position over time under different ambient flow conditions and control strategies?

1.2 Contributions and Outline

In this dissertation, we introduce the concept of controlled Lagrangian particle tracking (CLPT) to model the trajectories of vehicles moving in ocean flows. CLPT is an extension of the existing concept of Lagrangian particle tracking (LPT), used in oceanography to model trajectories of particles passively advected by ocean flows. Typically, the motions of these passive particles are modeled using a Langevin equation, where the particle velocity is given by the superposition of a large-scale "mean" flow velocity and small-scale stochastic turbulence; the "mean" flow is assumed to be known exactly. We add a third velocity component: the controlled through-water velocity of the vehicle. We furthermore note that the mean flow velocity is obtained from an ocean model and may include unknown errors.

The main contribution of this thesis is the development of a theoretical model for error growth in the predicted position of an autonomous vehicle guided by ocean model forecast flow data, given a spatially-varying model for the error in flow estimates. We find a first-order error growth model by finding the first-order Taylor expansion of the error growth dynamics about the modeled vehicle trajectory, and treating the error in the modeled flow as a perturbation of the linearized dynamics. This model is used as the theoretical framework for analyzing growth of error in predicted vehicle position under different flow conditions and control strategies.

We first consider a control strategy known as flow-canceling control. This is perhaps the simplest model-based control strategy that can be implemented on an underwater vehicle over a single extended dive time. The vehicle operates with no position feedback and simply cancels the modeled ocean flow at its current position. We show that, in a static flow field with stochastic errors in flow values at ocean model gridpoints, the error is bounded, and the expected error of this bound as approximately twice the ocean model gridsize.

We extend our results to a transect-following controller, which uses flow-canceling and position-based feedback track a straight-line transect, and to a station-keeping controller, which uses flow cancellation and position-based feedback to guide the vehicle to a desired

station-keeping position and to keep it stationary there. We show that error growth in predicted vehicle position is reduced with use of position-based feedback, and derive bounds on the error growth in the constant-flow case.

We test the validity of our results using numerical simulations and data collected over three field deployments of autonomous underwater vehicles. These deployments were carried out in Monterey Bay, CA, in August of 2006, and in Long Bay, SC, in January-April of 2012 and in February of 2013. The vehicles in the latter two deployments were guided using flow data from predictive ocean models. The observed vehicle trajectories were compared with predicted trajectories from a realistic, three-dimensional simulation of vehicle motion in modeled flow to obtain measurements of position prediction error.

The rest of this dissertation is organized as follows. A review of related work, including Lagrangian particle tracking is given in Chapter 2. The error growth model for CLPT is presented in Chapter 3, where we also describe the flow-canceling, transect-following, and station-keeping controllers. The growth of error in predicted position of a vehicle operating under flow-canceling control is described in Chapter 4. In Chapter 5 we extend these results to the transect-following and station-keeping feedback controller. The field experiments and collected data are described in Chapter 6. Chapter 7 contains some concluding remarks and future research directions.

CHAPTER 2

BACKGROUND

This chapter provides an overview of related work. A brief description of Lagrangian particle tracking is given in Section 2.1. Some existing results on path-planning and navigation using data from predictive ocean flow modes are given in Section 2.2. A brief description of existing state-of-the-art autonomous underwater vehicle technology and its development is given in Section 2.3.

2.1 Lagrangian Particle Tracking

The Lagrangian formulation of fluid dynamics uses the trajectories of infinitesimal particles advected in the flow to give a description of the flow field [13]. This description suggests the idea of using marked "particle-like" objects to map the structure of real flow fields. It is perhaps not surprising, then, that the idea of using particle-like "Lagrangian drifters" to study ocean circulation has been around for hundreds of years. In the mid-eighteenth century, the positions of drogues (small buoys with underwater appendages designed to move with the ambient flow, as illustrated in Figure 1) observed from a fixed station were used to probe the structure of flows [14]. Later, drifters were used to study large-scale circulations by T. W. Fulton, who released bottles (tagged with release date and location) in the North Sea; 502 of the original 2074 bottles were recovered, yielding the first qualitative description of the North Sea circulation [15]. Similar experiments were repeated by O. Krümmel off the Dutch coast in 1904 and by M. Uda in the Northwest Pacific Ocean in 1935 [14, 15]. A later iteration of this idea was demonstrated in the experiments by Stommel in 1949, where aerial photographs of floating paper drift cards were used to study ocean turbulence [15, 16]. Today, the most commonly used drifters are drogues similar to their historic counterparts, but use GPS and satellite communications to measure and report their locations over time.

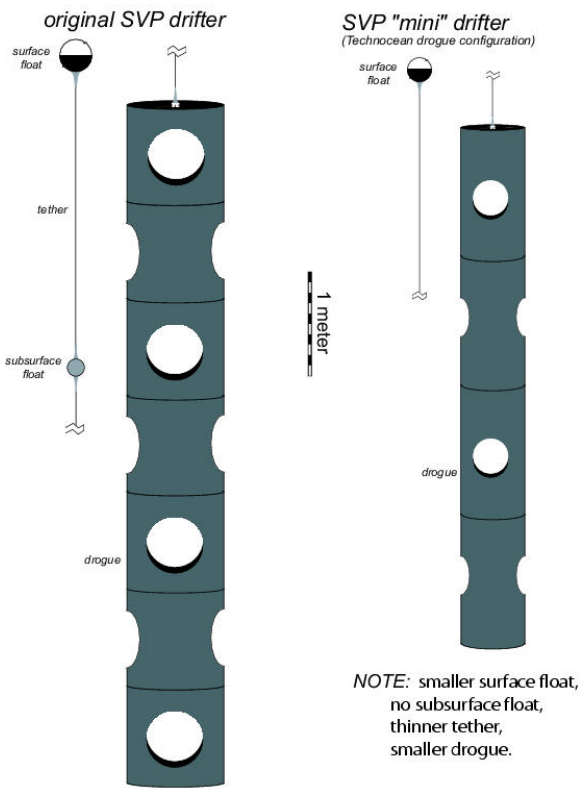

Figure 1: A modern "holey-sock" drogue (image taken from [17]).

With the advent of increasingly accurate ocean models, work is shifting from using trajectories of particles to probe the structure of ocean flows, to the use of ocean flows to predict the motion of various particles; this is what we refer to as Lagrangian particle tracking (LPT). Numerical modeling of Lagrangian particle trajectories, coupled with field observations, can indicate which flow constituents most affect Lagrangian particle distributions, and predict accumulation zones and dwelling times for the tracked particles. Lagrangian schemes have been used to study the dispersion of dissolved pollutants [18], of biological species including algae [19, 20] and fish larvae [21, 22], and of macroscopic objects such as marine debris [23].

The difficulty, historically, has been accurately modeling particle motions in the multitude of turbulent scales seen in ocean/atmospheric flows. Most implementations of LPT assume that there is a clear scale separation between the turbulent motion and large-scale mean flow (although this assumption frequently does not hold in practice [24]). The flow

is then assumed to be a superposition of a stochastic small-scale turbulent flow (termed the "stochastic eddy velocity") and a large-scale, deterministic flow field (the "mean flow"); the goal, then, is to model the overall advection/diffusion behavior of particles in the net flow field through aggregate analysis of particle trajectories.

The effects of small-scale turbulence on particle motion have been well studied. Taylor [25] gives an early estimate of dispersion of particles based on Lagrangian statistics in flow. In Taylor's work, the turbulent scale is assumed to be infinitesimal; the stochastic motions of particles caused by turbulent components in the flow are simulated using a random walk model, that is

$$d\mathbf{x} = \mathbf{F}(\mathbf{x}, t)dt + d\omega,$$

where $\mathbf{F}$ is the mean flow and ω is a driving noise. A more accurate description of turbulent motion is given by the "random flight" model [26, 27, 28], in which the velocity of the particle is modeled as a finite-memory stochastic process

$$d\mathbf{x} = (\mathbf{F}(\mathbf{x}, t) + \nu(t))dt$$

$$d\nu = -A\nu(t)dt + \Lambda d\omega,$$

where A determines the memory length, which characterizes the scale of the turbulence (this model will be discussed at more length in Chapter 3). A third, more sophisticated approach, models particle acceleration as a stochastic process [29]. Griffa [24] gives a good overview of these three models, adapted for oceanographic applications.

The LPT stochastic particle motion models assume that the mean flow is known exactly. In practice, the mean flow is obtained from numerical ocean models, and inaccuracies in the modeled flow data may introduce significant errors in the prediction of particle trajectories. Sources of error in an ocean model include missing physics; inaccuracies in the boundary conditions; unknown variations in local bathymetry; numerical errors solving the ocean model equations; and finite resolution of the model. There are some existing works in oceanographic literature that address these issues. The finite size and mass of the tracked particles may also affect their advection properties. The effects of finite particle size and

mass have been studied, ex. in [30]. Model subgridscale flow variations are discussed in [31] (which also gives a good overview of Lagrangian particle tracking methods). The effects of smoothing the flow field (as by interpolation of a flow field modeled over a discrete grid) are studied in [32].

Our work address the effects of finite grid size and subgridscale structures on the motion of autonomous underwater vehicles operating under feedback control. This problem is related to the drifter studies described in the literature; however, the particles in the proposed work have dynamics which are separate from the ocean model. Their net motion depends both on the ambient flow and on their through-water motion. This adds an interesting new dimension to the problem.

2.2 Model-Aided Navigation of Autonomous Underwater Vehicles

In many practical applications where autonomous control of underwater vehicles is used, the vehicle navigation is implemented using a receding-horizon control (RHC), also known as model predictive control (MPC), [33, 34, 35, 36, 37]. A good overview of MPC is given in [38, 39]. Broadly, the idea is that the controller generates an optimal control input with respect to a user-defined cost function, over a finite time horizon T_{plan}. The input is implemented on the vehicle in open-loop fashion for a time interval $T_{\text{replan}} \leq T_{\text{plan}}$; the state of the vehicle is then measured and the process is repeated with initial state given by the new vehicle state. The MPC framework is a powerful tool for guidance of underwater vehicles because the difficulties associated with underwater localization (the lack of GPS signal under the water surface and the high energy cost of sonar-based localization methods) make closed-loop position-based feedback control impractical for long-duration missions. During extended field deployments, the vehicle typically uses dead-reckoning to estimate its position while underwater, and receives a position update during periodic surfacings, when GPS signal is available. It is therefore quite natural to use MPC control with T_{replan} given by the vehicle surfacing interval.

The receding-horizon control implementation for autonomous underwater vehicles may differ from the classical MPC approach described above. It is common, for example, to generate a reference trajectory at each planning step, rather than directly computing a control input. The control input is then generated using a simple on-board trajectory-following controller. Examples of controllers which utilize this version of receding-horizon control include the Glider Coordinated Control System (GCCS) [40, 41] and Sensorweb [6].

The generation of reference trajectories using modeled vehicle dynamics and forecast flow data obtained from predictive ocean models is a fairly well-studied problem in the field of underwater vehicle navigation. One approach is to use dynamic programming methods, as in [6], which allow one to find a globally optimal path. This approach may be quite slow and computationally intensive, however, and typically faster heuristic algorithms are used in application. Garau *et al* use an A* algorithm to generate min-time paths for AUVs in spatially varying, time-static flows [42, 11]. A Fast Marching (FM)-based algorithm for efficient path planning in a static flow field is described in [43]; this method can be generalized to strong [44] and time-varying flows [45]. Optimal path planning using beta-splines is demonstrated in [7, 46]. Path planning using genetic algorithms is described in [47, 48, 49], and case-based path planning is used in [50].

The above algorithms for generating reference trajectories assume that the flow field is deterministic and known exactly; deviations of the real vehicle trajectory from the generated reference are not considered, and no attempt is made to quantify the expected path-tracking performance of the vehicle under given flow conditions. Path-tracking performance may be maintained through periodic re-planning of the reference trajectory; at the same time, frequent replanning is undesirable for vehicles operating under the surface of the water, since it requires operation at the surface, where the vehicle is less capable of efficient maneuvering, and may be in danger of colliding with surface craft (especially when operating in areas near shipping lanes) [8, 10]. A prediction of the error between the real

vehicle position and the reference trajectory over time may be used to set the replanning interval to maintain appropriate path-following performance while minimizing the surfacing frequency.

There are several works in the existing literature which consider path-planning under uncertainty in the modeled vehicle motion. An analytic method for computing the mean and variance of the difference between the real and modeled position of an autonomous surface vehicle performing constant-speed maneuvers in a no-flow environment is developed in [51] and applied to path planning through an environment with obstacles in [52]. Another approach, based on use of an unscented Kalman filter, is used to estimate the variance of the error in predicted position of an autonomous underwater vehicle in [53]. These methods assume that the uncertainty in the vehicle motion can be modeled as an additive zero-mean Gaussian white noise in the system dynamics. A more general error model can be handled using particle methods. For example, [54, 55] use particle methods to estimate the position distribution of a vehicle with uncertain dynamics. However, particle-based methods tend to be computationally intensive, and give no insight into the structures in the flow field and error which contribute most significantly to growth of error in predicted vehicle position.

2.3 Autonomous Underwater Vehicles

This section provides a short introduction to autonomous underwater vehicles, with emphasis on underwater gliders. The use of these vehicles in oceanographic studies motivates the proposed research into predictability of Lagrangian paths of underwater vehicles.

In recent years, autonomous underwater vehicles (AUVs) have emerged as a highly versatile technology in the field of oceanographic research. They are flexible and compact sensor platforms with controlled vertical and horizontal velocity inputs, and can be roughly divided into two groups: actively-propelled craft; and gliders. Gliders are variable-buoyancy vehicles which convert vertical motion in the water column to horizontal movement. The two groups are not entirely disjoint; hybrid gliders which combine both active and passive

propulsion methods are being developed [56, 57, 58]. An overview of the development of unmanned underwater vehicles is given in [59].

Actively propelled AUV models include the Iver2, manufactured by OceanServer Technology; the Folaga, manufactured by Graal Tech; the Remus 100, manufactured by Hydroid; and various others. These are man-portable platforms designed for easy deployment and recovery. They are capable of deployments lasting for several hours at a time; maximum mission time range from approximately 6 to 24 hours. Typical horizontal speeds range from approximately 1 to 1.5 m/s [60], with maximum depth of 80-200 m. Larger active-propulsion autonomous vehicles such as ex. Autosub3, manufactured by the National Oceanography Centre, the Hugin 4500, manufactured by Konsberg Maritime, and Seahorse, manufactured by Penn State University's Applied Research Laboratory, are capable of deployments lasting 60-72 hours, with top speeds of 1.5-2 m/s and maximum dive depths of 1-4.5 km [60].

Buoyancy-driven underwater gliders, on the other hand, tend to have lower through-water velocities and longer mission endurance times as compared to actively-propelled vehicles. To dive, a glider displaces a flexible membrane, effectively sucking in a small amount of water. This causes it to become negatively buoyant and sink in the water column. The vertical motion is converted to horizontal glide using wings. At the bottom of the dive, the glider displaces the membrane in the opposite direction to achieve positive buoyancy; the resulting motion is a characteristic vertical zig-zag path. The three most commonly used commercial gliders are reviewed by Rudnick *et al* in [5]. These are the Spray, built at Scripps Inst. of Oceanography; the Slocum battery, manufactured by Webb Research Corp., and the Seaglider, built at U. of Washington. The Spray and Seaglider are deep-water survey vehicles, with max. dive depth of 1.5 and 1 km, and endurance of 330 and 200 days, respectively. The Slocum battery is designed for coastal surveying missions. The max. dive depth, depending on the model, is 200 or 1000 m, and endurance is 20 days (30 days for newer models) [5, 61]. A new deep-sea glider currently being developed by Webb

will use thermal differences to expand/contract its hull to adjust buoyancy; this model is expected to have a mission endurance time of 3-5 years.

Autonomous underwater vehicles are commonly used in environments that are not readily accessible by other survey methods (ex. under arctic ice, as described in [62, 63]), or for ocean monitoring missions that require mobility and long-duration deployments (see for example [5, 64, 8]), as cost of operating autonomous vehicles in the ocean is significantly lower than running ship-based missions [65]. AUVs may also be used to track moving or evolving ocean features, as in [66, 8, 9, 67]. Multiple AUVs may be deployed together for improved coverage of the survey area and improved data collection, as in [68, 69, 70, 64].

The vehicles described in this section motivate the proposed study of trajectory-following performance of autonomous agents under imperfectly modeled flow fields. As autonomous underwater vehicles become increasingly popular sensor platforms for oceanographic research, there is an increasing practical need to understand the theoretical performance limits of such vehicles in ocean environments that are not yet fully modeled or understood. In the proposed research, data from a field experiment off the coast of Long Bay, SC, involving two Slocum battery gliders, will be used to verify theoretical results.

CHAPTER 3

CONTROLLED LAGRANGIAN PARTICLE TRACKING

Controlled Lagrangian Particle Tracking is used to model the motions of vehicles (ie., controlled particles) with controlled velocity inputs in ocean flow fields. Let $\mathbf{x} \in \mathcal{D} \subset \mathbb{R}^2$ denote the horizontal position the vehicle. In general, the net velocity of the vehicle is a function of the vehicle position $\mathbf{x}$, the ambient mean water velocity $\mathbf{F}$, the small-scale turbulent flow component $v(t)$, and the control input u:

$$\frac{\mathrm{d}\mathbf{x}(t)}{\mathrm{d}t} = \mathbf{g}(\mathbf{x}(t), \mathbf{F}(\mathbf{x}, t), v(t), u(\mathbf{x}, \mathbf{F}, t)). \tag{1}$$

The functional form of $\mathbf{g}$ depends on the dynamics of the vehicle itself, the hydrodynamic coupling between vehicle and ambient flow, and on the ambient flow velocity. Errors can enter the model in a number of places, causing the modeled vehicle position to diverge from the true position observed in the field; we classify them broadly as errors in the modeled vehicle dynamics (including errors in the modeled coupling between ambient flow and vehicle motion) and errors in the modeled flow dynamics. In the case of slow-moving vehicles moving in complex flow environments with a reasonable model of the vehicle motion, the error in modeled position is dominated by the latter error source; that is, error in the modeled flow conditions. We therefore focus on this error source in our work throughout this dissertation.

3.1 Vehicle Motion Model

The random-flight model of [26, 27, 28, 31] is used to describe motions of material particles moving in the ocean. The ocean flow field is decomposed into two constituent components: a mean flow $\mathbf{F}_R$, and a stochastic eddy diffusion field v, which models small-scale flow fluctuations caused by physical eddies, as well as waves, wind-driven flows, and other turbulent flow components. It has been shown that this approach can be used effectively to model motions of passive drifter platforms in the ocean, provided that the parameters

describing the turbulent flow components are known or can be estimated [31, 71]. The random flight model is realized using the following Langevin "random flight" equation [31]:

$$\mathrm{d}\mathbf{x} = (\mathbf{F}_R(\mathbf{x}, t) + \nu(t) + \mathbf{v}(\mathbf{u}(\mathbf{x}, t)))\mathrm{d}t \tag{2a}$$

$$\mathrm{d}\nu = -A\nu(t)\mathrm{d}t + \Lambda \mathrm{d}\omega, \tag{2b}$$

where $\mathbf{F}_R(\mathbf{x}, t)$ is the underlying mean flow, ν is the eddy diffusion term, $\mathbf{v}$ is the through-water velocity of the vehicle, and $\mathbf{u}$ is the control input. The matrices A and $\Lambda \in \mathbb{R}^{2\times 2}$ are given by

$$A = \begin{bmatrix} \frac{1}{\tau} & \Omega \\ -\Omega & \frac{1}{\tau} \end{bmatrix} \qquad \Lambda = \begin{bmatrix} \sigma\sqrt{\frac{2}{\tau}} & 0 \\ 0 & \sigma\sqrt{\frac{2}{\tau}} \end{bmatrix}. \tag{3}$$

Here σ denotes the variance of the stochastic velocity fluctuations; τ represents Lagrangian correlation time and may be interpreted as a "forgetting time" parameter; and Ω is the spin parameter. The stochastic input ω represents zero-mean, Gaussian white noise. In the remainder of this dissertation, it is assumed that the values of τ and σ are known and that $\Omega = 0$. The vehicle can be controlled by adjusting its through-water speed $s(\mathbf{x}, t) \triangleq \| \mathbf{v} \|$ and heading $\phi(\mathbf{x}, t) \triangleq \angle \mathbf{v}$.

For autonomous underwater gliders, the throughwater speed of the vehicle is determined by the vertical speed of the vehicle and by its dive angle, and is approximately constant over all dives. We denote the resulting constant throughwater speed by s. In this case, vehicle position is given by

$$\mathrm{d}\mathbf{x} = (\mathbf{F}_R(\mathbf{x}, t) + \nu(t) + \mathbf{v}(\phi))\mathrm{d}t, \tag{4a}$$

$$\mathrm{d}\nu = -A\nu(t)\mathrm{d}t + \Lambda \mathrm{d}\omega, \tag{4b}$$

where $\| \mathbf{v} \| = s$ and $\phi(\mathbf{x}, t) = \mathbf{u}(\mathbf{x}, t)$ is the commanded vehicle heading.

Given a model forecast of the ocean flow field, it is possible to predict the vehicle position through numerical integration of the modeled vehicle dynamics (equations (2) or (4)),

with real flow replaced by the forecast values and $\nu(t) \equiv 0$. We now turn to examination of the error in the resulting predicted position of the vehicle.

3.2 Controlled Lagrangian Particle Tracking Error

Suppose that the modeled flow is available over a prediction time window $[t_0, t_1]$ (where it is possible that $t_1 \to \infty$). Let $\mathbf{z}(t)$, $t \in [t_0, t_1]$, denote the predicted vehicle position obtained from numerical integration of (2a) under a specified control law, with $\mathbf{F}_R(\mathbf{z}, t)$ replaced by the modeled value $\mathbf{F}_M(\mathbf{z}, t)$, and $\nu(t) \equiv 0$:

$$\frac{\mathrm{d}\mathbf{z}}{\mathrm{d}t} = \mathbf{F}_M(\mathbf{z}, t) + \mathbf{v}(\mathbf{u}(\mathbf{z}, t)). \tag{5}$$

The initial conditions at time t_0 are set so that $\mathbf{z}(t_0) = \mathbf{x}(t_0)$. The position prediction error $\mathbf{e}$ is defined as the offset between true and modeled vehicle position:

$$\mathbf{e}(t) \triangleq \mathbf{x}(t) - \mathbf{z}(t), \qquad \mathbf{e}(t_0) = [0,\ 0]^T,\ t \in [t_0, t_1]. \tag{6}$$

We refer to the magnitude of the position prediction error as the *controlled Lagrangian prediction error* (CLPE), denoted by $e(t)$:

$$e(t) \triangleq \| \mathbf{x}(t) - \mathbf{z}(t) \|, \tag{7}$$

where $\| \cdot \|$ represents the standard ℓ^2 norm on $\mathbb{R}^2$. The CLPE may be taken as a measure of performance of the model-based vehicle position prediction.

3.3 Position Prediction Error Dynamics

The time evolution of $\mathbf{e}$ is described by

$$\begin{aligned} \frac{\mathrm{d}\mathbf{e}}{\mathrm{d}t} &= \mathbf{F}_R(\mathbf{x}, t) + \nu(t) + \mathbf{v}(\mathbf{u}(\mathbf{x}, t)) - \mathbf{F}_M(\mathbf{z}, t) - \mathbf{v}(\mathbf{u}(\mathbf{z}, t)) \\ &= \mathbf{F}_M(\mathbf{x}, t) - \mathbf{F}_M(\mathbf{z}, t) + \mathbf{f}(\mathbf{x}, t) + \nu(t) + \mathbf{v}(\mathbf{u}(\mathbf{x}, t)) - \mathbf{v}(\mathbf{u}(\mathbf{z}, t)) \end{aligned} \tag{8}$$

where $\mathbf{f}(\zeta, t) \triangleq \mathbf{F}_R(\zeta, t) - \mathbf{F}_M(\zeta, t)$ is the error in modeled mean flow velocity at (ζ, t) and $\mathbf{e}(t_0) = 0$. Defining

$$\mathbf{V}(\zeta, t; \mathbf{u}) \triangleq \mathbf{F}_M(\zeta, t) + \mathbf{v}(\mathbf{u}(\zeta, t)) \tag{9}$$

to be the net vehicle velocity under the modeled flow, we can write the time evolution of the error in predicted vehicle velocity as

$$\frac{\mathrm{d}\mathbf{e}}{\mathrm{d}t} = \mathbf{V}(\mathbf{x}, t; \mathbf{u}) - \mathbf{V}(\mathbf{z}, t; \mathbf{u}) + \mathbf{f}(\mathbf{x}, t) + \nu(t), \qquad \mathbf{e}(t_0) = 0 \tag{10a}$$

$$\frac{\mathrm{d}\mathbf{z}}{\mathrm{d}t} = \mathbf{V}(\mathbf{z}, t; \mathbf{u}). \tag{10b}$$

For a given flow field and controller, $\mathbf{V}$ is a known function on $\mathcal{D} \times [t_0, t_1]$. The error in modeled flow velocity $\mathbf{f} : \mathcal{D} \times [t_0, t_1] \to \mathbb{R}^2$ may be treated as an unknown perturbation in the position prediction error dynamics, and $\nu : [t_0, t_1] \to \mathbb{R}^2$ as a noise input. Consider the unperturbed system with zero noise:

$$\frac{\mathrm{d}\mathbf{e}}{\mathrm{d}t} = \mathbf{V}(\mathbf{z} + \mathbf{e}, t; \mathbf{u}) - \mathbf{V}(\mathbf{z}, t; \mathbf{u}) \tag{11a}$$

$$\frac{\mathrm{d}\mathbf{z}}{\mathrm{d}t} = \mathbf{V}(\mathbf{z}, t; \mathbf{u}) \tag{11b}$$

In the unperturbed case, $\frac{\mathrm{d}\mathbf{e}}{\mathrm{d}t} = 0$ at $\mathbf{e} = 0$ for all $t \in [t_0, t_1]$. In general, however, (11a) is a complex nonlinear system with time-varying dynamics. The modeled ocean flow $\mathbf{F}_M$ component of net vehicle velocity $\mathbf{V}$ may include flow components that range in scale from thousands of kilometers (like the Gulf Stream) to small eddies or filaments with size on the order of the ocean model gridsize (the highest-resolution ocean models typically have a gridsize of $1.5 - 2$ km). The throughwater velocity of the vehicle depends on the control law used. We assume, here, that the mean ocean flow is slowly-varying in space compared with the size of the ocean model grid, and that the control is chosen in such a way that the net throughwater velocity of the vehicle varies slowly in space over scales comparable to ocean model gridsize. The dynamics of $\mathbf{e}$ about the point $\mathbf{e} = 0$ can be approximated using a first-order Taylor expansion of (11a), which gives the following time-varying system:

$$\frac{\mathrm{d}\mathbf{e}}{\mathrm{d}t} \approx D_{\mathbf{z}}\mathbf{V}(\mathbf{z}, t; \mathbf{u})\mathbf{e}. \qquad \frac{\mathrm{d}\mathbf{z}}{\mathrm{d}t} = \mathbf{V}(\mathbf{z}, t; \mathbf{u}) \tag{12a}$$

Adding in the perturbation $\mathbf{f}$ and driving noise ν, we have:

$$\frac{\mathrm{d}\mathbf{e}}{\mathrm{d}t} \approx D_{\mathbf{z}}\mathbf{V}(\mathbf{z}, t; \mathbf{u})\mathbf{e} + \mathbf{f}(\mathbf{z} + \mathbf{e}, t) + \nu(t) \qquad \frac{\mathrm{d}\mathbf{z}}{\mathrm{d}t} = \mathbf{V}(\mathbf{z}, t; \mathbf{u}). \tag{13a}$$

The form of $\mathbf{V}$ depends on the choice of controller used by the vehicle. Several possible control strategies are described in the following section.

3.4 Vehicle Controllers

In this section we describe three simple controllers for autonomous vehicles operating in ocean flow environments with flow forecasts from predictive ocean models. These controllers are chosen for their simplicity, as good starting-points for understanding the interaction between ambient flow and control effort in the growth of error in predicted vehicle position, as well as for their practical importance for field operations with autonomous vehicles. The first is the flow-canceling controller, which may be used to keep the vehicle stationary in the flow, assuming that the speed and heading can be controlled directly. This hovering behavior is used implicitly in many path-planning strategies for flow fields with strong spatio-temporal variations to "wait out" flows that are too strong for the vehicle to navigate directly. The second controller is the transect-following controller, which is used to stabilize the vehicle trajectory to a straight line. We assume that the heading of the vehicle may be controlled directly, but the speed is fixed (this is typical for slow-moving underwater vehicles like gliders, whose through-water speed determined by the dive angle, which is fixed before deployment in the field). In scientific applications, this controller may be used to collect data along a cross-section of the domain of interest. The last controller is the station-keeping controller, which may be used to drive the vehicle to a given position of interest. As in the transect-following controller, we assume that the vehicle travels with fixed through-water speed and that heading can be adjusted directly.

3.4.1 Flow-canceling controller

Consider a vehicle whose speed and heading can be controlled directly. Let $\mathbf{v}(u(\mathbf{x}, t)) = -\mathbf{F}_M(\mathbf{x}, t)$, where $\mathbf{F}_M(\mathbf{x}, t)$ is the modeled ocean flow at position $\mathbf{x}$ and time t. That is, the vehicle is able to perfectly cancel the modeled ambient flow velocity. The net vehicle

motion is then given by

$$\frac{\mathrm{d}\mathbf{x}(t)}{\mathrm{d}t} = \mathbf{F}_R(\mathbf{x}, t) - \mathbf{F}_M(\mathbf{x}, t) + \nu(t) = \mathbf{f}(\mathbf{x}, t) + \nu(t). \tag{14}$$

The net motion of the vehicle depends only on the structure of the error in the modeled ocean flow.

3.4.2 Transect-following controller

The transect-following controller is used to track a straight-line trajectory (transect) ℓ in the ocean flow field. We assume that the vehicle travels with constant through-water speed $\|\,\mathbf{v}\,\| = s(\mathbf{x}, t) = s$. Let $\mathbf{T}$ be a unit vector along the transect, pointing in the direction of travel, and let $\mathbf{N}$ be normal to $\mathbf{T}$. Let $\mathbf{p} \in \ell$ be an arbitrary point on the transect. The heading u is chosen to cancel modeled flow velocity normal to the transect direction, and an additional proportional controller is used to maintain the vehicle on the transect line (as far as is possible given fixed through-water speed of the vehicle). Let $\mathrm{sat}_c(\cdot)$ denote the saturation function, $\mathrm{sat}_c : \mathbb{R} \to [-c, c]$, where

$$\mathrm{sat}_c(y) = \begin{cases} -c & \text{if } y < -c \\ y & \text{if } -c \le y \le c \\ c & \text{if } y > c. \end{cases} \tag{15}$$

Then for $(\zeta, t) \in \mathcal{D} \times \mathbb{R}$,

$$\mathbf{v}(\zeta, t)^T\mathbf{N} = -\mathrm{sat}_s(\mathbf{F}_M(\zeta, t)^T\mathbf{N} + K(\zeta - \mathbf{p})^T\mathbf{N}), \tag{16}$$

where K is a constant gain. Since the net through-water speed s of the vehicle is constant, its through-water velocity along $\mathbf{T}$ is given by

$$\mathbf{v}(\zeta, t)^T\mathbf{T} = \sqrt{s^2 - \mathrm{sat}_s^2(\mathbf{F}_M(\zeta, t)^T\mathbf{N} + K(\zeta - \mathbf{p})^T\mathbf{N})}. \tag{17}$$

The heading angle which satisfies (16)-(17) is:

$$u(\zeta, t) = \tan^{-1}\frac{T_2}{T_1} - \sin^{-1}\frac{\mathrm{sat}_s(\mathbf{F}_M(\zeta, t)^T\mathbf{N} + K(\zeta - \mathbf{p})^T\mathbf{N})}{s}. \tag{18}$$

(See Fig. 2). Let

$$\gamma(\zeta) \triangleq s^2 - (\mathbf{F}_M^T\mathbf{N} + K(\zeta - \mathbf{p})^T\mathbf{N})^2. \tag{19}$$

Using the notation defined in (9), we have:

$$\mathbf{V}(\zeta, t) = \begin{cases} \left(\mathbf{F}_M^T\mathbf{T} + \sqrt{s^2 - (\mathbf{F}_M^T\mathbf{N} + K(\zeta - \mathbf{p})^T\mathbf{N})^2}\right)\mathbf{T} - K(\zeta - \mathbf{p})^T\mathbf{N} & \text{if } \gamma \geq 0 \\ \left(\mathbf{F}_M^T\mathbf{T}\right)\mathbf{T} + \left(\mathbf{F}_M^T\mathbf{N} - \text{sign}\left(\mathbf{F}_M^T\mathbf{N} + K(\zeta - \mathbf{p})^T\mathbf{N}\right)s\right)\mathbf{N} & \text{otherwise.} \end{cases} \tag{20}$$

The vehicle must be able to cancel cross-track flow to apply the proportional-gain controller without exceeding its the total available speed.

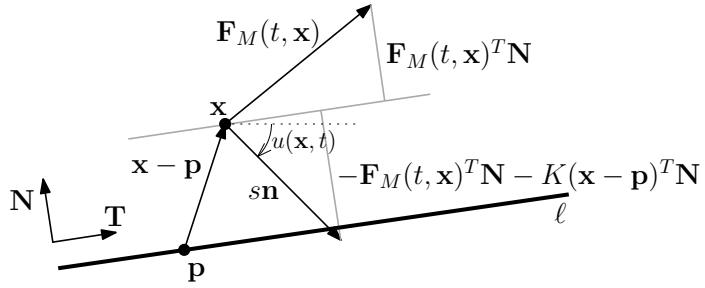

Figure 2: Schematic of the transect-following controller.

3.4.3 Station-keeping controller

The third controller we describe is the station-keeping controller. Like the transect-following controller, this controller is defined for the constant-speed vehicle model with heading control. The vehicle should always move toward a fixed goal position $\mathbf{g}$. Thus, the heading u is chosen to cancel the modeled flow velocity in the direction normal to the desired motion. The through-water speed of the vehicle s is assumed to be constant. Let $\mathbf{T}$ be the unit vector from the vehicle position to the goal $\mathbf{g}$, and let $\mathbf{N}$ be normal to $\mathbf{T}$. Without loss of generality, we choose the coordinate system so that $\mathbf{g} = 0$. Then $\mathbf{T}(\mathbf{x}) = -\frac{\mathbf{x}}{\|\mathbf{x}\|}$ and $\mathbf{N} = -\frac{J\mathbf{x}}{\|\mathbf{x}\|}$, where J is the 90° rotation matrix. Under the flow-canceling controller, u is chosen so that net motion is along $\mathbf{T}$. Assuming $\|\mathbf{F}_M\| < s$ everywhere, so that flow cancellation is always possible, this means that:

$$\mathbf{v}(\mathbf{u}(\mathbf{x}, t))^T\mathbf{N} = -\mathbf{F}_M(\mathbf{x}, t)^T\mathbf{N}. \tag{21}$$

To satisfy (21), we must have $u(\mathbf{x}, t) = \tan^{-1}\frac{\mathbf{x}_2}{\mathbf{x}_1} + \pi - \sin^{-1}\frac{\mathbf{F}_M(\mathbf{x},t)^T\mathbf{N}}{s}$ (see Fig. 3). The resulting through-water velocity component along $\mathbf{T}$ is given by

$$\mathbf{v}(\mathbf{u}(\mathbf{x}, t))^T\mathbf{T} = \sqrt{s^2 - (\mathbf{F}_M(\mathbf{x}, t)^T\mathbf{N})^2}. \tag{22}$$

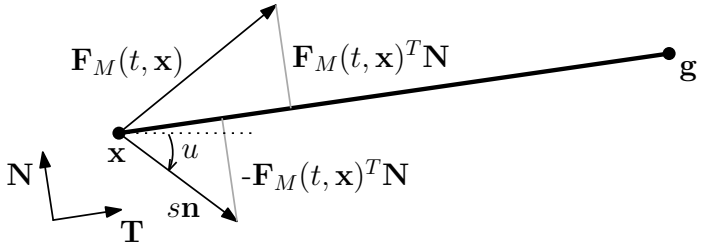

Figure 3: Schematic of the station-keeping controller.

The control input is well-defined everywhere except at the goal position $\mathbf{g} = 0$, where $T = -\frac{\mathbf{x}}{\|\mathbf{x}\|}$ and $\mathbf{N} = J\mathbf{T}$ are undefined. To avoid this singularity in our analysis, we switch to a simple flow-canceling control in an area around the goal; that is, for $\|\mathbf{x}\| \leq R$, where $R \in \mathbb{R}_+$ is a fixed threshold value, we allow for adjustments in the vehicle speed, and set $\mathbf{v}(u(\mathbf{x}, t)) = -\mathbf{F}_M(\mathbf{x}, t)$.

Summarizing the above results, we have that under station-keeping control:

$$u(\mathbf{x}, t) = \begin{cases} \tan^{-1}\frac{\mathbf{x}_2}{\mathbf{x}_1} + \pi - \sin^{-1}\frac{\mathbf{F}_M(\mathbf{x},t)^T\mathbf{N}}{s}, & \|\mathbf{x}\| \geq R \\ \tan^{-1}\frac{\mathbf{x}_2}{\mathbf{x}_1} + \tan^{-1}\frac{\mathbf{F}_M(\mathbf{x},t)^T\mathbf{N}}{\mathbf{F}_M(\mathbf{x},t)^T\mathbf{T}}, & \|\mathbf{x}\| < R \end{cases} \tag{23}$$

$$\mathbf{v}(\mathbf{u}(\mathbf{x}, t)) = \begin{cases} \sqrt{s^2 - (\mathbf{F}_M(\mathbf{x}, t)^T\mathbf{N})^2}\mathbf{T} - (\mathbf{F}_M(\mathbf{x}, t)^T\mathbf{N})\mathbf{N}, & \|\mathbf{x}\| \geq R \\ -\mathbf{F}_M(\mathbf{x}, t) & \|\mathbf{x}\| < R. \end{cases} \tag{24}$$

Using the notation defined in (9), we have:

$$\mathbf{V}(\mathbf{x}, t) = \begin{cases} \left(\mathbf{F}_M^T\mathbf{T} + \sqrt{s^2 - (\mathbf{F}_M^T\mathbf{N})^2}\right)\mathbf{T}, & \|\mathbf{x}\| \geq R \\ 0 & \|\mathbf{x}\| < R. \end{cases} \tag{25}$$

Given control input, the motion of the vehicle is fully specified. The position of the vehicle can be predicted using numerical integration of (2a) (or, for a constant-speed vehicle, of (4a)), with $\mathbf{F}_R$, the real flow velocity, replaced by its modeled value, $\mathbf{F}_M$, and $\nu(t) \equiv 0$.

We examine the accuracy of predicted vehicle positions for different controllers described here, under different flow conditions, in the following chapters.

CHAPTER 4

ERROR GROWTH UNDER THE FLOW-CANCELING CONTROLLER

The flow-canceling controller described in Section 3.4.1 is the simplest controller based on predictive ocean model data; it simply cancels the predicted ocean flow at the current position of the vehicle. We derive the expected upper threshold for exponential growth of CLPT error for one and two-dimensional flow fields. The expected thresholds are functions of the gridsize in the ocean model used to estimate the flow.

In Sections 4.1 and 4.2, we consider the error growth caused by error in predicted flow $\mathbf{f}$ alone; in those sections we therefore make the following assumption:

(A2) The small-scale eddy diffusivity is negligible, so that $\nu(t) \equiv 0$.

Under Assumption (A2), the position estimation error evolves in times as

$$\frac{\mathrm{d}\mathbf{e}}{\mathrm{d}t} = \frac{\mathrm{d}\mathbf{x}}{\mathrm{d}t} - \frac{\mathrm{d}\mathbf{z}}{\mathrm{d}t} = \mathbf{F}_R(\mathbf{x}, t) - \mathbf{F}_M(\mathbf{x}, t) + (\mathbf{F}_R(\mathbf{z}, t) - \mathbf{F}_M(\mathbf{z}, t)) = \mathbf{f}(\mathbf{x}, t) \tag{26}$$

with $\mathbf{e}(t_0) = [0,\ 0]^{\mathrm{T}}$. In general $\mathbf{f}$ is an unknown function of position and time, whose values depend on the particular realization of the ocean flow and on the model used. Under the perfect flow canceling controller, the position of the simulated vehicle remains $\mathbf{z}(t) = \mathbf{z}(t_0)$. Therefore, $\mathbf{e}(t) = \mathbf{x}(t) - \mathbf{z}(t_0)$. It can be assumed, without loss of generality, that the vehicle starts at the origin, $\mathbf{x}(t_0) = \mathbf{z}(t_0) = [0,\ 0]^{\mathrm{T}}$. Then, $\mathbf{e}(t)$ given by (26) will be equal to $\mathbf{x}(t)$ in the following system:

$$\frac{\mathrm{d}\mathbf{x}}{\mathrm{d}t} = \mathbf{f}(\mathbf{x}, t)\mathrm{d}t, \qquad \mathbf{x}(t_0) = 0. \tag{27}$$

For simplicity, suppose that $\mathbf{f}$ is a function of $\mathbf{x}$ only. We also assume that $\mathbf{f}$ has equilibria; that is, there exits a non-empty set $\mathbf{X}$ s.t. $\mathbf{f}(\mathbf{x}, t) = 0\ \forall \mathbf{x} \in \mathbf{X}$.

4.1 The One-Dimensional Case

First consider the case when flow is one-dimensional. We make the following assumptions:

(B1) The vehicle is confined to move on a line, so the domain of $\mathbf{f}$ is $\mathbb{R}$. Since $\mathbf{f}$ is now a scalar function, it is denoted by f; similarly, the real vehicle position $\mathbf{x}$ is denoted by x; similarly the position of the simulated vehicle is denoted z.

(B2) A uniform grid of gridsize h is defined over $\mathbb{R}$. The ocean model outputs an estimate F_M of the real flow F_R at each gridpoint $x_k = kh$, $k \in \mathbb{Z}$. We model the values of $f(x) = F_M(x) - F_R(x)$ at the grid points are independent identically distributed random variables[1], denoted by ξ_k ($\xi_k = f(x_k) = f(kh)$). These ξ_k are assumed to be symmetrically distributed around 0, with probability density function ρ_ξ.

(B3) The initial conditions are given by $x(t_0) = z(t_0) = 0$.

The values of f are not known everywhere in $\mathbb{R}$, since they depend on the structure of the unknown flow F_R, as well as on the method used to interpolate F_M between gridpoints. However, f can be approximated at any point by taking the linear interpolation of its values at the gridpoints. For $x \in (x_k, x_{k+1})$, say that

$$f(x) = \frac{(x_{k+1} - x)\,\xi_k + (x - x_k)\,\xi_{k+1}}{h}. \tag{28}$$

Under Assumptions (B1)-(B3), $f(x)$ has equilibria given by

$$x_{eq} = (\xi_{k+1}x_k - \xi_k x_{k+1})/(\xi_{k+1} - \xi_k), \tag{29}$$

if $x_{eq} \in [x_k,\ x_{k+1}]$. Since f is time-invariant, x in (27) converges to a stable equilibrium x_{eq} of f. Thus, x_{eq} marks an upper threshold on growth of the CLPT error caused by f; the threshold is given by $E(|x_{eq} - z(t_0)|)$. The expected threshold will be found, with expectation taken over all realizations of the model flow f. The following lemmas are needed for this:

Lemma 4.1.1 *The position x_{eq} in (29) is a stable equilibrium of (27) under Assumptions (B1)-(B3) if and only if $\xi_k > 0$ and $\xi_{k+1} < 0$.*

[1]Note that, for any given realization of the ocean model and true ocean flow fields, the flow error f is a fixed, unknown function. Expectations involving f are taken over the set of all possible realizations of the ocean model.

Proof: A sufficient and necessary condition for x_{eq} to be a stable equilibrium is that it satisfies $f(x_{eq}) = 0$ and $\partial f/\partial x(x_{eq}) = (\xi_{k+1} - \xi_k)/h < 0$.

Suppose that $\xi_k > 0$ and $\xi_{k+1} < 0$. Clearly, there exists a point $x_{eq} \in [hk, h(k+1)]$, given by (29), which is an equilibrium of f. Since $(\xi_{k+1} - \xi_k)/h < 0$, x_{eq} must be a stable equilibrium.

Conversely, suppose that $x_k < x_{eq} < x_{k+1}$ is a stable equilibrium. Using the equation for x_{eq}, and the fact that $(\xi_{k+1} - \xi_k)/h < 0$, one gets:

$$x_k < \quad \frac{\xi_{k+1}x_k - \xi_k x_{k+1}}{\xi_{k+1} - \xi_k} \quad < x_{k+1} \tag{30}$$

$$x_k(\xi_{k+1} - \xi_k) > \quad \xi_{k+1}x_k - \xi_k x_{k+1} \quad > x_{k+1}(\xi_{k+1} - \xi_k). \tag{31}$$

Subtracting the middle term from both sides of (31), gives:

$$\xi_k(x_{k+1} - x_k) > 0 > \xi_{k+1}(x_{k+1} - x_k), \tag{32}$$

which directly gives $\xi_k > 0$, $\xi_{k+1} < 0$, since $x_{k+1} - x_k = h > 0$. This proves the Lemma.

Lemma 4.1.2 *The probability that $x_{eq} \in (x_k, x_{k+1})$ given $\xi_0 > 0$ is:*

$$\mathbf{Pr}(x_{eq} \in (x_k, x_{k+1}) | \xi_0 > 0) = \left(\frac{1}{2}\right)^{k+1}.$$

Proof: By Lemma 4.1.3, $\mathbf{Pr}(x_{eq} \in (x_k, x_{k+1}) | \xi_0 > 0)$ is simply the probability that $\xi_1, ..., \xi_k > 0$ and $\xi_{k+1} < 0$. Because the values of ξ are independent,

$$\mathbf{Pr}(\xi_1, ..., \xi_k > 0, \xi_{k+1} < 0) = \left(\prod_i^k \mathbf{Pr}(\xi_i > 0)\right)\mathbf{Pr}(\xi_{k+1} < 0).$$

The ξ_i are iid symmetrically-distributed variables, thus $\mathbf{Pr}(\xi_i > 0) = 1/2$ for all i. Similarly, $\mathbf{Pr}(\xi_{k+1} < 0) = 1/2$. Thus $\mathbf{Pr}(x_{eq} \in (x_k, x_{k+1}) | \xi_0 > 0) = (1/2)^{k+1}$.

With the above Lemmas, it is possible to calculate $E(|x_{eq}|)$, where x_{eq} is a stable equilibrium of (28) such that $x \to x_{eq}$ as $t \to \infty$. By definition,

$$E(|x_{eq}|) = \int_0^\infty |x| \rho_{|x_{eq}|}(x) \mathrm{d}x \tag{33}$$

where $\rho_{|x_{eq}|}(x)$ is the probability density function of $|x_{eq}|$. The variable ξ_0 can be introduced as a conditioning variable in (33); then, using the fact that ξ_k are symmetrically-distributed, zero-mean random variables, so that

$$\mathbf{Pr}(\xi_k > 0) = \mathbf{Pr}(\xi_k < 0) = \int_0^\infty \rho_\xi(x)\mathrm{d}x = 1/2, \tag{34}$$

one has:

$$E(|x_{eq}|) = \frac{1}{2}\int_0^\infty |x|\rho_{|x_{eq}|}(x|\xi_0 > 0)\mathrm{d}x + \frac{1}{2}\int_0^\infty |x|\rho_{|x_{eq}|}(x|\xi_0 < 0)\mathrm{d}x. \tag{35}$$

The following variables are defined for convenience:

$$x_+ = \mathrm{argmin}_{x>0}\{|x| : f(x) = 0, \partial f/\partial x < 0\} \tag{36}$$

$$x_- = \mathrm{argmin}_{x<0}\{|x| : f(x) = 0, \partial f/\partial x < 0\}. \tag{37}$$

The following two lemmas are needed for the calculation of $E(|x_{eq}|)$:

Lemma 4.1.3 *If $\xi_0 > 0$, then $x_{eq} = x_+$, and moreover, $x_{eq} \in (x_k, x_{k+1})$ where x_{k+1} is the position corresponding to the first negative value of ξ; that is, $\xi_j > 0$ for all $j \in \{1, 2, ..., k\}$, and $\xi_{k+1} < 0$.*

Proof: By the definition in (28), f is a continuous, piecewise affine function.

By continuity, $f(t_0) = \xi_0 > 0$ implies that $f > 0$ in some sufficiently small neighborhood ϵ of 0. Thus x cannot become negative, since $dx/dt = f(x) > 0$ for all $x \in \epsilon$; so $\lim_{t\to\infty} x(t) = x_{eq} > 0$.

Since f is piecewise affine, $f > 0$ on any interval $[x_k, x_{k+1}]$ with ξ_k, $\xi_{k+1} > 0$, and f must have a zero-crossing x_{eq} on any interval (x_k, x_{k+1}) with $\xi_k > 0$ and $\xi_{k+1} < 0$. By Lemma 4.1.1, this crossing is a stable equilibrium of (27). The smallest such crossing is x_+. Since $x = 0$ is in the region of attraction, $x \to x_{eq}$ as $t \to \infty$, and so $x_{eq} = x_+$.

Lemma 4.1.4 *If $\xi_0 < 0$, then $x_{eq} = x_-$, and moreover, $x_{eq} \in (x_{-k}, x_{-k+1})$ where x_{-k} is the point corresponding to the first positive value of ξ, that is, $\xi_j < 0$ for all $j \in \{-1, -2, ..., -k+1\}$, and $\xi_{-k} > 0$.*

The proof exactly parallels the proof of Lemma 4.1.3.

Theorem 4.1.5 *Under Assumptions (B1)-(B3) of the one-dimensional problem,*

$$\int_0^\infty |x|\rho_{|x_{eq}|}(x|\xi_0 > 0)\mathrm{d}x = \int_{-\infty}^0 |x|\rho_{|x_{eq}|}(x|\xi_0 < 0)\mathrm{d}x = \frac{3}{2}h.$$

Therefore, $E(|x_{eq}|) = \frac{3}{2}h$.

Proof: The statement $\int_0^\infty |x|\rho_{|x_{eq}|}(x|\xi_0 > 0)\mathrm{d}x = \int_{-\infty}^0 |x|\rho_{|x_{eq}|}(x|\xi_0 < 0)\mathrm{d}x$ follows from the symmetry of ρ_ξ. It remains to show that $E(|x_{eq}|) = 3h/2$.

Equation (35) for the expected value of $|x_{eq}|$ may be written as

$$E(|x_{eq}|) = \int_0^\infty |x|\rho_{|x_{eq}|}(x|\xi_0 > 0)\mathrm{d}x,$$

which can be decomposed as

$$E(|x_{eq}|) = \sum_{k=0}^{\infty} \int_{x_k}^{x_{k+1}} x\rho_{|x_{eq}|}(x|\xi_0 > 0, x_{eq} \in (x_k, x_{k+1}))\mathrm{d}x\mathbf{Pr}(x_{eq} \in (x_k, x_{k+1})|\xi_0 > 0). \quad (38)$$

Using Lemma 4.1.2, and applying a change of variables $u = x - x_k$, (38) can be written as

$$E(|x_{eq}|) = \sum_{k=0}^{\infty} \left[\frac{1}{2}\right]^{k+1} \int_0^h (u + x_k)\rho_{|x_{eq}-x_k|}(u|\xi_0 > 0, (x_{eq} - x_k) \in (0, h))\mathrm{d}u. \quad (39)$$

To evaluate this expression, one must compute $\rho_{|x_{eq}-x_k|}(u|\xi_0 > 0, (x_{eq} - x_k) \in (0, h))$. Given that $x_{eq} \in (x_k, x_{k+1})$, let $u_* \triangleq x_{eq} - x_k$ in this interval. To find $\rho_{u_*}(u|u_* \in (0, h))$, the probability density of u_* in terms of u, we consider the mapping $\phi : \mathbb{R}^2 \to \mathbb{R}^2 : (\xi_k, \xi_{k+1}) \mapsto (u_*, v)$, where

$$u_* = \frac{h\xi_k}{\xi_k - \xi_{k+1}} \quad (40)$$

$$v = \xi_k. \quad (41)$$

Let $\vec{\xi}$ denote the doublet (ξ_k, ξ_{k+1}), and $\vec{w}$ denote (u_*, v). The distribution of $\vec{w}$ is given by

$$\tilde{\rho}(\vec{w}) = \left|\det \frac{\partial\phi}{\partial\vec{\xi}}\right|^{-1} \rho(\phi^{-1}(\vec{w})). \quad (42)$$

The inverse map is well-defined and is given by

$$\phi^{-1}(\vec{w}) = (\xi_k, \xi_{k+1}) = (v, v(1 - h/u_*)), \tag{43}$$

while

$$\left|\det \frac{\partial \phi}{\partial \vec{\xi}}\right|^{-1} = \left|\det \begin{pmatrix} -\frac{h\xi_{k+1}}{(\xi_k - \xi_{k+1})^2} & \frac{h\xi_k}{(\xi_k - \xi_{k+1})^2} \\ 1 & 0 \end{pmatrix}\right|^{-1} = \frac{(\xi_k - \xi_{k+1})^2}{h\xi_k} = \frac{hv}{u_*^2}. \tag{44}$$

Substituting (44) and (43) into (42) gives:

$$\tilde{\rho}(\vec{w}) = \frac{hv}{u_*^2}\rho(v, v(1 - h/u_*)). \tag{45}$$

Since ξ_k and ξ_{k+1} are independent, symmetrically distributed random variables and $\xi_k > 0$ and $\xi_{k+1} < 0$ are given,

$$\rho(\xi_k) = 2\rho_\xi(\xi_k)H(\xi_k) \tag{46}$$

$$\rho(\xi_{k+1}) = 2\rho_\xi(\xi_{k+1})H(-\xi_{k+1}), \tag{47}$$

where $H(\cdot)$ denotes the unit step function.

Because the values of ξ are iid, the joint probability distribution is

$$\rho(\phi^{-1}(\vec{\omega})) = \rho(\vec{\xi}) = \rho(\xi_k)\rho(\xi_{k+1}) = \rho(v)\rho(v(1 - h/u_*)). \tag{48}$$

Thus, using (46)-(47), (45) may be written as

$$\tilde{\rho}(\vec{w}) = \frac{4hv}{u_*^2}\rho_\xi(v)\rho_\xi(v(1 - h/u_*))H(v)H(v(h/u_* - 1)). \tag{49}$$

Taking the marginal distribution over v gives:

$$\int_{-\infty}^{\infty} \tilde{\rho}(\vec{w})\mathrm{d}v = \frac{4h}{u_*^2}\int_0^\infty v\rho_\xi(v)\rho_\xi(v(1 - h/u_*))\mathrm{d}vH(h/u_* - 1). \tag{50}$$

Equation (50) is the distribution function in (39). Plugging in the above result for $\rho_{|x_{eq}-x_k|}(u|(x_{eq} - x_k) \in (0, h))$ in (39),

$$\begin{aligned} E(|x_{eq}|) &= \sum_{k=0}^{\infty}\left[\frac{1}{2}\right]^{k+1}\int_0^h \frac{4h(u + x_k)}{u^2}\left(\int_0^\infty v\rho_\xi(v)\rho_\xi(v(1 - h/u))\mathrm{d}v\right)\mathrm{d}u \\ &= \sum_{k=0}^{\infty}\left[\frac{1}{2}\right]^{k+1}\Bigg(\int_0^h \frac{4hu}{u^2}\left(\int_0^\infty v\rho_\xi(v)\rho_\xi(v(1 - h/u))\mathrm{d}v\right)\mathrm{d}u \\ &\qquad + \int_0^h \frac{4hx_k}{u^2}\left(\int_0^\infty v\rho_\xi(v)\rho_\xi(v(1 - h/u))\mathrm{d}v\right)\mathrm{d}u\Bigg). \end{aligned} \tag{51}$$

This expression contains two integrals which will be handled in turn. Consider first the integral

$$\int_0^h \frac{4hx_k}{u^2}\left(\int_0^\infty v\rho_\xi(v)\rho_\xi(v(1-h/u))\mathrm{d}v\right)\mathrm{d}u. \tag{52}$$

After pulling out constants and reversing the order of integration, this becomes:

$$4x_k\int_0^\infty v\left(\int_0^h \frac{h}{u^2}\rho_\xi(v(1-h/u))\mathrm{d}u\right)\rho_\xi(v)\mathrm{d}v \tag{53}$$

Using change of variables $s = v(1-h/u)$, the above expression may be written as

$$4x_k\int_0^\infty v\left(\int_{-\infty}^0 \frac{(v-s)^2}{hv^2}\rho_\xi(s)\frac{hv}{(v-s)^2}\mathrm{d}s\right)\rho_\xi(v)\mathrm{d}v = 4x_k\int_0^\infty\left(\int_{-\infty}^0\rho_\xi(s)\mathrm{d}s\right)\rho_\xi(v)\mathrm{d}v. \tag{54}$$

Because ρ_ξ is symmetric, $\int_{-\infty}^0\rho_\xi(s)\mathrm{d}s = 1/2$, the above integral is equal to $2x_k\int_0^\infty\rho_\xi(v)\mathrm{d}v$. Again, it follows from symmetry of ρ_ξ that $\int_0^\infty\rho_\xi(v)\mathrm{d}v = 1/2$, and this expression evaluates to $2x_k(1/2) = x_k$.

Similarly, one can evaluate the integral

$$\int_0^h \frac{4hu}{u^2}\left(\int_0^\infty v\rho_\xi(v)\rho_\xi(v(1-h/u))\mathrm{d}v\right)\mathrm{d}u = 4\int_0^\infty\left(\int_0^h\frac{hv}{u}\rho_\xi(v(1-h/u))\mathrm{d}u\right)\rho_\xi(v)\mathrm{d}v. \tag{55}$$

Once again letting $s = v(1-h/u)$ gives:

$$4\int_0^\infty\left(\int_{-\infty}^0(v-s)\rho_\xi(s)\frac{hv}{(v-s)^2}\mathrm{d}s\right)\rho_\xi(v)\mathrm{d}v = 4\int_0^\infty\int_{-\infty}^0\frac{hv}{v-s}\rho_\xi(s)\rho_\xi(v)\mathrm{d}s\mathrm{d}v. \tag{56}$$

It can be shown, using the symmetry of ρ_ξ, that:

$$4\int_0^\infty\int_{-\infty}^0\frac{hv}{v-s}\rho_\xi(s)\rho_\xi(v)\mathrm{d}s\mathrm{d}v = \frac{h}{2}. \tag{57}$$

Therefore,

$$\begin{aligned}
E(|x_{eq}|) &= \sum_{k=0}^\infty\left[\frac{1}{2}\right]^{k+1}\int_0^h\frac{4h(u+x_k)}{u^2}\left(\int_0^\infty v\rho_\xi(v)\rho_\xi(v(1-h/u_*))\mathrm{d}v\right)\mathrm{d}u \\
&= \sum_{k=0}^\infty\left(\frac{1}{2}\right)^{k+1}\frac{h}{2} + \sum_{k=0}^\infty\left(\frac{1}{2}\right)^{k+1}x_k \\
&= \frac{h}{4}\sum_{k=0}^\infty\left(\frac{1}{2}\right)^k + \frac{h}{2}\sum_{k=0}^\infty\left(\frac{1}{2}\right)^k k \\
&= \frac{h}{2} + h = \frac{3}{2}h,
\end{aligned} \tag{58}$$

where $x_k = kh$. This proves Theorem 4.1.5.

Theorem 4.1.6 *Suppose that $x(t_0) = 0$. The variance of $|x_{eq}|$ is given by*

$$\mathrm{Var}(|x_{eq} - x(t_0)|) = \iint_0^\infty \frac{4h^2v^2}{(v+s)^2}\rho_\xi(s)\rho_\xi(v)\mathrm{d}s\mathrm{d}v + \frac{7}{4}h^2. \tag{59}$$

Proof: Given $x(t_0) = 0$, $\mathrm{Var}(x_{eq}) = E|x_{eq}|^2 - (E|x_{eq}|)^2$. Then

$$\begin{aligned} E|x_{eq}|^2 &= \int_{-\infty}^{\infty} |x|^2\rho_{eq}(x)\mathrm{d}x \\ &= \int_{-\infty}^{0} |x|^2\rho_{eq}(x|\xi_0 < 0)\mathbf{Pr}(\xi_0 < 0)\mathrm{d}x + \int_0^\infty |x|^2\rho_{eq}(x|\xi_0 > 0)\mathbf{Pr}(\xi_0 > 0)\mathrm{d}x. \end{aligned} \tag{60}$$

By symmetry of the distribution of ξ_0, $\mathbf{Pr}(\xi_0 > 0) = \mathbf{Pr}(\xi_0 < 0) = \frac{1}{2}$, and

$$\int_{-\infty}^{0} |x|^2\rho_{eq}(x|\xi_0 < 0)\mathbf{Pr}(\xi_0 < 0)\mathrm{d}x = \int_0^\infty |x|^2\rho_{eq}(x|\xi_0 > 0)\mathbf{Pr}(\xi_0 > 0)\mathrm{d}x.$$

Thus, (60) can be written as

$$E|x_{eq}|^2 = \int_0^\infty |x|^2\rho_{eq}(x|\xi_0 > 0)\mathrm{d}x. \tag{61}$$

Splitting this integral over the intervals $[x_k, x_{k+1})$ gives

$$\begin{aligned} E|x_{eq}|^2 &= \sum_{k=0}^{\infty} \int_{x_k}^{x_{k+1}} |x|^2\rho_{eq}(x|\xi_0 > 0, x_{eq} \in (x_k, x_{k+1}))\mathbf{Pr}(x_{eq} \in (x_k, x_{k+1}))\mathrm{d}x \\ &= \sum_{k=0}^{\infty} \frac{1}{2^{k+1}} \int_{x_k}^{x_{k+1}} |x|^2\rho_{eq}(x|\xi_0 > 0, x_{eq} \in (x_k, x_{k+1}))\mathrm{d}x. \end{aligned} \tag{62}$$

Using change of variables $u = x - x_k$, (62) can be written as

$$E|x_{eq}|^2 = \sum_{k=0}^{\infty} \frac{1}{2^{k+1}} \int_0^h (u^2 + 2x_k u + x_k^2)\rho_u(u|\xi_0 > 0, x_{eq} \in (x_k, x_{k+1}))\mathrm{d}u. \tag{63}$$

Plugging in the distribution from (50) gives

$$E|x_{eq}|^2 = \sum_{k=0}^{\infty} \frac{1}{2^{k+1}} \int_0^h 4h\left(1 + \frac{2x_k}{u} + \frac{x_k^2}{u^2}\right)\left[\int_0^\infty v\rho_\xi(v)\rho_\xi\left(v\left(1 - \frac{h}{u}\right)\right)\mathrm{d}v\right]\mathrm{d}u, \tag{64}$$

where

$$\int_0^h 4h\left(1 + \frac{2x_k}{u} + \frac{x_k^2}{u^2}\right)\left[\int_0^\infty v\rho_\xi(v)\rho_\xi\left(v\left(1 - \frac{h}{u}\right)\right)\mathrm{d}v\right]\mathrm{d}u \tag{65}$$

can be split up into the three integrals

$$\int_0^h 4h\left[\int_0^\infty v\rho_\xi(v)\rho_\xi\left(v\left(1-\frac{h}{u}\right)\right)\mathrm{d}v\right]\mathrm{d}u \tag{66}$$

$$2x_k\int_0^h \frac{4h}{u}\left[\int_0^\infty v\rho_\xi(v)\rho_\xi\left(v\left(1-\frac{h}{u}\right)\right)\mathrm{d}v\right]\mathrm{d}u = 2x_k\left(\frac{h}{2}\right) = kh^2 \tag{67}$$

$$x_k\int_0^h \frac{4hx_k}{u^2}\left[\int_0^\infty v\rho_\xi(v)\rho_\xi\left(v\left(1-\frac{h}{u}\right)\right)\right]\mathrm{d}v = x_k^2 = k^2h^2, \tag{68}$$

where the last two integrals (67) and (68) are evaluated as in (55)-(57) and (52)-(54), respectively. Using change of variables $s = -v(1-h/u)$ in (66), we get:

$$\int_0^h 4h\left[\int_0^\infty v\rho_\xi(v)\rho_\xi\left(v\left(1-\frac{h}{u}\right)\right)\mathrm{d}v\right]\mathrm{d}u = 4h^2\iint_0^\infty \frac{v^2}{(v+s)^2}\rho_\xi(s)\rho_\xi(v)\mathrm{d}s\mathrm{d}v. \tag{69}$$

The value of this integral depends on the form of ρ_ξ. Plugging (67)-(69) in (64) gives:

$$\begin{aligned} E|x_{eq}|^2 &= \sum_{k=0}^\infty \frac{1}{2^{k+1}}\left[\iint_0^\infty \frac{4hv^2}{(v+s)^2}\rho_\xi(s)\rho_\xi(v)\mathrm{d}s\mathrm{d}v + kh^2 + k^2h^2\right] \\ &= \frac{1}{2}\iint_0^\infty \frac{4hv^2}{(v+s)^2}\rho_\xi(s)\rho_\xi(v)\mathrm{d}s\mathrm{d}v\sum_{k=0}^\infty\frac{1}{2^k} + \frac{h^2}{2}\sum_{k=0}^\infty\frac{k}{2^k} + \frac{h^2}{2}\sum_{k=0}^\infty\frac{k^2}{2^k} \\ &= \iint_0^\infty \frac{4hv^2}{(v+s)^2}\rho_\xi(s)\rho_\xi(v)\mathrm{d}s\mathrm{d}v + 4h^2. \end{aligned} \tag{70}$$

It follows that

$$\mathrm{Var}(|e_{eq}|) = E|x_{eq}|^2 - (E|x_{eq}|)^2 = \iint_0^\infty \frac{4hv^2}{(v+s)^2}\rho_\xi(s)\rho_\xi(v)\mathrm{d}s\mathrm{d}v + \frac{7}{4}h^2, \tag{71}$$

which proves the Theorem.

The result in Theorem 4.1.5 can be extended to the case where the particle's initial position does not coincide with a particular gridpoint (that is, in the case that Assumption (B3) is dropped). Suppose that the particle's initial position is $x(t_0) = z(t_0) \in (x_k, x_{k+1}]$. There are then 4 possible cases, depending on the values of $\xi_k = f(x_k)$ and $\xi_{k+1} = f(x_{k+1})$:

1). $\xi_k > 0$ and $\xi_{k+1} > 0$,

2). $\xi_k < 0$ and $\xi_{k+1} > 0$,

3). $\xi_k > 0$ and $\xi_{k+1} < 0$,

4). $\xi_k < 0$ and $\xi_{k+1} < 0$.

Let c be a random variable which labels the above cases; c takes values in the set $\{1, 2, 3, 4\}$, with $\mathbf{Pr}(c = i) = \frac{1}{4}$ for all i. The expected value of $|x_{eq} - x(t_0)|$ may be calculated using conditional expectations:

$$E(|x_{eq} - x(t_0)|) = \frac{1}{4} \sum_{i=1}^{4} E(|x_{eq} - x(t_0)| \, \big| \, c = i). \tag{72}$$

Theorem 4.1.7 *The expected value of $|x_{eq} - x(t_0)|$ is independent of initial conditions, that is,*

$$E(|x_{eq} - x(t_0)|) = 3h/2 \tag{73}$$

for arbitrary $x(t_0) = z(t_0)$.

Proof: Theorem 4.1.7 can be proved by calculating $E(|x_{eq} - x(t_0)| \, \big| \, c = i)$ for each case in turn.

To begin, consider Case 1) ($\xi_k > 0$ and $\xi_{k+1} > 0$). By monotonicity of f on (x_k, x_{k+1}), $f(x) > 0$ for all $x \in (x_k, x_{k+1}]$; it is clear, then, that the particle moves in the positive x-direction until it passes x_{k+1}. The expected distance to the nearest equilibrium is then

$$E(x_{eq} - x(t_0)) = E(x_{eq} - x_{k+1}) + x_{k+1} - x(t_0), \tag{74}$$

where $x_{k+1} > 0$ is given. Shifting the origin to x_{k+1} and applying Theorem 4.1.5 gives $E(x_{eq} - x_{k+1}) = 3h/2$. Plugging this back into (74) gives:

$$E(|x_{eq} - x(t_0)| \, \big| \, c = 1) = 3h/2 + (x_{k+1} - x(t_0)). \tag{75}$$

Case 4) ($\xi_k < 0$ and $\xi_{k+1} < 0$) is analogous to Case 1); this time however, $f(x) < 0$ for all $x \in (x_k, x_{k+1}]$. The particle moves in the negative x-direction until it passes x_k, therefore

$$E(|x_{eq} - x(t_0)| \, \big| \, c = 4) = (x(t_0) - x_k) + 3h/2. \tag{76}$$

Next consider Case 2) ($\xi_k < 0$ and $\xi_{k+1} > 0$). The expectation can be calculated as follows:

$$\begin{aligned} E(|x_{eq} - x(t_0)| \,\big|\, c = 2) = E(|x_{eq} - x(t_0)| \,\big|\, c = 2,\ f(x(t_0)) > 0)\mathbf{Pr}(f(x(t_0)) > 0) \\ + E(|x_{eq} - x(t_0)| \,\big|\, c = 2,\ f(x(t_0)) < 0)\mathbf{Pr}(f(x(t_0)) < 0). \end{aligned} \tag{77}$$

If $f(x(t_0)) = f(z(t_0)) > 0$, then $f(x) > 0$ for all $x \in (x(t_0), x_{k+1}]$; so the particle moves in the positive direction until it passes x_{k+1}. As in Case 1), the expected value of $|x_{eq} - x(t_0)|$ is then $3h/2 + (x_{k+1} - x(t_0))$. If, on the other hand, $f(x(t_0)) = f(z(t_0)) < 0$, then $f(x) < 0$ for all $x \in (x_k, x(t_0))$, and the particle moves in the negative direction until it passes x_k. As in case 4), the expected value of $|x_{eq} - x(t_0)|$ is then $(x(t_0) - x_k) + 3h/2$. Therefore (77) can be rewritten as

$$\begin{aligned} E(|x_{eq} - x(t_0)| \,\big|\, c = 2) &= \left(\frac{3h}{2} + (x_{k+1} - x(t_0))\right)\mathbf{Pr}(f(x(t_0)) > 0) \\ &\quad + \left(\frac{3h}{2} + (x(t_0) - x_k)\right)(1 - \mathbf{Pr}(f(x(t_0)) > 0)) \\ &= \left(\frac{3h}{2} + x(t_0) - x_k\right) + (h - 2(x(t_0) - x_k))\mathbf{Pr}(f(x(t_0)) > 0). \end{aligned} \tag{78}$$

It remains only to calculate the probability $\mathbf{Pr}(f(x(t_0)) > 0)$. Let $y_0 := x(t_0) - x_k$ ($y_0 \in (0, h]$). Using (28), one can write:

$$\begin{aligned} \mathbf{Pr}(f(y_0) > 0 | \xi_k < 0, \xi_{k+1} > 0) &= \mathbf{Pr}\left(\frac{y_0\xi_{k+1} + (h - y_0)\xi_k}{h} > 0 \,\middle|\, \xi_k < 0, \xi_{k+1} > 0\right) \\ &= \mathbf{Pr}\left(\xi_{k+1} > \frac{y_0 - h}{y_0}\xi_k \,\middle|\, \xi_k < 0, \xi_{k+1} > 0\right). \end{aligned} \tag{79}$$

This can be calculated, using the fact that $\xi_k < 0$ and $\xi_{k+1} > 0$, as

$$\mathbf{Pr}\left(\xi_{k+1} > \frac{y_0 - h}{y_0}\xi_k \,\middle|\, \xi_k < 0, \xi_{k+1} > 0\right) = \int_{-\infty}^{0}\left(\int_{\frac{y_0 - h}{y_0}s}^{\infty} \rho_\xi(r)dr\right)\rho_\xi(s)\mathrm{d}s. \tag{80}$$

Lastly, consider Case 3) ($\xi_k > 0$ and $\xi_{k+1} < 0$). By Lemma 4.1.1, there is a stable equilibrium $x_{eq} \in (x_k, x_{k+1})$ where $f(x_{eq}) = 0$. By monotonicity of f within one interval, if

$f(x(t_0)) < 0$ then $x(t_0) > x_{eq}$, and if $f(x(t_0)) > 0$ then $x_{eq} > x(t_0)$. Therefore,

$$\begin{aligned} E(|x_{eq} - x(t_0)||c = 3) &= E(x_{eq} - x(t_0))\mathbf{Pr}(f(x(t_0)) > 0) + E(x(t_0) - x_{eq})\mathbf{Pr}(f(x(t_0)) < 0) \\ &= (x_k + h/2 - x(t_0))\mathbf{Pr}(f(x(t_0)) > 0) \\ &\quad + (x(t_0) - (x_k + h/2))(1 - \mathbf{Pr}(f(x(t_0)) > 0)) \\ &= 2((x_k + h/2) - x(t_0))\mathbf{Pr}(f(x(t_0)) > 0) - ((x_k + h/2) - x(t_0)), \end{aligned} \tag{81}$$

where $\mathbf{Pr}(f(x(t_0)) > 0)$ denotes

$$\mathbf{Pr}(f(x(t_0)) > 0 | \xi_k > 0, \xi_{k+1} < 0).$$

This probability can be calculated analogously to the probability in Case 2) (using $y_0 := x(t_0) - x_k$):

$$\mathbf{Pr}(f(y_0) > 0 | \xi_k > 0, \xi_{k+1} < 0) = 1 - \int_0^\infty \left(\int_{-\infty}^{\frac{y_0 - h}{y - 0} s} \rho_\xi(r) \mathrm{d}r \right) \rho_\xi(s) \mathrm{d}s. \tag{82}$$

Using the fact that ρ_ξ is a symmetric function and applying change of variables $r' = -r$ and $s' = -s$, the above may be rewritten as

$$\begin{aligned} \mathbf{Pr}(f(y_0) > 0 | \xi_k > 0, \xi_{k+1} < 0) &= 1 - \int_{-\infty}^0 \left(\int_{\frac{y_0 - h}{y - 0} s}^\infty \rho_\xi(r) \mathrm{d}r \right) \rho_\xi(s) \mathrm{d}s \\ &= 1 - \mathbf{Pr}(f(y_0) > 0 | \xi_k < 0, \xi_{k+1} > 0). \end{aligned} \tag{83}$$

Plugging (75),(76),(78), and (81) into (72) gives

$$E(|x_{eq} - x(t_0)|) = 3h/2, \tag{84}$$

which is independent of the value of $x(t_0)$. This proves Theorem 4.1.7.

4.2 The Two-Dimensional Case

In the previous section, it has been shown that, in the one-dimensional case, $E(|x_{eq} - z(t_0)|) = 3h/2$. This result can be generalized to the two-dimensional case. The assumptions for this case are as follows:

(C1) The particle moves in the horizontal plane (the domain of $\mathbf{f}$ is $\mathbb{R}^2$).

(C2) The ocean model outputs an estimate $\mathbf{F}_M$ of the flow $\mathbf{F}_R$ at each gridpoint on a uniform square grid over $\mathbb{R}^2$ with gridsize h, where $\mathbf{x}_{k,l} = [kh,\ lh]^{\mathrm{T}}$ is a gridpoint indexed by (k, l). The values of $\mathbf{f}(\mathbf{x}) = \mathbf{F}_M(\mathbf{x}) - \mathbf{F}_R(\mathbf{x})$ at the grid points are iid symmetrically-distributed random variables, denoted by $\vec{\xi}_{k,l} = [\xi^1_{k,l}\ \xi^2_{k,l}]^{\mathrm{T}}$ (where $\xi^1_{k,l} = f^1(\mathbf{x}_{k,l})$ and $\xi^2_{k,l} = f^2(\mathbf{x}_{k,l})$ are mutually independent). The pdf of $\xi^i_{k,l}$, where $i = 1, 2$, is denoted by ρ_ξ.

(C3) The initial position of the particle in simulation is equal to the initial position of the physical particle: $\mathbf{z}(t_0) = \mathbf{x}(t_0)$.

Analogous to the one-dimensional case, values of $\mathbf{f}$ at any point can be approximated by taking the bilinear interpolation of grid point values; for $\mathbf{x} = [x^1\ x^2]^{\mathrm{T}} \in (kh, (k+1)h) \times (lh, (l+1)h)$, $\mathbf{f}$ is given by

$$\begin{aligned}\mathbf{f}(\mathbf{x}) = \frac{1}{h^2}\Big\{\Big[&\vec{\xi}_{k,l}((k+1)h - x^1)((l+1)h - x^2) + \vec{\xi}_{k+1,l}(x^1 - kh)((l+1)h - x^2) \\ &+ \vec{\xi}_{k,l+1}((k+1)h - x^1)(x^2 - lh) + \vec{\xi}_{k+1,l+1}(x^1 - kh)(x^2 - lh)\Big]\Big\}.\end{aligned} \tag{85}$$

In two dimensions, the particle exhibits a much richer range of behaviors than a particle confined to move on a line, and it becomes more difficult to find $\lim_{t\to\infty} \mathbf{x}(t) = \mathbf{x}_{eq}$. Instead, this value can be approximated by finding a lower bound on $E(|\mathbf{x}_{eq} - \mathbf{x}(t_0)|)$ as $E(|\mathbf{x}_* - \mathbf{x}(t_0)|)$, where $\mathbf{x}_*$ is defined as the smallest (w.r.t. the 1-norm in $\mathbb{R}^2$) equilibrium of the flow $\mathbf{f}$ which satisfies the necessary stability condition $\partial \mathbf{f}^i / \partial \mathbf{x}^i < 0$ for $i = 1, 2$:

$$\mathbf{x}_* = \mathrm{argmin}_{\mathbf{x}\in\mathbb{R}^2} \left\{ \| \mathbf{x} - \mathbf{x}(\mathrm{t}_0) \|_1 : \partial \mathbf{f}^{\mathrm{i}} / \partial \mathbf{x}^{\mathrm{i}}(\mathbf{x}) < 0 \ \ \forall \mathrm{i} \right\}. \tag{86}$$

Figure 4 shows the zero level sets of $\mathbf{f}^1(\mathbf{x})$. Computing the ℓ^1-norm to the nearest equilibrium requires finding the distance to the nearest intersect of the zero level sets of $\mathbf{f}^1(\mathbf{x})$ with those of $\mathbf{f}^2(\mathbf{x})$.

The main contribution of this section is summarized in the following theorem:

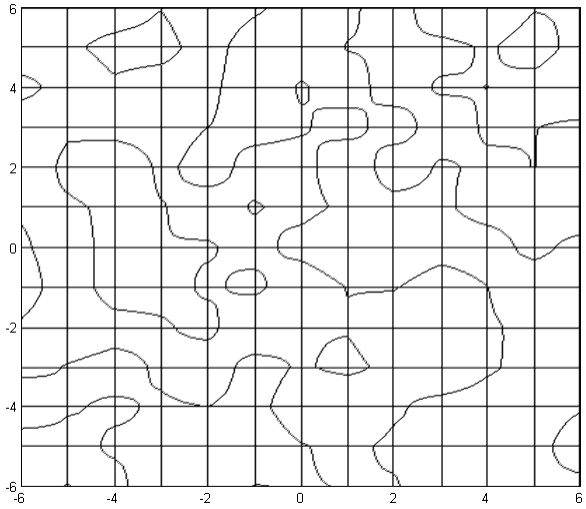

Figure 4: Zero level set of the error flow in the x-direction, $\mathbf{f}^1(\mathbf{x}) = 0$. Equilibria of $\mathbf{f}(\mathbf{x})$ lie on intersections of the zero level sets for flow in the x- and y-directions.

Theorem 4.2.1 *The expected value of the 1-norm of the steady-state position-prediction error, given by* $\| \mathbf{x}_* \|_1$*, satisfies:*

$$
\begin{aligned}
&E(\| \mathbf{x}_* - \mathbf{x}(t_0) \|_1) \leq \\
&2 \sum_{k=0}^{\infty} \Bigg\{ \frac{2(k+1)h}{4^{k+1}} \int_{-kh}^{-(k+1)h} \int_0^{\infty} \frac{4hv}{x^i} \rho_\xi(v) \rho_\xi(v(1 - h/x^i)) \mathrm{d}v \mathrm{d}x^i \\
&\qquad + \frac{2k}{4^{k+1}} \int_{-kh}^{-(k+1)h} \int_0^{\infty} \frac{4hv}{x^i} \rho_\xi(v) \rho_\xi(v(1 - h/x^i)) \\
&\qquad \times \left[1 - \int_0^{|x^i|-kh} \int_0^{\infty} \frac{4hv}{u^2} \rho_\xi(v) \rho_\xi(v(1 - h/u)) \mathrm{d}v \mathrm{d}u \right] \mathrm{d}v \mathrm{d}x^i \Bigg\}
\end{aligned}
\tag{87}
$$

where h is the grid size used by the ocean model. In particular, if ρ_ξ *is Gaussian,*

$$E(\| \mathbf{x}_* - \mathbf{x}(t_0) \|_1) \leq 2.52h. \tag{88}$$

The proof of this theorem requires a sequence of lemmas, which are proved below. As in the one-dimensional case, the following variables are introduced for convenience:

$$x_+^i = \mathrm{argmin}_{x^i > 0} \{ |x^i| : f^i(x^i \hat{\mathbf{e}}_i) = 0, \partial f^i / \partial x^i < 0 \} \tag{89}$$

$$x_-^i = \mathrm{argmin}_{x^i < 0} \{ |x^i| : f^i(x^i \hat{\mathbf{e}}_i) = 0, \partial f^i / \partial x^i < 0 \}, \tag{90}$$

where $\hat{\mathbf{e}}_i$ is the standard i^{th} basis vector in $\mathbb{R}^2$.

Lemma 4.2.2 *The value of* $\mathbf{Pr}(x^i_- \in (-(k+1)h, -kh) | \xi^i_{0,0} > 0)$ *is* $k\left(\frac{1}{2}\right)^{k+1}$.

Proof: The variable x^i_- represents the first stable 0 of f^i, evaluated on $(-\infty, 0)$ in the direction i. Without loss of generality, let $i = 1$ (x-axis). Along the axis, f^1 is a linear interpolation of its values at the points $\{0, \pm h, \pm 2h, \ldots\}$. By Lemma 4.1.3, the smallest stable equilibrium of f^1 on $(-\infty, 0)$ must lie in the first interval $((-(k+1)h, -kh))$ with $\xi^1_{-(k+1),0} > 0$ and $\xi^1_{-k,0} < 0$.

Since $\xi^1_{0,0} > 0$ by assumption, $\mathbf{Pr}(x^1_- \in (-h, 0)) = 0$. Let

$$\xi^1_{-j,0} = \min_{l \in \mathbb{Z}^+} \{\xi_{-l} : \xi_{-l} < 0\}$$

be the first negative gridpoint flow value. Then

$$\mathbf{Pr}(x^1_- \in (-(k+1)h, -kh) | \xi^i_{0,0} > 0) = \mathbf{Pr}(\xi^1_{-(k+1),0} > 0) \sum_{j=1}^{k} \Big(\prod_{m=j}^{k} \mathbf{Pr}(\xi^1_{-m,0} < 0) \prod_{l=1}^{j-1} \mathbf{Pr}(\xi^1_{-l,0} > 0) \Big). \tag{91}$$

By symmetry of the distribution of $\xi^1_{n,0}$, $\mathbf{Pr}(\xi^1_{n,0} > 0) = \mathbf{Pr}(\xi^1_{n,0} < 0) = 1/2$ for all n. The above equation therefore simplifies to

$$\mathbf{Pr}(x^1_- \in (-(k+1)h, -kh) | \xi^i_{0,0} > 0) = \sum_{i=1}^{k} \left(\frac{1}{2}\right)^{k+1} = k\left(\frac{1}{2}\right)^{k+1}. \tag{92}$$

The calculation for x^2_- is analogous. This proves the Lemma.

Lemma 4.2.3 *The value of* $\mathbf{Pr}(x^i_+ > (k+1)h | \xi^i_{0,0} > 0)$ *is* $\left(\frac{1}{2}\right)^{k+1}$.

Proof: The variable x^i_+ represents the first stable 0 of f^i, evaluated on the line corresponding to direction i. As in Lemma 4.2.2, let $i = 1$ (x-axis). By Lemma 4.1.3, the smallest stable 0 of f^1 on $(0, \infty)$ must lie in the first interval $(mh, (m+1)h)$ with $\xi^1_{m,0} > 0$ and $\xi^1_{m+1,0} < 0$. Therefore, since $\xi^1_{0,0} > 0$ by assumption, $\mathbf{Pr}(x^1_+ > (k+1)h)$ is equal to the probability that $\xi^1_{i,0} > 0$ for all $i \in \{1, ..., k+1\}$. Using the fact that $\xi^1_{n,0}$ are independent and symmetrically distributed gives:

$$\mathbf{Pr}(x^1_+ > (k+1)h | \xi^i_{0,0} > 0) = \prod_{i=1}^{k+1} \mathbf{Pr}(\xi^1_{i,0} > 0) = \left(\frac{1}{2}\right)^{k+1} \tag{93}$$

The calculation for x^2_+ is analogous. This proves the Lemma.

Lemma 4.2.4 *The value of* $\mathbf{Pr}(x_+^i \in (kh,(k+1)h)|\xi_{0,0}^i > 0)$ *is* $\left(\frac{1}{2}\right)^{k+1}$.

Proof: The proof is almost identical to that of Lemma 4.2.3. Let $i = 1$ (x-axis). By Lemma 4.1.3, the smallest stable 0 of f^1 on $(0,\infty)$ must lie in the first interval $(kh,(k+1)h)$ with $\xi_{k,0}^1 > 0$ and $\xi_{k+1,0}^1 < 0$. Therefore, since $\xi_{0,0}^1 > 0$ by assumption, $\mathbf{Pr}(x_+^1 > (k+1)h)$ is equal to the probability that $\xi_{i,0}^1 > 0$ for all $i \in \{1,...,k\}$, and $\xi_{k+1,0}^1 < 0$. Using the fact that $\xi_{n,0}^1$ are independent and symmetrically distributed gives:

$$\mathbf{Pr}(x_+^1 > (k+1)h|\xi_{0,0}^i > 0) = \prod_{i=1}^{k} \mathbf{Pr}(\xi_{i,0}^1 > 0)\mathbf{Pr}(\xi_{k+1,0}^1 < 0) = \left(\frac{1}{2}\right)^{k+1}. \tag{94}$$

The calculation for x_+^2 is analogous. This proves the Lemma.

Lemma 4.2.5 *The probability that* x_* *lies in the interval* $(-(k+1)h,-kh)$ *is*

$$\mathbf{Pr}(x_* = x_-^i, x_-^i \in (-(k+1)h,-kh)|\xi_{0,0}^i > 0) = \frac{k}{4^{k+1}} + \frac{k}{4^{k+1}}\left(1 - \int_0^{|x_-^i|-kh} \frac{4h}{u^2}\left(\int_0^\infty v\rho_\xi(v)\rho_\xi(v(1-h/u))\mathrm{d}v\right)\mathrm{d}u\right). \tag{95}$$

Proof: The value of $\mathbf{Pr}(x_* = x_-^i, x_-^i \in (-(k+1)h,-kh)|\xi_{0,0}^i > 0)$ is given by

$$\mathbf{Pr}(x_* = x_-^i, x_-^i \in (-(k+1)h,-kh)|\xi_{0,0}^i > 0) = \mathbf{Pr}(|x_-^i| < |x_+^i|, x_-^i \in (-(k+1)h,-kh)|\xi_{0,0}^i > 0). \tag{96}$$

The dependence on ξ_0 will not be written in future equations to avoid notational clutter, but will be assumed. The variables x_-^i and x_+^i are mutually independent, so that

$$\mathbf{Pr}(|x_-^i| < |x_+^i|, x_-^i \in (-(k+1)h,-kh)) =$$
$$\mathbf{Pr}(x_-^i \in (-(k+1)h,-kh))\mathbf{Pr}(x_+^i > (k+1)h) + \mathbf{Pr}(x_-^i \in (-(k+1)h,-kh))\mathbf{Pr}(x_+^i \in (|x_-^i|,(k+1)h)), \tag{97}$$

where

$$\mathbf{Pr}(x_+^i \in (|x_-^i|,(k+1)h)) = \mathbf{Pr}(x_+^i \in (|x_-^i|,(k+1)h)|x_+^i \in (kh,(k+1)h))\mathbf{Pr}(x_+^i \in (kh,(k+1)h)). \tag{98}$$

Thus,

$$\mathbf{Pr}(|x_-^i| < |x_+^i|, x_-^i \in (-(k+1)h, -kh)) = \mathbf{Pr}(x_-^i \in (-(k+1)h, -kh))\mathbf{Pr}(x_+^i > (k+1)h)$$
$$+\mathbf{Pr}(x_-^i \in (-(k+1)h, -kh))\mathbf{Pr}(x_+^i \in (|x_-^i|, (k+1)h)|x_+^i \in (kh, (k+1)h))\mathbf{Pr}(x_+^i \in (kh, (k+1)h)). \tag{99}$$

Using Lemmas 4.2.2-4.2.4, the above can be written as

$$\mathbf{Pr}(|x_-^i| < |x_+^i|, x_-^i \in (-(k+1)h, -kh)) = \left(\frac{k}{4^{k+1}}\right) + \left(\frac{k}{4^{k+1}}\right)\mathbf{Pr}(x_+^i \in (|x_-^i|, (k+1)h)|x_+^i \in (kh, (k+1)h)). \tag{100}$$

The remaining expression, $\mathbf{Pr}(x_+^i \in (|x_-^i|, (k+1)h)|x_+^i \in (kh, (k+1)h))$, may be calculated as follows:

$$\begin{aligned}\mathbf{Pr}(x_+^i \in (|x_-^i|, (k+1)h)|x_+^i \in (kh, (k+1)h)) &= 1 - \mathbf{Pr}(x_+^i \in (kh, |x_-^i|)|x_+^i \in (kh, (k+1)h)) \\ &= 1 - \int_{kh}^{|x_-^i|} \rho_{x_-^i}(x)\mathrm{d}x,\end{aligned} \tag{101}$$

where $x_-^i \in (kh, (k+1)h)$. Using the change of variables

$$\begin{aligned}u &= x - kh \\ v &= \xi_{k,0}^i\end{aligned} \tag{102}$$

and the distribution for $u_* = x_* - x_k = x_+ - kh$ derived in the one-dimensional case (see (50)),

$$\mathbf{Pr}(x_+^i \in (|x_-^i|, (k+1)h)|x_+^i \in (kh, (k+1)h)) = 1 - \int_0^{|x_-^i|-kh} \frac{4h}{u^2}\left(\int_0^\infty v\rho_\xi(v)\rho_\xi(v(1-h/u))\mathrm{d}v\right)\mathrm{d}u. \tag{103}$$

Plugging this expression into (100) gives:

$$\mathbf{Pr}(x_* = x_-^i, x_-^i \in (-(k+1)h, -kh)) = \frac{k}{4^{k+1}} + \frac{k}{4^{k+1}}\left(1 - \int_0^{|x_-^i|-kh} \frac{4h}{u^2}\left(\int_0^\infty v\rho_\xi(v)\rho_\xi(v(1-h/u))\mathrm{d}v\right)\mathrm{d}u\right). \tag{104}$$

This proves the Lemma.

Lemma 4.2.6 *The probability that x_* lies in the interval $(kh, (k+1)h)$ is:*

$$\mathbf{Pr}(x_* = x_+^i, x_+^i \in (kh,(k+1)h)|\xi_{0,0}^i > 0) = \frac{k+2}{4^{k+1}} + \frac{k}{4^{k+1}}\left(1 - \int_0^{x_+^i - kh} \frac{4h}{u^2}\left(\int_0^\infty v\rho_\xi(v)\rho_\xi(v(1-h/u))\mathrm{d}v\right)\mathrm{d}u\right). \quad (105)$$

Proof: The value of $\mathbf{Pr}(x_* = x_+^i, x_+^i \in (kh,(k+1)h)|\xi_{0,0}^i > 0)$ is given by

$$\mathbf{Pr}(x_* = x_+^i, x_+^i \in (kh,(k+1)h)|\xi_{0,0}^i > 0) = \mathbf{Pr}(|x_+^i| < |x_-^i|, x_+^i \in (kh,(k+1)h)|\xi_{0,0}^i > 0). \quad (106)$$

For notational convenience, the conditioning variable $\xi_{0,0}^i$ will be dropped subsequent equations. Using independence of x_-^i and x_+^i, the above equations may be written as

$$\begin{aligned}\mathbf{Pr}(|x_+^i| < |x_-^i|, x_+^i \in (kh,(k+1)h)) &= \mathbf{Pr}(x_+^i \in (kh,(k+1)h))\mathbf{Pr}(x_-^i < -(k+1)h) \\ &+ \mathbf{Pr}(x_+^i \in (kh,(k+1)h))\mathbf{Pr}(x_-^i \in (-(k+1)h, -x_+^i)|x_-^i \in (-(k+1)h,-kh)) \\ &\times \mathbf{Pr}(x_-^i \in (-(k+1)h,-kh)).\end{aligned} \quad (107)$$

By Lemmas 4.2.2 and 4.2.4,

$$\begin{aligned}\mathbf{Pr}(x_+^i \in (kh,(k+1)h)) &= \left(\frac{1}{2}\right)^{k+1} \\ \mathbf{Pr}(x_-^i \in (-(k+1)h,-kh)) &= k\left(\frac{1}{2}\right)^{k+1}\end{aligned} \quad (108)$$

and

$$\begin{aligned}\mathbf{Pr}(x_-^i < -(k+1)h) &= 1 - \sum_{j=0}^{k} \mathbf{Pr}(x_-^i \in (-(j+1)h, -jh)) \\ &= 1 - \sum_{j=0}^{k} j\left(\frac{1}{2}\right)^{j+1} \\ &= (k+2)\left(\frac{1}{2}\right)^{k+1}.\end{aligned} \quad (109)$$

Then using change of variables

$$\begin{aligned}u &= x + (k+1)h \\ v &= \xi_{k,0}^i\end{aligned} \quad (110)$$

and the distribution for $u_* = x_* - x_{-(k+1)} = x_+ + (k+1)h$ in (50), $\mathbf{Pr}(x_-^i \in (-(k+1)h, -x_+^i) | x_-^i \in (-(k+1)h, -kh))$ can be calculated analogously to $\mathbf{Pr}(x_+^i \in (|x_-^i|, (k+1)h) | x_+^i \in (kh, (k+1)h))$ to give:

$$\mathbf{Pr}(x_-^i \in (-(k+1)h, -x_+^i) | x_-^i \in (-(k+1)h, -kh)) = 1 - \int_0^{x_+^i - kh} \frac{4h}{u^2} \left(\int_0^\infty v \rho_\xi(v) \rho_\xi(v(1-h/u)) \mathrm{d}v \right) \mathrm{d}u, \quad (111)$$

so that

$$\mathbf{Pr}(x_* = x_+^i, x_+^i \in (kh, (k+1)h)) = \frac{k+2}{4^{k+1}} + \frac{k}{4^{k+1}} \left(1 - \int_0^{x_+^i - kh} \frac{4h}{u^2} \left(\int_0^\infty v \rho_\xi(v) \rho_\xi(v(1-h/u)) \mathrm{d}v \right) \mathrm{d}u \right). \quad (112)$$

This proves the Lemma.

The proof of Theorem 4.2.1 is given below.

The ℓ^1 norm of $\mathbf{x}_*$ is $|x_*^1| + |x_*^2|$. By assumption, the flows along the x- and y-axes are mutually independent. The expected value of $|x_*^i|$, for $i = 1, 2$, will be computed along each dimension independently.

First, note that the value of $E(|x_{*,i} - x_i(t_0)|)$ is independent of the initial position $\mathbf{x}(t_0)$. This can be shown as follows:

First, use a shift the coordinates; for $x_i(t_0) \in [kh, (k+1)h)$, let $x \mapsto x' = x - kh$ so that $x_i'(t_0) \in [0, h)$. Then

$$\begin{aligned} E(|x_{*,i} - x_i(t_0)|) &= E(|x'_{*,i} - x_i'(t_0)|) \\ &= E(x'_{*,i} - x_i'(t_0) | x'_{*,i} = x_i^+ > 0) \mathbf{Pr}(x'_{*,i} = x_i^+) \\ &\quad + E(x'_{*,i} + x_i'(t_0) | x'_{*,i} = x_i^- < 0) \mathbf{Pr}(x'_{*,i} = x_i^-) \\ &= E(x'_{*,i}) - x_i'(t_0) \mathbf{Pr}(x'_{*,i} = x_i^+) + x_i'(t_0) \mathbf{Pr}(x'_{*,i} = x_i^-) \\ &= E(x'_{*,i}) - \frac{1}{2} x_i'(t_0) + \frac{1}{2} x_i'(t_0), \\ &= E(x'_{*,i}), \end{aligned} \quad (113)$$

which is the expected value of $E(|x_{*,i} - x_i(t_0)|)$ when $\mathbf{x}(t_0) = 0$. Without loss of generality, it will therefore be assumed for the remainder of this proof that $\mathbf{x}(t_0) = \mathbf{z}(t_0) = 0$.

Consider the motion along one axis. Let ξ^i_k, for $i = 1, 2$, denote the the values of $\xi^i_{i,j}$ along the i^{th} axis; so that $\xi^1_k = \xi^1_{k,0}$ and $\xi^2_k = \xi^2_{0,k}$. As in the one-dimensional case, one can write:

$$E(|x^i_*|) = \frac{1}{2}\int_{-\infty}^{\infty} |x^i|\rho_{|x^i_*|}(x^i|\xi^i_0 > 0)\mathrm{d}x^i + \frac{1}{2}\int_{-\infty}^{\infty} |x^i|\rho_{|x^i_*|}(x^i|\xi^i_0 < 0)\mathrm{d}x^i. \tag{114}$$

This case differs from the one-dimensional case, however, in that Lemmas 4.1.3 and 4.1.4 no longer hold, since the particle is moving in two dimensions, and may therefore circumvent the region of positive (or negative) flow around $x^i = 0$ by moving along the perpendicular directions.

It follows from the symmetry of ρ_ξ that $\int_{-\infty}^{\infty} |x^i|\rho_{|x^i_*|}(x^i|\xi^i_0 > 0)\mathrm{d}x^i = \int_{-\infty}^{\infty} |x^i|\rho_{|x^i_*|}(x^i|\xi^i_0 < 0)\mathrm{d}x^i$. Thus,

$$E(|x^i_*|) = \int_{-\infty}^{\infty} |x^i|\rho_{|x^i_*|}(x^i|\xi^i_0 > 0)\mathrm{d}x^i. \tag{115}$$

Note that $x^i_* = \mathrm{argmin}_{x^i_+, x^i_-}\{|x|\}$, therefore

$$\begin{aligned}
E(|x^i_*|) &= \sum_{k=0}^{\infty}\int_{-(k+1)h}^{-kh} |x^i|\rho_{|x^i_*|}(x^i|\xi^i_0 > 0, \mathrm{d}1)\mathbf{Pr}(\mathrm{d}1|\xi^i_0 > 0)\mathrm{d}x^i \\
&\quad + \sum_{k=0}^{\infty}\int_{x^i_k}^{x^i_k+h} |x^i|\rho_{|x^i_*|}(x^i|\xi^i_0 > 0, \mathrm{d}2)\mathbf{Pr}(\mathrm{d}2|\xi^i_0 > 0)\mathrm{d}x^i \\
&= \sum_{k=0}^{\infty}\int_{-kh}^{-(k+1)h} x^i\rho_{|x^i_*|}(x^i|\xi^i_0 > 0, \mathrm{d}1)\mathbf{Pr}(\mathrm{d}1|\xi^i_0 > 0)\mathrm{d}x^i \\
&\quad + \sum_{k=0}^{\infty}\int_{x^i_k}^{x^i_k+h} x^i\rho_{|x^i_*|}(x^i|\xi^i_0 > 0, \mathrm{d}2)\mathbf{Pr}(\mathrm{d}2|\xi^i_0 > 0)\mathrm{d}x^i,
\end{aligned} \tag{116}$$

where the shorthand d1 has been adopted for the condition "$x_* = x^i_-,\ x^i_- \in (-(k+1)h, -kh)$" and d2 for "$x_* = x^i_+,\ x^i_+ \in (kh, (k+1)h)$".

Using Lemmas 4.2.5 and 4.2.6, and applying change of variables

$$\begin{aligned}
u &= x - \left\lfloor \frac{x}{h} \right\rfloor h \\
v &= \xi^i_{\lfloor \frac{x}{h} \rfloor},
\end{aligned} \tag{117}$$

(116) can be written as

$$
\begin{aligned}
&E(|x_*^i|) = \\
&\sum_{k=0}^{\infty} \Bigg\{ \frac{k}{4^{k+1}} \int_{-kh}^{-(k+1)h} x^i \rho_{|x_*^i|}(x^i|\xi_0^i > 0, \mathrm{d}1)\mathrm{d}x^i \\
&+ \frac{k}{4^{k+1}} \int_{-kh}^{-(k+1)h} x^i \rho_{|x_*^i|}(x^i|\xi_0^i > 0, \mathrm{d}1) \\
&\qquad \times \left[1 - \int_0^{|x^i|-kh} \frac{4h}{u^2} \left(\int_0^{\infty} v \rho_\xi(v) \rho_\xi(v(1-h/u)) \mathrm{d}v \right) \mathrm{d}u \right] \mathrm{d}x^i \\
&+ \frac{k+2}{4^{k+1}} \int_{kh}^{(k+1)h} x^i \rho_{|x_*^i|}(x^i|\xi_0^i > 0, \mathrm{d}2)\mathrm{d}x^i \\
&+ \frac{k}{4^{k+1}} \int_{kh}^{(k+1)h} x^i \rho_{|x_*^i|}(x^i|\xi_0^i > 0, \mathrm{d}2) \\
&\qquad \times \left[1 - \int_0^{x^i-kh} \frac{4h}{u^2} \left(\int_0^{\infty} v \rho_\xi(v) \rho_\xi(v(1-h/u)) \mathrm{d}v \right) \mathrm{d}u \right] \mathrm{d}x^i \Bigg\}.
\end{aligned} \tag{118}
$$

Using the symmetry of ρ_ξ the terms in the above equation can be combined to obtain:

$$
\begin{aligned}
E(|x_*^i|) = \sum_{k=0}^{\infty} \Bigg\{ &\frac{2(k+1)h}{4^{k+1}} \int_{-kh}^{-(k+1)h} x^i \rho_{|x_*^i|}(x^i|\xi_0^i > 0, \mathrm{d}1)\mathrm{d}x^i \\
&+ \frac{2k}{4^{k+1}} \int_{-kh}^{-(k+1)h} x^i \rho_{|x_*^i|}(x^i|\xi_0^i > 0, \mathrm{d}1) \\
&\times \left[1 - \int_0^{|x^i|-kh} \frac{4h}{u^2} \left(\int_0^{\infty} v \rho_\xi(v) \rho_\xi(v(1-h/u)) \mathrm{d}v \right) \mathrm{d}u \right] \mathrm{d}x^i \Bigg\}.
\end{aligned} \tag{119}
$$

Substituting in the pdf derived in (50) gives:

$$
\begin{aligned}
E(|x_*^i|) = \sum_{k=0}^{\infty} \Bigg\{ &\frac{2(k+1)h}{4^{k+1}} \int_{-kh}^{-(k+1)h} \int_0^{\infty} \frac{4hv}{x^i} \rho_\xi(v) \rho_\xi(v(1-h/x^i)) \mathrm{d}v \mathrm{d}x^i \\
&+ \frac{2k}{4^{k+1}} \int_{-kh}^{-(k+1)h} \int_0^{\infty} \frac{4hv}{x^i} \rho_\xi(v) \rho_\xi(v(1-h/x^i)) \\
&\times \left[1 - \int_0^{|x^i|-kh} \int_0^{\infty} \frac{4hv}{u^2} \rho_\xi(v) \rho_\xi(v(1-h/u)) \mathrm{d}v \mathrm{d}u \right] \mathrm{d}v \mathrm{d}x^i \Bigg\}.
\end{aligned} \tag{120}
$$

The above expression holds for $i = 1, 2$, so $E(|\mathbf{x}_*|_1) = E(|x_*^1| + |x_*^2|) = E(|x_*^1|) + E(|x_*^2|) = 2E(|x_*^i|)$. This proves Theorem 4.2.1 in the general case. If ξ has a Gaussian distribution, the above expression may be evaluated numerically to give

$$
E(|x_*^i|) = 1.26h, \tag{121}
$$

from which it follows that, in this case, $E(|\mathbf{x}_*|) = 2.52h$. This completes the proof of Theorem 4.2.1.

Theorem 4.2.1 gives an expected bound on the ℓ^1 norm of the position estimation error caused by error in the modeled values of the flow in the 2-D case. This gives a range on the bound of the ℓ^2 error as follows:

$$\|\chi\|_1 / \sqrt{2} \leq \|\chi\|_2 \leq \|\chi\|_1 \tag{122}$$

for all $\chi \in \mathbb{R}^2$. In the case that ξ are Gaussian random variables, the lower bound on the ℓ^2 norm of the position estimation error satisfies:

$$E(\|\mathbf{x}_*\|_2) \in [1.78h, 2.52h]. \tag{123}$$

Note that the above calculations do not depend on the strength of the error flow values at the gridpoints, only on the fact that they are independent, identically distributed random variables. The strength (that is, the variance) of the flow, however, does affect the time it takes for the error growth to reach an equilibrium. Since the velocity of the particle in the ocean flow is given by a bilinear interpolation of the flow values at the gridpoints, the higher the variance of the gridpoint values, the higher the mean particle speed; consequently, the faster the particles converge to an equilibrium of the error flow field.

The above approach does not address the coupling between the x and y-position of the expected equilibrium. This coupling is caused by the bilinear interpolation of the gridpoint flow values. Because it is a bilinear interpolation of gridpoint values, the error flow along each of the x and y directions is a continuous function in $\mathbb{R}^2$, with continuous level sets; in particular, the curves $\mathbf{f}^1(\mathbf{x}) = 0$ and $\mathbf{f}^2(\mathbf{x}) = 0$ are continuous curves (see Figure 4). The average distance to the nearest equilibrium, therefore, depends not only on the average distance to an equilibrium along a particular axis, but also on the shape of the zero-level set curve. This can be understood via the following simple example: consider two lines $y = 0$ and $y = h$, with zero-crossings at $x = 1$ and $x = -2$, respectively. The sample mean of the norms of the crossing values is $(|1| + |-2|)/2 = 1.5$. Consider a straight line joining the

two crossing points. The mean distance from the y-axis to this line is $5/6h$. In general, the distance to the zero level set curve along the x and y-directions is less than the expected distance to an equilibrium along a particular line parallel that axis; for this reason, Theorem 4.2.1 gives an upper bound on the true value of $E(\| \mathbf{x}_* \|_1)$ at steady state.

4.3 Eddy Diffusivity Contribution to CLPT Error Growth

The random-flight model (2) is frequently used to model motions of fluid particles in homogeneous, isotropic turbulence. The controlled particle is likewise subject to motion caused by small-scale turbulent flows; in this section the contribution of these turbulence-induced motions to the growth of the CLPT error is considered.

The Langevin equation governing the dynamics of the controlled particle is reproduced here for easy reference:

$$\mathrm{d}\mathbf{x} = (\mathbf{F}_R(\mathbf{x}, t) + \mathbf{u}(\mathbf{x}, t) + \nu)\,\mathrm{d}t \tag{124}$$

$$\mathrm{d}\nu = -A\nu\mathrm{d}t + \Lambda\mathrm{d}\omega. \tag{125}$$

Under the flow-canceling controller, $\mathbf{u}(\mathbf{x}, t)$ is chosen to cancel the estimated flow $\mathbf{F}_M(\mathbf{x}, t) = \mathbf{F}_R(\mathbf{x}, t) + \mathbf{f}(\mathbf{x}, t)$. It is further assumed that the spin parameter $\Omega = 0$, so that $A = \frac{1}{\tau}I$ and $\Lambda = \sigma\sqrt{\frac{2}{\tau}}I$, where I is the identity matrix in $\mathbb{R}^2$. To simplify the notation, let $a = 1/\tau$ and $L = \sigma\sqrt{\frac{2}{\tau}}$. Let $\mathbf{q}$ denote the particle state, $[\mathbf{x},\ \nu]^T$. The total equation for the evolution of $\mathbf{q}$ can be written in standard Ito form as

$$\mathrm{d}\mathbf{q} = \begin{bmatrix} 0 & I \\ 0 & -A \end{bmatrix}\mathbf{q} + \begin{bmatrix} 0 & 0 \\ 0 & \Lambda \end{bmatrix}(\hat{\mathbf{e}}_3\mathrm{d}\omega_1 + \hat{\mathbf{e}}_4\mathrm{d}\omega_2) \tag{126}$$

where $\hat{\mathbf{e}}_i$, $i = 1, \ldots, 4$, are standard basis vectors in $\mathbb{R}^4$, and the initial position of the particle, $\mathbf{x}(t_0)$, is assumed to be 0.

Claim 4.3.1 *The CLPT error growth caused by the stochastic velocity term ν, for the case that $\mathbf{f} \equiv 0$, satisfies:*

$$\| \mathbf{e}_\nu(t) \| \leq \sqrt{\frac{2L}{a^2}}t^{\frac{1}{2}}. \tag{127}$$

when $t > \tau$.

Completing the proof of this claim requires the following two Lemmas:

Lemma 4.3.2 *Let $\psi_2 = \nu^{\mathrm{T}}\nu$, and say $\nu(t_0) = 0$, so that $\psi_2(t_0) = 0$. Then,*

$$E\left(\psi_2(t)\right) = \frac{L}{a}\left(1 - e^{-2at}\right). \tag{128}$$

Proof: The function ψ_2 can be expressed as

$$\psi_2 = \mathbf{q}^{\mathrm{T}} \begin{bmatrix} 0 & 0 \\ 0 & I \end{bmatrix} \mathbf{q}. \tag{129}$$

Using this definition, it can be shown that

$$\frac{\mathrm{d}E\left(\psi_2(t)\right)}{\mathrm{d}t} = -2aE\left(\psi_2\right) + 2L. \tag{130}$$

This is a standard first-order ODE with solution given by

$$E\left(\psi_2(t)\right) = \frac{L}{a}\left(1 - e^{-2at}\right). \tag{131}$$

This proves the Lemma.

Lemma 4.3.3 *Let $\psi_1 = \mathbf{x}^{\mathrm{T}}\nu$, and say $\mathbf{x}(t_0) = \nu(t_0) = 0$, so that $\psi_1(t_0) = 0$. Then,*

$$E\left(\psi_1(t)\right) = \frac{L}{a^2} - \frac{2L}{a^2}e^{-at} + \frac{L}{a^2}e^{-2at}. \tag{132}$$

Proof: Given

$$\psi_1 = \mathbf{x}^{\mathrm{T}}\nu = \mathbf{q}^{\mathrm{T}} \begin{bmatrix} 0 & I \\ 0 & 0 \end{bmatrix} \mathbf{q}, \tag{133}$$

it can be shown that

$$\frac{\mathrm{d}E\left(\psi_1(t)\right)}{\mathrm{d}t} = -aE\left(\psi_1(t)\right) + E\left(\psi_2(t)\right). \tag{134}$$

Using Lemma 4.3.2:

$$\frac{\mathrm{d}E\left(\psi_1(t)\right)}{\mathrm{d}t} = -aE\left(\psi_1(t)\right) + \frac{L}{a}\left(1 - e^{-2at}\right). \tag{135}$$

This non-homogeneous linear ODE can be solved explicitly to get:

$$E\left(\psi_1(t)\right) = e^{-at}\int_0^{\mathrm{T}} e^{as}\frac{L}{2a}\left(1-e^{-2as}\right)\mathrm{d}s \tag{136}$$

$$= \frac{L}{a^2} - \frac{2L}{a^2}e^{-at} + \frac{L}{a^2}e^{-2at}. \tag{137}$$

This proves the Lemma.

The proof of Claim 4.3.1 is given below.

Given perfect mean flow cancellation, and $\mathbf{f} \equiv 0$ (that is, $\mathbf{F}_M = \mathbf{F}_R$), we have $\mathbf{z}(t) = \mathbf{z}(t_0) = 0$ and the CLPT error is then given by

$$e(t) = \|\,\mathbf{x}(t) - \mathbf{z}(t)\,\| = \|\,\mathbf{x}(t)\,\|, \tag{138}$$

where $\|\cdot\|$ is the standard ℓ^2-norm in $\mathbb{R}^4$. Define ψ as the square of the CLPT error,

$$\psi = e^2 = \|\,\mathbf{x}(t)\,\|^2 = \mathbf{q}^{\mathrm{T}}\begin{bmatrix} I & 0 \\ 0 & 0 \end{bmatrix}\mathbf{q}. \tag{139}$$

It is easy to show that

$$\frac{\mathrm{d}E(\psi)}{\mathrm{d}t} = 2E\left(\mathbf{q}^{\mathrm{T}}\begin{bmatrix} 0 & I \\ 0 & 0 \end{bmatrix}\mathbf{q}\right) = 2E\left(\mathbf{x}^{\mathrm{T}}\nu\right) = 2E\left(\psi_1\right). \tag{140}$$

By Lemma 4.3.3,

$$\frac{\mathrm{d}E\left(\psi(t)\right)}{\mathrm{d}t} = \frac{2L}{a^2} - \frac{4L}{a^2}e^{-at} + \frac{2L}{a^2}e^{-2at}. \tag{141}$$

This equation can be directly integrated (given $\psi(t_0) = 0$) to find:

$$E\left(\psi(t)\right) = \frac{2L}{a^2}t + \frac{4L}{a^3}e^{-at} - \frac{L}{a^3}e^{-2at} - \frac{3L}{a^3}, \tag{142}$$

which is bounded above by $\frac{2L}{a^2}t$ for $t > 1/a = \tau$, the Lagrangian correlation time of the system.

The expected value of $\|\,\mathbf{e}_v(t)\,\| = \|\,\mathbf{x}(t)\,\|$ can be restricted by Jensen's inequality:

$$E\left(\|\,\mathbf{x}(t)\,\|\right) = E\left(\sqrt{\psi(t)}\right) \leq \sqrt{E\left(\psi(t)\right)} < \alpha t^{\frac{1}{2}}, \tag{143}$$

which is satisfied with $\alpha = \sqrt{\frac{2L}{a^2}}$, for t larger than the correlation time scales of the system. Thus, positioning error growth caused by the stochastic eddy diffusivity term is bounded above by a square-root time growth law. This proves Claim 4.3.1.

Remarks: The results of Sections 4.2 and 4.3 can be combined to describe the characteristics of the growth of CLPT error. The initial error growth is dominated by the error contributions caused by the large-scale error flow $\mathbf{f}$, which represents inaccuracies in the model prediction of the mean flow field. This causes an initially exponential CLPT error growth; however, this contribution to the error growth becomes small when the particle reaches an equilibrium of the error flow field. The long-term error contribution is dominated by the eddy diffusivity ν, with CLPT error growth on the order of $t^{1/2}$, as justified by Claim 4.3.1.

4.4 Simulation of CLPT Error Growth

The CLPT error results are first tested in simulation. Two simulations are used: the first, to verify the expected threshold for exponential growth of the CLPT error; the second, to demonstrate motion of controlled agents in the flow defined by (27).

In the first simulation, a square area of interest is selected, centered at the origin, and covered with a grid whose gridsize is normalized to $h = 1$. The error flow $\mathbf{f}$ is simulated by assigning independent, jointly Gaussian-distributed random flow values at each gridpoint. Using these values, all equilibrium points of $\mathbf{f}$ are computed. In the 1-D case, equilibria are kept only if they correspond to a stable equilibrium, i.e., if $\frac{\mathrm{d}f}{\mathrm{d}x} < 0$. In the 2-D case, equilibria are kept if they satisfy the necessary stability criteria, $\frac{\partial f^1}{\partial x} < 0$ and $\frac{\partial f^2}{\partial y} < 0$. Given the set of equilibria z_{eq}, the value

$$|z_*|_1 = \min_{z_{eq}} (|z|_1) \tag{144}$$

is recorded. The above calculation is repeated 10^5 times for each of the 1-D and 2-D cases, and the sample mean taken over all runs. This gives a sample mean of the ℓ^1-norm to the nearest equilibrium which satisfies necessary stability conditions in the 1-D and 2-D cases.

In the 1-D case, the sample mean of the distance to the equilibrium is 1.5, which agrees with the theoretical value of $1.5h$ calculated in Section 4.1. In the 2-dim case, the sample mean of the minimum 1-norm of the equilibrium is $1.92h$. This is less than $2.52h$, the value of the lower bound on the 1-norm of the error computed in Section 4.2, which agrees with Theorem 4.2.1.

The second simulation demonstrates how the results for position estimation error growth are affected by small-scale turbulent flow, modeled by the ν term in the Langevin equation (2). In this simulation, a 2-D region of interest is set up, centered at the origin, and cover it with a uniform rectangular grid. The gridsize used is 2.219 km in the x-direction and 1.826 km in the y-direction, which corresponds to the gridsize used by the ROMS ocean model in the physical glider deployment in Monterey Bay (see Section 6.4.1). The values of the error flow $\mathbf{f}$ at gridpoints are normally distributed random variables with diagonal covariance matrix (given by $\sigma_\xi \mathbf{I}_{2\times 2}$). Flow values at the particle position are obtained using bilinear interpolation of the gridpoint values, with added stochastic drift ν. An Euler-Maruyama integrator is used to find particle positions over time. The simulation is run with 400 repetitions, for different values of the variance of σ (the variance of driving noise in ν), $1/\tau$, and σ_ξ. Figure 5 shows the average ℓ^2-norm of the particle position over time for different values of the simulation parameters. The error growth is initially dominated by the error caused by the error flow $\mathbf{f}$; for longer times, the error is dominated by the small-scale stochastic terms. The shape of the error growth curve depends on the relative strengths of these two contributions, as shown in Figure 5.

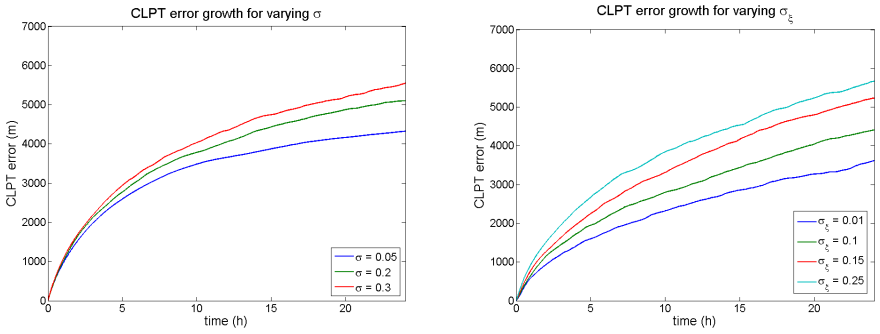

Figure 5: (Left) CLPT error growth over time for different values of variance σ of the stochastic input to ν. The Lagrangian correlation time is $\tau = 0.28$ hrs., and variance of $\mathbf{f}$ at the gridpoints is $\sigma_\xi = 0.3$ m/s. (Right) CLPT error growth over time: the variance σ_ξ of $\mathbf{f}$ at the gridpoints is varied. The variance of the stochastic input to ν is $\sigma = 0.32$. The Langevin correlation time is 0.28 hrs.

CHAPTER 5

ERROR GROWTH UNDER THE TRANSECT-FOLLOWING AND STATION-KEEPING CONTROLLERS

The transect-following and station-keeping controllers differ from the flow-canceling controller in that vehicle speed is assumed to be constant; thus, the "hovering" behavior of the flow-canceling controller is not achievable. The error in predicted vehicle position, then, depends on the interaction between the vehicle motion and the structure of the underlying flow field as well as on the error in the predicted flow values.

5.1 Transect-Following Controller

First we analyze the error growth dynamics under the transect-following controller. Equation (20) for the net motion of the vehicle under transect-following control is reproduced below for convenience:

$$\mathbf{V}(\zeta,t) = \begin{cases} \left(\mathbf{F}_M^T\mathbf{T} + \sqrt{s^2 - (\mathbf{F}_M^T\mathbf{N} + K(\zeta-\mathbf{p})^T\mathbf{N})^2}\right)\mathbf{T} - K(\zeta-\mathbf{p})^T\mathbf{N} & \text{if } \gamma \geq 0 \\ \left(\mathbf{F}_M^T\mathbf{T}\right)\mathbf{T} + \left(\mathbf{F}_M^T\mathbf{N} - \text{sign}\left(\mathbf{F}_M^T\mathbf{N} + K(\zeta-\mathbf{p})^T\mathbf{N}\right)s\right)\mathbf{N} & \text{otherwise,} \end{cases}$$

where

$$\gamma(\zeta) = s^2 - (\mathbf{F}_M^T\mathbf{N} + K(\zeta-\mathbf{p})^T\mathbf{N})^2. \tag{145}$$

We assume that the real and virtual vehicles are initialized on the transect line ℓ, with $\mathbf{x}(t_0) = \mathbf{z}(t_0) \in \ell$. Furthermore, for the remainder of this section, unless stated otherwise, we make the following assumption:

(C1) For any ζ in the state-space $\mathcal{D} \subset \mathbb{R}^2$,

$$s^2 - (\mathbf{F}_M(\zeta,t)^T\mathbf{N})^2 > 0.$$

Under Assumption (C1), the virtual vehicle is always able to cancel the flow normal to the transect line, so that given a simulation over time interval $[t_0, t_1]$, $\mathbf{z}(t_0) \in \ell$ means

$\mathbf{z}(t) \in \ell$ for all $t \in [t_0, t_1]$. Note that this assumption may not always hold in the field; however in general, vehicles are deployed in regions where the ambient flow does not exceed vehicle throughwater speed, so that the flow component normal to the transect can always be canceled.

We are especially interested in cross-track component of the error in the predicted vehicle position $e_{\mathbf{N}} = \mathbf{N}^T\mathbf{e}$, which corresponds to the off-track distance of the real vehicle. We show that the cross-track error $e_{\mathbf{N}} \triangleq \mathbf{N}^T\mathbf{e}$ is bounded in the following proposition.

Proposition 5.1.1 *Consider a vehicle using transect-following control along transect ℓ, as described in (20). The real and virtual vehicles are initialized at $\mathbf{x}(t_0) = \mathbf{z}(t_0) \in \ell$. Suppose the flow field $\mathbf{F}_M$ satisfies Assumption (C1), and the flow speed is bounded as $\|\mathbf{F}_M(\zeta, t)\| \leq F_{\max}$ for all $(\zeta, t) \in \mathcal{D} \times \mathbb{R}$; that the error in modeled flow values is bounded as $\sup_{\mathcal{D}} \|\mathbf{f}\| = f_{\max}$ where $f_{\max}$ satisfies $f_{\max} < s - F_{\max}$; and that the stochastic eddy velocity $\nu(t) = 0$ everywhere. The cross-track component of the error in predicted position of the vehicle is bounded as*

$$|e_{\mathbf{N}}| \leq \frac{f_{\max}}{K}. \tag{146}$$

Proof: The growth of error in predicted position of the vehicle for $\nu(t) \equiv 0$ is given by (10a):

$$\frac{\mathrm{d}\mathbf{e}}{\mathrm{d}t} = \mathbf{V}(\mathbf{z} + \mathbf{e}, t) - \mathbf{V}(\mathbf{z}, t) + \mathbf{f}(\mathbf{z} + \mathbf{e}, t). \tag{147}$$

Let $\mathbf{T}$ denote the unit vector in the direction of the transect and let $\mathbf{N}$ be the unit vector normal to the transect in $\mathcal{D}$. For notational convenience, we denote the along-track speed of the modeled vehicle at position $\zeta \in \mathcal{D}$ by

$$\beta(\zeta, t) = \mathbf{F}_M(\zeta, t)^T\mathbf{T} + \sqrt{s^2 - \mathrm{sat}_s^2(\mathbf{F}_M(\zeta, t)^T\mathbf{N} + K(\zeta - \mathbf{p})^T\mathbf{N})}, \tag{148}$$

where $\mathbf{p}$ is an arbitrary point on ℓ. Let γ be defined as in (145). Note that, under Assumption (C1), $\mathbf{z}(t_0) \in \ell$ means that $\mathbf{z}(t) \in \ell$ for all $t \in [t_0, t_1]$; this means that $(\mathbf{z} - \mathbf{p})^T\mathbf{N} = 0$. Also under Assumption (C1), $\mathrm{sign}\left(\mathbf{F}_M^T\mathbf{N} + K(\zeta - \mathbf{p})^T\mathbf{N}\right) = \mathrm{sign}\left((\zeta - \mathbf{p})^T\mathbf{N}\right)$. Using this together

with (20) and (148), equation (147) can be written as

$$\frac{\mathrm{d}\mathbf{e}}{\mathrm{d}t} = \begin{cases} \left(\beta(\mathbf{z}+\mathbf{e},t)\mathbf{T} - K\left(\mathbf{e}^T\mathbf{N}\right)\mathbf{N}\right) - \beta(\mathbf{z},t)\mathbf{T} + \mathbf{f}(\mathbf{z}+\mathbf{e},t) & \text{if } \gamma(\mathbf{z}+\mathbf{e}) \geq 0 \\ \beta(\mathbf{z}+\mathbf{e},t))\mathbf{T} + \left(\mathbf{F}_M(\mathbf{z}+\mathbf{e},t)^T\mathbf{N} - \mathrm{sign}(e_\mathbf{N})s\right)\mathbf{N} - \beta(\mathbf{z},t)\mathbf{T} + \mathbf{f}(\mathbf{z}+\mathbf{e},t) & \text{otherwise,} \end{cases} \tag{149}$$

$$= \begin{cases} (\beta(\mathbf{z}+\mathbf{e},t) - \beta(\mathbf{z},t))\mathbf{T} - K(\mathbf{e}^T\mathbf{N})\mathbf{N} + \mathbf{f}(\mathbf{z}+\mathbf{e},t) & \text{if } \gamma(\mathbf{z}+\mathbf{e}) \geq 0 \\ (\beta(\mathbf{z}+\mathbf{e},t) - \beta(\mathbf{z},t))\mathbf{T} + \left(\mathbf{F}_M(\mathbf{z}+\mathbf{e},t)^T\mathbf{N} - \mathrm{sign}(e_\mathbf{N})s\right)\mathbf{N} + \mathbf{f}(\mathbf{z}+\mathbf{e},t) & \text{otherwise.} \end{cases} \tag{150}$$

The cross-track error growth is given by

$$\frac{\mathrm{d}e_\mathbf{N}}{\mathrm{d}t} = \frac{\mathrm{d}}{\mathrm{d}t}\mathbf{e}^T\mathbf{N} = \left(\frac{\mathrm{d}\mathbf{e}}{\mathrm{d}t}\right)^T\mathbf{N}, \tag{151}$$

since $\mathbf{N}$ is a constant vector. Using (150) in the above equation, we get:

$$\frac{\mathrm{d}e_\mathbf{N}}{\mathrm{d}t} = \begin{cases} -Ke_\mathbf{N} + f_\mathbf{N}(\mathbf{z}+\mathbf{e},t) & \text{if } \gamma(\mathbf{z}+\mathbf{e}) \geq 0 \\ \left(\mathbf{F}_M(\mathbf{z}+\mathbf{e},t)^T\mathbf{N} - \mathrm{sign}(e_\mathbf{N})s\right) + f_\mathbf{N}(\mathbf{z}+\mathbf{e},t) & \text{otherwise,} \end{cases} \tag{152}$$

where $f_\mathbf{N} \triangleq \mathbf{f}^T\mathbf{N}$ denotes the cross-track component of $\mathbf{f}$. We define a quadratic comparison function

$$W(e_\mathbf{N}) = \frac{1}{2}e_\mathbf{N}^2. \tag{153}$$

Then

$$\frac{\mathrm{d}W(e_\mathbf{N})}{\mathrm{d}t} = \begin{cases} -Ke_\mathbf{N}^2 + f_\mathbf{N}(\mathbf{z}+\mathbf{e},t)e_\mathbf{N} & \text{if } \gamma(\mathbf{z}+\mathbf{e}) \geq 0 \\ (\mathbf{F}_M(\mathbf{z}+\mathbf{e},t)^T\mathbf{N} - \mathrm{sign}(e_\mathbf{N})s)e_\mathbf{N} + f_\mathbf{N}(\mathbf{z}+\mathbf{e},t)e_\mathbf{N} & \text{otherwise.} \end{cases} \tag{154}$$

Consider fist the case where $\gamma(\mathbf{z}+\mathbf{e}) \geq 0$, that is,

$$s^2 - (\mathbf{F}_M^T\mathbf{N} + Ke_\mathbf{N})^2 \geq 0, \tag{155}$$

or

$$s \geq |\mathbf{F}_M^T\mathbf{N} + Ke_\mathbf{N}| \geq F_{\max} + K|e_\mathbf{N}|, \tag{156}$$

which is true if

$$|e_{\mathbf{N}}| \leq \frac{s - F_{\max}}{K}. \tag{157}$$

By assumption, $K > 0$ and $|f_{\mathbf{N}}| \leq \|\mathbf{f}\| \leq f_{\max}$. Thus, from (154) we have

$$\frac{\mathrm{d}W(e_{\mathbf{N}})}{\mathrm{d}t} \leq -Ke_{\mathbf{N}}^2 + f_{\max}e_{\mathbf{N}} < 0 \tag{158}$$

whenever $|e_{\mathbf{N}}| > \frac{f_{\max}}{K}$ and $|e_{\mathbf{N}}| \leq (s - F_{\max})/K$.

Next, consider $\gamma(\mathbf{z} + \mathbf{e}) < 0$. Then

$$\frac{\mathrm{d}W(e_{\mathbf{N}})}{\mathrm{d}t} = (\mathbf{F}_M(\mathbf{z} + \mathbf{e}, t)^T\mathbf{N} - \mathrm{sign}(e_{\mathbf{N}})s)e_{\mathbf{N}} + f_{\mathbf{N}}(\mathbf{z} + \mathbf{e}, t)e_{\mathbf{N}}. \tag{159}$$

From Assumption (C1), it follows that

$$(\mathbf{F}_M(\mathbf{z} + \mathbf{e}, t)^T\mathbf{N} - \mathrm{sign}(e_{\mathbf{N}})s) \begin{cases} < 0 & \text{if } e_{\mathbf{N}} > 0 \\ > 0 & \text{if } e_{\mathbf{N}} < 0. \end{cases} \tag{160}$$

Thus, $(\mathbf{F}_M(\mathbf{z} + \mathbf{e}, t)^T\mathbf{N} - \mathrm{sign}(e_{\mathbf{N}})s)e_{\mathbf{N}} < 0$ for all $e_{\mathbf{N}} \neq 0$. From this, we have that

$$(\mathbf{F}_M(\mathbf{z} + \mathbf{e}, t)^T\mathbf{N} - \mathrm{sign}(e_{\mathbf{N}})s)e_{\mathbf{N}} + f_{\mathbf{N}}(\mathbf{z} + \mathbf{e}, t)e_{\mathbf{N}} < 0 \tag{161}$$

whenever

$$|f_{\mathbf{N}}(\mathbf{z} + \mathbf{e}, t)| < |\mathbf{F}_M(\mathbf{z} + \mathbf{e}, t)^T\mathbf{N} - \mathrm{sign}(e_{\mathbf{N}})s|, \tag{162}$$

which is satisfied if

$$f_{\max} < s - F_{\max}. \tag{163}$$

From the above analysis, we have that $\mathrm{d}W(e_{\mathbf{N}})/\mathrm{d}t < 0$ whenever $|e_{\mathbf{N}}| > \frac{f_{\max}}{K}$ if (163) is satisfied. It follows that the set set $M = \left\{e_{\mathbf{N}} : |e_{\mathbf{N}}| > \frac{f_{\max}}{K}\right\}$ is an invariant set of (152) if (163) is satisfied. Since $e_{\mathbf{N}}(t_0) = 0 \in M$, $e_{\mathbf{N}}(t) \in M$ for all $t \in [t_0, t_1]$. This proves the Proposition.

The growth of error in the along-track direction is more difficult to model, since there is no feedback in the along-track direction. The along-track error growth is given by

$$\frac{\mathrm{d}e_{\mathbf{T}}}{\mathrm{d}t} = [\beta(\mathbf{z} + \mathbf{e}, t) - \beta(\mathbf{z}, t)]\mathbf{T} + f_{\mathbf{T}}(\mathbf{z} + \mathbf{e}, t). \tag{164}$$

We consider $f_{\mathbf{T}}$ a perturbation of the error growth equation. Consider the unperturbed along-track error growth:

$$\frac{\mathrm{d}e_{\mathbf{T}}}{\mathrm{d}t} = [\beta(\mathbf{z}+\mathbf{e},t) - \beta(\mathbf{z},t)]\mathbf{T}. \tag{165}$$

Linearizing about the unperturbed equation about the modeled vehicle position $\mathbf{z}$ gives:

$$\frac{\mathrm{d}e_{\mathbf{T}}}{\mathrm{d}t} \approx \left[\mathbf{T}^T D_{\mathbf{z}}\mathbf{F}_M(\mathbf{z},t) - \frac{\mathbf{N}^T(\mathbf{F}_M(\mathbf{z},t) + K(\mathbf{z}-\mathbf{p}))}{\sqrt{s^2 - (\mathbf{N}^T\mathbf{F}_M(\mathbf{z},t) + K\mathbf{N}^T(\mathbf{z}-\mathbf{p}))^2}}\mathbf{N}^T(D_{\mathbf{z}}\mathbf{F}_M(\mathbf{z},t) + KI)\right]\mathbf{e}, \tag{166}$$

where I denotes the 2×2 identity matrix. This equation depends strongly on the structure of the ambient flow and the cross-track component of the error in predicted vehicle position. For the remainder of this section, we only consider the cross-track error component for the transect-following controller.

The growth of error in predicted vehicle position can be modeled under different flow conditions and for different models of the error in flow forecast values. As in the flow-canceling controller, we consider a case of stochastic error in the modeled flow velocity, with error values at ocean model gridpoints given by random variables. The growth of error in predicted vehicles position in this case is described in the following subsection.

5.1.1 Random Flow Error at Ocean Model Gridpoints

An ocean model outputs flow data $\mathbf{F}_M$ on a limited-resolution grid $G = \{\mathbf{x}_{m,n} : m,n = 0, \pm1, \ldots, \pm\infty\}$. The true ocean flow at each gridpoint is given by $\mathbf{F}_R(\mathbf{x}_{m,n},t) = \mathbf{F}_M(\mathbf{x}_{m,n},t) + \mathbf{f}(\mathbf{x}_{m,n},t)$. As in Chapter 4, we model the errors in modeled flow values at the ocean model gridpoints $\mathbf{x}_{m,n}$ as independent, identically distributed random variables $\mathbf{f}(\mathbf{x}_{m,n}) = \xi_{m,n} = [\xi^1_{m,n}, \xi^2_{m,n}]^T \in \mathbb{R}^2$. In this section we derive bounds on the growth of cross-track error of a transect-following vehicle in an ocean flow field, with guidance from an ocean model with stochastic errors at the model gridpoints.

As shown in the proof of Proposition 5.1.1, the cross-track component of position prediction error under the transect-following controller has dynamics:

$$\begin{cases} \frac{\mathrm{d}e_{\mathbf{N}}}{\mathrm{d}t} &= -Ke_{\mathbf{N}}(t) + f_{\mathbf{N}}(\mathbf{z}+\mathbf{e},t) \\ \frac{\mathrm{d}\mathbf{z}}{\mathrm{d}t} &= V(\mathbf{z},t), \end{cases} \tag{167}$$

where $e_{\mathbf{N}}(t_0) = 0$ and $f_{\mathbf{N}}(\mathbf{z}+\mathbf{e},t) \triangleq \mathbf{N}^T\mathbf{f}(\mathbf{z}+\mathbf{e},t)$ is the error in modeled flow in the cross-track direction. Note that $f_{\mathbf{N}}(\mathbf{z}+\mathbf{e},t)$ can be expressed explicitly as a function of modeled vehicle position $\mathbf{z}$, along-track error $e_{p,\mathbf{T}} = \mathbf{T}^T\mathbf{e}$, cross-track error $e_{\mathbf{N}} = \mathbf{N}^T\mathbf{e}$, and time t. We therefore write it as $f_{\mathbf{N}}(\mathbf{z}+\mathbf{e},t) = f_{\mathbf{N}}(e_{\mathbf{N}},t;\mathbf{z},e_{p,\mathbf{T}})$.

We consider a special case of (167), motivated by the following toy problem. Consider a transect-following vehicle moving along a transect ℓ in an ocean domain covered by a rectangular model grid aligned with ℓ, as shown in Figure 6. Suppose that the initial position of the real and simulated vehicles $\mathbf{z}(t_0) = \mathbf{x}(t_0)$ lies on ℓ, and that the ambient flow can be canceled by the vehicle. Then, the real vehicle remains on ℓ for all $t \in [t_0, t_1]$, and cross-track error in predicted vehicle position corresponds to the off-track motion of the real vehicle. We make the following assumptions about the structure of the ocean model grid and the error $f_{\mathbf{N}}$ in the modeled cross-track flow:

(D1) The ocean model grid is rectangular, with gridsize h in the direction normal to the transect line ℓ, with gridpoints at $e_{\mathbf{N}} = kh$ for $k = 0, \pm 1, \ldots, \pm\infty$.

(D2) The values of error in modeled cross-track flow $f_{\mathbf{N}}$ at ocean model gridpoints $\mathbf{x}_{m,n}$ are independent identically distributed random variables denoted by $\xi^{\mathbf{N}}_{m,n}$. The $\xi^{\mathbf{N}}_k$ are assumed to be symmetrically distributed with mean 0, with probability density function (pdf) ρ_ξ. The values of $f_{\mathbf{N}}(e_{\mathbf{N}},t;\mathbf{z},e_{p,\mathbf{T}})$ in the cross-track direction are given by linear interpolation of gridpoint values. In the along-track direction, the values of $f_{\mathbf{N}}(e_{\mathbf{N}},t;\mathbf{z},e_{p,\mathbf{T}})$ are piecewise constant and are given by the values at the most recently crossed vertical line on ocean model gridpoints (see Figure 6).

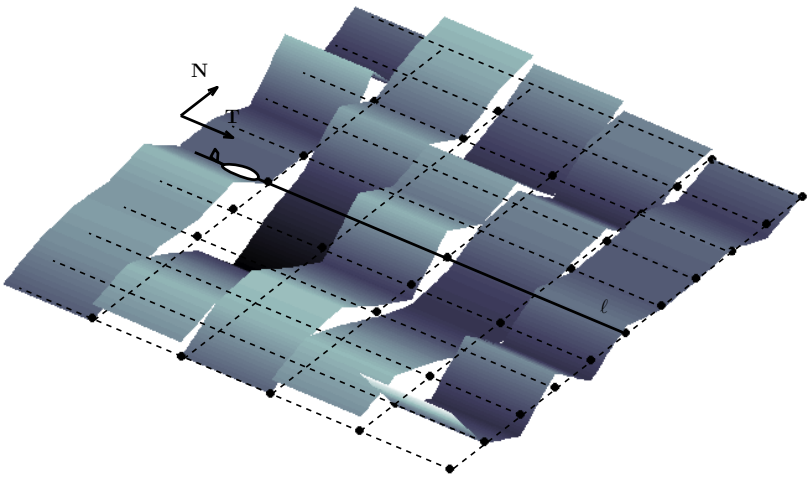

Figure 6: Autonomous underwater vehicle moving along straight-line transect ℓ, with error in the cross-track direction $\mathbf{f_N}$ shown. The error is interpolated linearly in the cross-track direction and is piecewise constant in the along-track direction.

Let $t_1^c < t_2^c < \ldots < t_N^c$, with $t_k^c \in [t_0, t_1]$ for all $k = 1, \ldots, N$, be times when the virtual vehicle crosses the vertical lines of ocean model gridpoints and obtains new values of $\mathbf{f_N}$. In Chapter 4 we showed that, for a vehicle moving under pure flow-canceling control along a straight line, with error dynamics given by $\mathrm{d}e_\mathbf{N}/\mathrm{d}t = f_\mathbf{N}(\mathbf{e_N}, t)$, and time-invariant $f_\mathbf{N}$, the error converges to a stable equilibrium of $f_\mathbf{N}$, with expected distance to the nearest equilibrium given by $3h/2$. Similarly, in the case of the transect-following controller, $e_\mathbf{N}$ approaches a stable equilibrium of (167) on each time interval $(t_n^c, t_{n+1}^c]$. Suppose that each time step $t_{n+1}^c - t_n^c$ is sufficiently long to allow convergence of the error to the nearest stable equilibrium, to within any desired accuracy (the "adiabatic assumption"). We derive expressions for the distribution of the positions of the stable equilibrium to which the error converges as a function of the time step n. We proceed through the following lemmas:

Lemma 5.1.2 *Let $g(e_\mathbf{N})$ denote the net cross-track error velocity in (167), so that*

$$\frac{\mathrm{d}e_\mathbf{N}}{\mathrm{d}t} = g(e_\mathbf{N}) \triangleq -Ke_\mathbf{N}(t) + f_\mathbf{N}(e, t_n^c). \tag{168}$$

Let $e_0^n = e_\mathbf{N}(t_n^c)$ denote $e_\mathbf{N}$ at the start of the n^{th} time interval $(t_n^c, t_{n+1}^c]$ and let $k_0 \triangleq \lfloor e_0^n/h \rfloor$.

Given $g(k_0 h) < 0$, the probability that $g(e_0^n) < 0$ is given by

$$\mathbf{Pr}(g(e_0^n) < 0 | g(k_0 h) < 0) = \frac{\int_{-\infty}^{0} \left[\int_{-\infty}^{\gamma\mu} \rho_\xi(\eta + K(k_0+1)h) \mathrm{d}\eta \right] \rho_\xi(\mu + K k_0 h) \mathrm{d}\mu}{\int_{-\infty}^{0} \rho_\xi(\eta + K k_0 h) \mathrm{d}\eta}. \tag{169}$$

where

$$\gamma = -\frac{(k_0+1)h - e_0^n}{e_0^n - k_0 h}. \tag{170}$$

Proof: Let $\zeta_k \triangleq g(kh)$ denote the cross-track error velocity at the gridpoint indexed by k. By Assumption (D2) ζ_k are random variables with probability distribution functions given by $\rho_{\zeta_k}(x) = \rho_\xi(x + Kkh)$. By affineness of (167) and Assumption (D2), $g(e_{\mathbf{N}})$ is given by a linear interpolation of gridpoint values ζ_k. Thus

$$g(e_0^n) = \frac{1}{h} \left[(e_0^n - k_0 h)\zeta_{k_0+1} + ((k_0+1)h - e_0^n)\zeta_{k_0} \right], \tag{171}$$

and so

$$\mathbf{Pr}(g(e_0^n) < 0 | g(k_0 h) < 0) = \mathbf{Pr}\left((e_0^n - k_0 h)\zeta_{k_0+1} + ((k_0+1)h - e_0^n)\zeta_{k_0} < 0 | \zeta_{k_0} < 0 \right). \tag{172}$$

Rearranging terms in the above equation and using γ defined in (170) gives

$$\begin{aligned} \mathbf{Pr}(g(e_0^n) < 0 | g(k_0 h) < 0) &= \mathbf{Pr}\left(\zeta_{k_0+1} < -\gamma \zeta_{k_0} | \zeta_{k_0} < 0 \right) \\ &= \int_{-\infty}^{0} \left[\int_{-\infty}^{\gamma} \mu \rho_{\zeta_{k_0+1}}(\eta) \mathrm{d}\eta \right] \rho_{\zeta_{k_0}}(\mu | \zeta_{k_0} < 0) \mathrm{d}\mu, \end{aligned} \tag{173}$$

where

$$\rho_{\zeta_{k_0+1}}(\eta) = \rho_\xi(\eta + K(k_0+1)h) \tag{174}$$

and

$$\rho_{\zeta_{k_0}}(\mu | \zeta_{k_0} < 0) = \frac{\rho_\xi(\mu + K k_0 h)}{\int_{-\infty}^{0} \rho_\xi(\eta + K k_0 h) \mathrm{d}\eta} H(-\mu) \tag{175}$$

(here H denotes the unit step function). Plugging (174) and (175) in (173) and simplifying the resulting expression proves the Lemma.

Lemma 5.1.3 *Let $e_0^n = e_{\mathbf{N}}(t_n^c)$ and let $k_0 \triangleq \lfloor e_0^n/h \rfloor$. Then the probability that the stable equilibrium e_{eq} whose basin of attraction contains e_0^n lies in $[kh, (k+1)h)$ is given by:*

$$\mathbf{Pr}(e_{eq} \in [kh, (k+1)h)) =$$
$$\begin{cases} \int_0^\infty \rho_\xi(\eta + Kkh)\mathrm{d}\eta \left[\prod_{j=k+1}^{k_0} \int_{-\infty}^0 \rho_\xi(\eta + Kjh)\,\mathrm{d}\eta\right] R(e_0^n), & k < k_0 \\ \int_{-\infty}^0 \rho_\xi(\eta + K(k+1)h)\mathrm{d}\eta\{ \prod_{j=k_0}^{k} \int_0^\infty \rho_\xi(\eta + Kjh)\mathrm{d}\eta \\ \quad + \left[\prod_{j=k_0+1}^{k} \int_0^\infty \rho_\xi(\eta + Kjh)\mathrm{d}\eta\right] \int_{-\infty}^0 \rho_\xi(\eta + Kk_0h)(1 - R(e_0^n))\}, & k \geq k_0 \end{cases} \tag{176}$$

where

$$R(e_0^n) = \mathbf{Pr}(g(e_0^n) < 0 | g(k_0 h) < 0). \tag{177}$$

Proof: On a given time interval n, (167) is a time-invariant, piecewise-affine, one-dimensional flow. Given $e_0^n \in [k_0 h, (k_0+1)h)$, there are three possible cases:

(1) $\zeta_{k_0} < 0$ and $g(e_0^n) < 0$;

(2) $\zeta_{k_0} < 0$ and $g(e_0^n) > 0$.

(3) $\zeta_{k_0} \geq 0$;

For $\zeta_{k_0} \geq 0$, as in Case (3), it immediately follows that $e_{eq} > k_0 h$, since $e(t)$ cannot pass to an equilibrium $e'_{eq} < k_0 h$ as $\frac{\mathrm{d}}{\mathrm{d}t} e|_{e=k_0 h} \geq 0$. For $\zeta_{k_0} < 0$, the location of the stable equilibrium with basin of attraction containing $e(t)$ depends on the initial value of $\frac{\mathrm{d}}{\mathrm{d}t} e$. If $\frac{rd}{rdt} e(t_n^c) = g(e_0^n) < 0$, as in Case (1), then, by linearity of g on $[kh, e_0^n]$, $g(e) < 0$ for all $e \in [kh, e_0^n]$, and it follows that $e_{eq} < k_0 h$. Similarly, if $\frac{\mathrm{d}}{\mathrm{d}t} e(t_n^c) = g(e_0^n) > 0$ as in Case (2), then $e_{eq} > (k_0+1)h$.

Consider $\mathbf{Pr}(e_{eq} \in [kh, (k+1)h))$ for $k < k_0$. This is non-zero only if Case (1) is satisfied, so that:

$$\mathbf{Pr}(e_{eq} \in [kh, (k+1)h) | k < k_0) = \mathbf{Pr}(e_{eq} \in [kh, (k+1)h) | \text{Case (1)}, k < k_0) \mathbf{Pr}(\text{Case (1)}), \tag{178}$$

where, using independence of ζ_j:

$$\begin{aligned}\mathbf{Pr}(e_{eq} \in [kh,(k+1)h)|\text{Case (1)}, k<k_0) &= \mathbf{Pr}(\zeta_k>0)\prod_{j=k+1}^{k_0-1}\mathbf{Pr}(\zeta_j<0)\\ &= \int_0^\infty \rho_\xi(\eta+Kkh)\mathrm{d}\eta\prod_{j=k+1}^{k_0-1}\int_{-\infty}^0\rho_\xi(\eta+Kjh)\mathrm{d}\eta,\end{aligned} \tag{179}$$

while

$$\begin{aligned}\mathbf{Pr}(\text{Case (1)}) &= \mathbf{Pr}(g(e_0^n)<0|\zeta_{k_0}<0)\mathbf{Pr}(\zeta_{k_0}<0)\mathbf{Pr}(\zeta_{k_0}<0,\ g(e_0^n)<0)\\ &= \mathbf{Pr}(g(e_0^n)<0|\zeta_{k_0}<0)\mathbf{Pr}(\zeta_{k_0}<0)\int_{-\infty}^0\rho_\xi(\eta+ak_0h)\mathrm{d}\eta\end{aligned} \tag{180}$$

The first term is given by Lemma 5.1.2, and $\mathbf{Pr}(\zeta_{k_0}<0)=\int_{-\infty}^0\rho_\xi(\eta+ak_0h)\mathrm{d}\eta$. Plugging equations (179)-(180) in (178) gives:

$$\mathbf{Pr}(e_{eq}\in[kh,(k+1)h)|k<k_0) = \int_0^\infty\rho_\xi(\eta+Kkh)\mathrm{d}\eta\left[\prod_{j=k+1}^{k_0}\int_{-\infty}^0\rho_\xi(\eta+Kjh)\mathrm{d}\eta\right]R(e_0^n), \tag{181}$$

where we have used R to denote $\mathbf{Pr}(g(e_0^n)<0|\zeta_{k_0}<0)$.

Similarly, for $k\geq k_0$, we have that

$$\begin{aligned}\mathbf{Pr}(e_{eq}\in[kh,(k+1)h)|k\geq k_0) &= \mathbf{Pr}(e_{eq}\in[kh,(k+1)h)|\text{Case (2)},k\geq k_0)\mathbf{Pr}(\text{Case (2)})+\\ &\quad\mathbf{Pr}(e_{eq}\in[kh,(k+1)h)|\text{Case (3)},k\geq k_0)\mathbf{Pr}(\text{Case (3)}),\end{aligned} \tag{182}$$

where

$$\begin{aligned}&\mathbf{Pr}(e_{eq}\in[kh,(k+1)h)|\text{Case (2)},k\geq k_0)\\ &=\mathbf{Pr}(\zeta_{k_0+1}>0,\ldots,\zeta_k>0,\zeta_{k+1}<0|\zeta_{k_0}<0,g(e_0^n)>0,k\geq k_0)\\ &=\left[\prod_{j=k_0+1}^{k}\int_0^\infty\rho_\xi(\eta+Kjh)\mathrm{d}\eta\right]\int_{-\infty}^0\rho_\xi(\eta+K(k+1)h)\mathrm{d}\eta\end{aligned} \tag{183}$$

and similarly,

$$\begin{aligned}&\mathbf{Pr}(e_{eq}\in[kh,(k+1)h)|\text{Case (3)},k\geq k_0)\\ &=\left[\prod_{j=k_0}^{k}\int_0^\infty\rho_\xi(\eta+Kjh)\mathrm{d}\eta\right]\int_{-\infty}^0\rho_\xi(\eta+K(k+1)h)\mathrm{d}\eta.\end{aligned} \tag{184}$$

Note that

$$\begin{aligned}\mathbf{Pr}(\text{Case (2)}) &= \mathbf{Pr}(\zeta_{k_0} < 0,\ g(e_0^n) > 0)\mathbf{Pr}(g(e_0^n) > 0|\zeta_{k_0} < 0)\mathbf{Pr}(\zeta_{k_0} < 0) \\ &= (1 - \mathbf{Pr}(\zeta_{k_0} < 0,\ g(e_0^n) > 0)\mathbf{Pr}(g(e_0^n) > 0|\zeta_{k_0} < 0)) \int_{-\infty}^{0} \rho_\xi(\eta + ak_0h)\mathrm{d}\eta \\ &= (1 - R(e_0^n))) \int_{-\infty}^{0} \rho_\xi(\eta + ak_0h)\mathrm{d}\eta,\end{aligned} \tag{185}$$

and

$$\begin{aligned}\mathbf{Pr}(\text{Case (3)}) &= \mathbf{Pr}(\zeta_{k_0} \geq 0) \\ &= \int_{0}^{\infty} \rho_\xi(\eta + ak_0h)\mathrm{d}\eta.\end{aligned} \tag{186}$$

Plugging (183)-(186) in (182) gives:

$$\begin{aligned}&\mathbf{Pr}(e_{eq} \in [kh, (k+1)h)|k \geq k_0) \\ &= \int_{-\infty}^{0} \rho_\xi(\eta + K(k+1)h)\mathrm{d}\eta\{\prod_{j=k_0}^{k} \int_{0}^{\infty} \rho_\xi(\eta + Kjh)\mathrm{d}\eta \\ &\quad + \left[\prod_{j=k_0+1}^{k} \int_{0}^{\infty} \rho_\xi(\eta + Kjh)\mathrm{d}\eta\right] \int_{-\infty}^{0} \rho_\xi(\eta + Kk_0h)(1 - R(e_0^n))\}\end{aligned} \tag{187}$$

Combining equations (181) and (187) proves the Lemma.

Lemma 5.1.4 *Given that $e_{eq} \in [kh, (k+1)h)$, let $u = e_{eq} - kh$. The distribution of u on $[0, h)$ is*

$$\rho_u(u; k) = \frac{h \int_0^\infty v\rho_\xi(v + Kkh)\rho_\xi(v(1 - h/u) + K(k+1)h)\mathrm{d}v}{u^2 \int_0^\infty \rho_\xi(\eta + Kkh)\mathrm{d}\eta \int_{-\infty}^0 \rho_\xi(\eta + K(k+1)h)\mathrm{d}\eta}. \tag{188}$$

Proof: Let $\xi_k^n \triangleq \xi_k(t_n^c) + Kkh$. The pdf of ξ_k^n is $\rho_{\xi^n}(\eta) = \rho_\xi(\eta + K\left\lfloor \frac{\eta}{h} \right\rfloor h)$. With this, $\frac{\mathrm{d}}{\mathrm{d}t}e_{\mathbf{N}}$ on $(t_n^c, t_{n+1}^c]$ can be expressed as

$$\frac{\mathrm{d}e_{\mathbf{N}}}{\mathrm{d}t} = f_n'(e_{\mathbf{N}}) \tag{189}$$

where f_n' takes values $f_n'(kh) = \xi_k^n$ at ocean model gridpoints, and values of f_n' within each grid cell are given by linear interpolation of the gridpoint values.

Given that a stable equilibrium of the system (167) occurs on $[kh, (k+1)h)$, we solve for the x-intercept in terms of ξ_k^n and ξ_{k+1}^n as follows:

$$x = kh + \frac{h\xi_k}{\xi_k - \xi_{k+1}}; \tag{190}$$

or, in terms of $u = x - kh$, $u = h\xi_k/(\xi_k - \xi_{k+1})$.

We show in Chapter 4 that the distribution of u on $[0, h)$ is given by the marginal distribution:

$$\rho_u(u) = \int_{-\infty}^{\infty} \frac{hv}{u^2} \rho_{\xi^n}(v|v \geq 0) \rho_{\xi^n}(v(1-h/u)|v(1-h/u) < 0) \mathrm{d}v, \tag{191}$$

where H denotes the unit step function, and

$$\rho_{\xi^n}(v|v \geq 0) = \frac{\rho_\xi(v + Kkh)}{\int_0^\infty \rho_\xi(\eta + Kkh)\mathrm{d}\eta} H(v) \tag{192}$$

$$\rho_{\xi^n}(v(1-h/u)|v(1-h/u) < 0) = \frac{\rho_\xi(v(1-h/u) + K(k+1)h)}{\int_0^\infty \rho_\xi(\eta + K(k+1)h)\mathrm{d}\eta} H(v(h/u-1)). \tag{193}$$

Plugging (192) and (193) in (191) and simplifying the resulting expression proves the Lemma.

Given $e(t_n^c) = e_0^n$, the distribution of the stable equilibrium on $(t_n^c, t_{n+1}^c]$ whose basin of attraction contains e_0^n is

$$\rho_{eq}(e|e_{\mathbf{N}}(t_n^c) = e_0^n) = \rho_{eq}(e|e_{eq} \in [kh, (k+1)h)) \mathbf{Pr}(e_{eq} \in [kh, (k+1)h)|e_{\mathbf{N}}(t_n^c) = e_0^n), \tag{194}$$

Where $\rho_{eq}(e|e_{eq} \in [kh, (k+1)h))$ and $\mathbf{Pr}(e_{eq} \in [kh, (k+1)h)|e_{\mathbf{N}}(t_n^c) = e_0^n)$ are given by Lemmas 5.1.2-5.1.4. The pdf for ξ normally distributed and $e_0 = 0$ is shown in Figure 7.

The expected norm $E_{eq}(|e_{eq}|) = \int_{-\infty}^{\infty} |e| \rho_{eq}(e) \mathrm{d}e$ of the stable equilibrium to which $e_{\mathbf{N}}$ converges during time interval $(t_n^c, t_{n+1}^c]$ is a function K and ocean model gridsize h, and can be found from numerical integration of (194). The expected norm of the nearest stable equilibrium as a function of K is shown in Figure 8 for initial position $e_0^n = 0$.

We have derived the distribution of equilibria to which $e_{\mathbf{N}}$ converges in a single time interval $(t_n^c, t_{n+1}^c]$, given the initial position $e_{\mathbf{N}}(t_n^c) = e_0^n$. The behavior of the cross-track error $e_{\mathbf{N}}$, sampled at times t_n^c, can be interpreted as a random walk $e_{\mathbf{N},n+1} = e_{\mathbf{N},n} + \omega_{n+1}$, where the

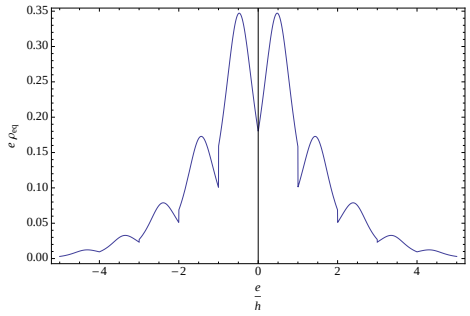

Figure 7: Probability distribution function of nearest equilibrium for the system in (167), given initial position $\mathbf{e}_0 = 0$, for $K = 0.3$, and zero-mean, normally distributed gridpoint flow error values ξ with variance $\sigma = 3$.

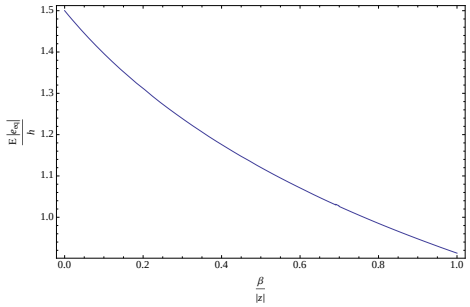

Figure 8: Expected value of $|\mathbf{e}_{eq}|/h$ as a function of the feedback gain K.

distribution of the n+1st step ω_{n+1} is a function of $e_{\mathbf{N},n}$ and control gain K. Simulation results indicate that, given K constant for all n, the distribution of $e_{\mathbf{N},n}$ converges to a stationary distribution as $n \to \infty$. The mean and variance of $e_{\mathbf{N},n}$ over time are plotted in Figure 9.

This model for error growth is only valid so long as the cross-track error is small enough to ensure that the vehicle through-water speed is large enough to cancel cross-track flow and to apply a proportional-gain control to correct the real vehicle's cross-track offset.

5.2 Station-Keeping Controller

We next turn to the case of station-keeping controller. Equation (25) for the net motion of the vehicle under station-keeping control is reproduced below:

$$\mathbf{V}(\zeta, t) = \begin{cases} \left(\mathbf{F}_M(\zeta, t)^T \mathbf{T}(\zeta) + \sqrt{s^2 - (\mathbf{F}_M(\zeta, t)^T \mathbf{N}(\zeta))^2}\right) \mathbf{T}(\zeta) & \text{for } \|\zeta\| \geq R \\ 0, & \text{otherwise,} \end{cases}$$

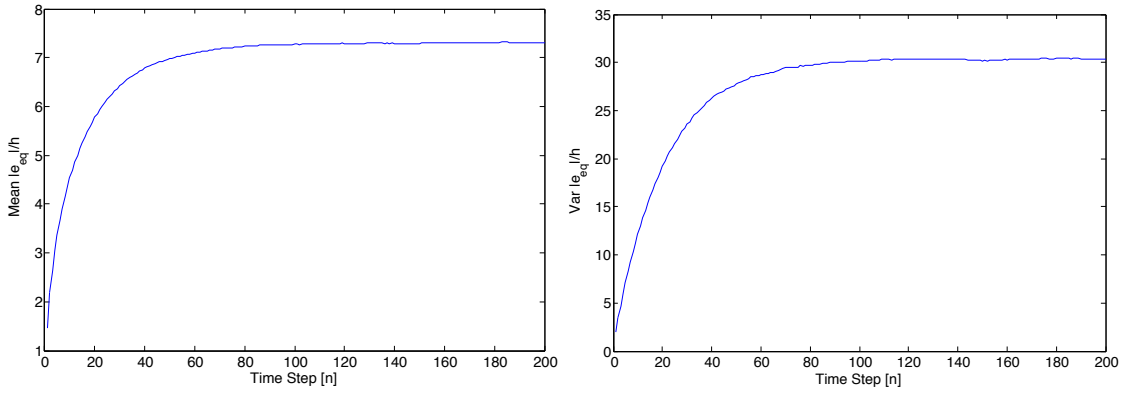

Figure 9: Mean (left) and variance (right) of $|\mathbf{e}_{eq}|$ over time (in units of time steps T).

where $\mathbf{T}(\zeta)$ is a unit vector from ζ to the station-keeping goal, $\mathbf{N}(\zeta)$ is a unit vector normal to $\mathbf{T}$, $R > 0$ is a fixed radius around the goal, and $(\zeta, t) \in \mathcal{D} \times \mathbb{R}$. For convenience, we set the coordinate system so that the station-keeping position is at the origin. Let

$$\beta(\zeta, t) \triangleq \mathbf{F}_M(\zeta, t)^T \mathbf{T}(\zeta) + \sqrt{s^2 - (\mathbf{F}_M(\zeta, t)^T \mathbf{N}(\zeta))^2}, \tag{195}$$

denote the modeled vehicle speed in the direction toward the station-keeping goal.

For the remainder of this section, we make the following assumption:

(C2) For any ζ in the state-space $\mathcal{D} \subset \mathbb{R}^2$,

$$s^2 - \mathbf{F}_M(\zeta, t)^2 > 0.$$

That is, the virtual vehicle is always able to cancel the flow normal to the desired direction of travel. Under Assumption (C2), given a simulation over time interval $[t_0, t_1]$, the virtual vehicle travels in a straight line toward the goal.

We confine our analysis to the case where the vehicle is far from its desired station-keeping position. We find a bound on the error in predicted vehicle position, using the following two Lemmas, which are taken from [72] and are reproduced here without proof:

Lemma 5.2.1 *Let* $\mathbf{V} : \mathcal{D} \times [t_0, t_1] \to \mathbb{R}^m$ *be continuous for some domain* $\mathcal{D} \subset \mathbb{R}^n$*, and suppose that* $[\partial \mathbf{V}/\partial \zeta]$ *exists and is continuous on* $\mathcal{D} \times [t_0, t_1]$*. If, for a convex subset* $\mathcal{W} \subset \mathcal{D}$*,*

there exists a constant $L \geq 0$ such that

$$\left\| \frac{\mathrm{d}\mathbf{V}}{\mathrm{d}\zeta}(\zeta, t) \right\| \leq L \tag{196}$$

on $\mathcal{W} \times [t_0, t_1]$, then $\mathbf{V}(\zeta, t)$ is Lipschitz continuous on $\mathcal{W}$, with Lipschitz constant L.

Lemma 5.2.2 *Let $V(\zeta, t)$ be piecewise continuous in t and Lipschitz continuous (with Lipschitz constant L) in ζ, for all $(\zeta, t) \in \mathcal{D} \times [t_0, t_1]$. Let $\mathbf{z}(t)$ and $\mathbf{x}(t)$ be solutions of*

$$\frac{\mathrm{d}\mathbf{z}}{\mathrm{d}t} = V(\mathbf{z}, t) \tag{197}$$

and

$$\frac{\mathrm{d}\mathbf{x}}{\mathrm{d}t} = V(\mathbf{x}, t) + \mathbf{f}(\mathbf{x}, t), \tag{198}$$

respectively, where $\mathbf{x}(t)$, $\mathbf{z}(t) \in \mathcal{D}$ for all $t \in [t_0, t_1]$. Suppose that

$$\| \mathbf{f}(\zeta, t) \| \leq f_{\max} \qquad \forall (\zeta, t) \in \mathcal{D} \times [t_0, t_1]. \tag{199}$$

Then

$$\| \mathbf{x}(t) - \mathbf{z}(t) \| \leq \| \mathbf{x}(t_0) - \mathbf{z}(t_0) \| \, e^{L(t-t_0)} + \frac{f_{\max}}{L} \left[e^{L(t-t_0)} - 1 \right] \tag{200}$$

for all $t \in [t_0, t_1]$.

Using Lemma 5.2.1 and 5.2.2, the error in predicted vehicle position can be bounded as in the following proposition.

Proposition 5.2.3 *Let $\mathbf{F}_M(\zeta, t)$ be a differentiable, Lipschitz continuous flow field with Lipschitz constant L_F, and suppose that $\| \mathbf{F}_M(\zeta, t) \| \leq F_{\max}$ for all $(\zeta, t) \in \mathcal{D} \times [t_0, t_1]$. Let $\mathbf{x}(t_0) = \mathbf{z}(t_0) = \mathbf{z}_0$ lie far from the goal, so that $\mathbf{z}(t) > R$ for all $t \in [t_0, t_1]$. Under the station-keeping controller, the error in the predicted position of the vehicle is bounded as*

$$\| \mathbf{e}(t) \| \leq \frac{f_{\max}}{L_V} \left[e^{L_V (t-t_0)} - 1 \right], \tag{201}$$

where

$$L_V = L_F \left(1 + \frac{F_{\max}^2}{\sqrt{s^2 - F_{\max}^2}} \right) + \frac{s(F_{\max} + s)}{R \sqrt{s^2 - F_{\max}^2}}. \tag{202}$$

Proof: For notational convenience, we define the following scalar function:

$$\alpha(\mathbf{z},t) = \frac{\mathbf{F}_M(\mathbf{z},t)^T J\mathbf{T}}{\sqrt{s^2 - (\mathbf{F}_M(\mathbf{z},t)^T J\mathbf{T})^2}} \tag{203}$$

and the matrix functions:

$$A(\mathbf{z},t) = (\mathbf{T}\mathbf{F}_M(\mathbf{z},t)^T + \alpha(\mathbf{z},t)\mathbf{T}\mathbf{F}_M(\mathbf{z},t)^T J + \beta(\mathbf{z},t)I)\mathbf{N}\mathbf{N}^T \tag{204a}$$

$$B(\mathbf{z},t) = (\mathbf{T}\mathbf{T}^T + \alpha(\mathbf{z},t)\mathbf{T}\mathbf{F}_M(\mathbf{z},t)^T J). \tag{204b}$$

To apply Lemma 5.2.2, we first show that $\mathbf{V}(\mathbf{z},t)$ is Lipschitz continuous for all $\mathbf{z}$ in $\mathcal{D}' = \{\mathbf{z} \in \mathcal{D} : \| \mathbf{z} \| \geq R\}$. We do this by using Lemma 5.2.1. Using (25) for $\mathbf{V}$ gives

$$\begin{aligned} D_{\mathbf{z}}\mathbf{V}(\mathbf{z},t) = &\left[\mathbf{T}(\mathbf{z})\mathbf{T}(\mathbf{z})^T - \frac{\mathbf{F}_M^T J\mathbf{T}(\mathbf{z})}{\sqrt{s^2 - (\mathbf{F}_M^T J\mathbf{T}(\mathbf{z}))^2}}\mathbf{T}(\mathbf{z})\mathbf{F}_M^T J\right] D_{\mathbf{z}}\mathbf{F}_M(\mathbf{z},t) \\ &+ \left[\mathbf{T}(\mathbf{z})\mathbf{F}_M^T - \frac{\mathbf{F}_M^T J\mathbf{T}(\mathbf{z})}{\sqrt{s^2 - (\mathbf{F}_M^T J\mathbf{T}(\mathbf{z}))^2}}\mathbf{T}(\mathbf{z})\mathbf{F}_M^T J + \left(\mathbf{F}_M^T\mathbf{T}(\mathbf{z}) + \sqrt{s^2 - (\mathbf{F}_M^T J\mathbf{T}(\mathbf{z}))^2}\right) I\right] D\mathbf{T}(\mathbf{z}). \end{aligned} \tag{205}$$

Under Assumption (C2), the virtual vehicle travels in a straight line to the origin with speed $\beta(\mathbf{z},t)$ given by (195). Note that $\mathbf{T}(\mathbf{z}) = \frac{\mathbf{z}(t)}{\| \mathbf{z}(t) \|}$ and $\mathbf{N}(\mathbf{z}) = J\mathbf{T}(\mathbf{z})$ are constant along simulated vehicle trajectories. We therefore drop the argument $\mathbf{z}$ for notational convenience. Substituting (203) and (195) in (205) and using the fact that

$$D_{\mathbf{z}}\mathbf{T}(\mathbf{z}) = -D_{\mathbf{z}}\frac{\mathbf{z}}{\| \mathbf{z} \|} = -\frac{\mathbf{N}(\mathbf{z})\mathbf{N}(\mathbf{z})^T}{\| \mathbf{z} \|}, \tag{206}$$

we have:

$$\begin{aligned} D_{\mathbf{z}}\mathbf{V}(\mathbf{z},t) &= (\mathbf{T}\mathbf{T}^T + \alpha\mathbf{T}\mathbf{F}_M^T J)D_{\mathbf{z}}\mathbf{F}_M(\mathbf{z},t) - \frac{(\mathbf{T}\mathbf{F}_M^T + \alpha\mathbf{T}\mathbf{F}_M^T J - \beta I)\mathbf{N}\mathbf{N}^T}{\| \mathbf{z}(t) \|} \\ &= B(\mathbf{z},t)D_{\mathbf{z}}\mathbf{F}(\mathbf{z},t) - \frac{1}{\| \mathbf{z}(t) \|}A(\mathbf{z},t), \end{aligned} \tag{207}$$

where A and B are defined as in (204). Since, by assumption, $\mathbf{F}_M \in C^1$, (207) is defined and continuous for all $\mathbf{z} \in \mathcal{D}'$; it remains to show that it is bounded. We have:

$$\begin{aligned} \| D_{\mathbf{z}}\mathbf{V}(\mathbf{z},t) \| &= \left\| B(\mathbf{z},t)D_{\mathbf{z}}\mathbf{F}(\mathbf{z},t) - \frac{1}{\| \mathbf{z}(t) \|}A(\mathbf{z},t) \right\| \\ &\leq \| B(\mathbf{z},t) \| \| D_{\mathbf{z}}\mathbf{F}(\mathbf{z},t) \| + \frac{1}{\| \mathbf{z} \|} \| A(\mathbf{z},t) \|, \end{aligned} \tag{208}$$

where $\| M \|$ for $M \in \mathbb{R}^{n \times n}$ is the induced 2-norm defined as

$$\max_{\| \zeta \| = 1} \| M\zeta \| = \sqrt{\lambda_{\max} M^T M}; \tag{209}$$

here $\lambda_{\max}(\cdot) : \mathbb{R}^{n \times n} \rightarrow R$ is the maximum eigenvalue. Then, using the fact that $\mathbf{F}_M$ is Lipschitz continuous with Lipschitz constant L_F, we have

$$\begin{aligned} \| D_{\mathbf{z}} \mathbf{V}(\mathbf{z}, t) \| &\leq \sqrt{\lambda_{\max}(B^T B)} \| D_{\mathbf{z}} \mathbf{F}(\mathbf{z}, t) \| + \frac{1}{\| \mathbf{z} \|} \sqrt{\lambda_{\max}(A^T A)} \\ &\leq \sqrt{\lambda_{\max}(B^T B)} L_F + \frac{1}{\| \mathbf{z} \|} \sqrt{\lambda_{\max}(A^T A)} \end{aligned} \tag{210}$$

It is straightforward to show that

$$\sqrt{\lambda_{\max}(A^T A)} = \frac{s\beta(\mathbf{z}, t)}{\sqrt{s^2 - (\mathbf{F}_M(\mathbf{z}, t)^T J \mathbf{T})^2}} \tag{211}$$

and

$$\sqrt{\lambda_{\max}(B^T B)} = \sqrt{1 - 2\alpha(\mathbf{z}, t) \mathbf{F}_M(\mathbf{z}, t)^T \mathbf{N} + \alpha^2(\mathbf{z}, t) \| \mathbf{F}_M(\mathbf{z}, t) \|^2}. \tag{212}$$

Using (211) and (212), inequality (210) can be written as

$$\begin{aligned} &\| D_{\mathbf{z}} \mathbf{V}(\mathbf{z}, t) \| \\ &\leq L_F \sqrt{1 - 2\alpha(\mathbf{z}, t) \mathbf{F}_M(\mathbf{z}, t)^T \mathbf{N} + \alpha^2(\mathbf{z}, t) \| \mathbf{F}_M(\mathbf{z}, t) \|^2} + \frac{1}{\| \mathbf{z} \|} \frac{s\beta(\mathbf{z}, t)}{\sqrt{s^2 - (\mathbf{F}_M(\mathbf{z}, t)^T J \mathbf{T})^2}}. \end{aligned} \tag{213}$$

Using the fact that

$$-2\alpha(\mathbf{z}, t) \mathbf{F}_M(\mathbf{z}, t)^T \mathbf{N} = 2 \frac{\mathbf{F}^2}{\sqrt{s^2 - (\mathbf{F}_M(\mathbf{z}, t)^T \mathbf{N})^2}} \leq 2 \frac{F_{\max}^2}{\sqrt{s^2 - F_{\max}^2}}, \tag{214}$$

and

$$0 < \beta(\mathbf{z}, t) = \mathbf{F}_M(\mathbf{z}, t) + \sqrt{s^2 - (\mathbf{F}_M(bz, t)^T \mathbf{N})^2} \leq F_{\max} + s \tag{215}$$

we have that $\| D_{\mathbf{z}} \mathbf{V}(\mathbf{z}, t) \|$ is bounded as

$$\begin{aligned} \| D_{\mathbf{z}} \mathbf{V}(\mathbf{z}, t) \| &\leq L_F \sqrt{1 + 2 \frac{F_{\max}^2}{\sqrt{s^2 - F_{\max}^2}} + \frac{F_{\max}^4}{s^2 - F_{\max}^2}} + \frac{s(F_{\max} + s)}{R \sqrt{s^2 - F_{\max}^2}} \\ &= L_F \left(1 + \frac{F_{\max}^2}{\sqrt{s^2 - F_{\max}^2}} \right) + \frac{s(F_{\max} + s)}{R \sqrt{s^2 - F_{\max}^2}} = L_V \end{aligned} \tag{216}$$

on any convex subset $\mathcal{W}$ of $\mathcal{D}'$. Thus, by Lemma 5.2.1, $\mathbf{V}(\mathbf{z}, t)$ is Lipschitz continuous in $\mathbf{z}$ with Lipschitz constant L_V, for all $\mathbf{z} \in \mathcal{D}'$. The Proposition then follows from direct application of Lemma 5.2.2, with $\mathbf{x}(t_0) - \mathbf{z}(t_0) = 0$.

The growth of error can be approximated using a first-order Taylor expansion of the error growth equation, as in (13). For the station-keeping controller, setting $\nu(t) \equiv 0$, we have:

$$\begin{aligned} \frac{\mathrm{d}\mathbf{e}}{\mathrm{d}t} &\approx D_{\mathbf{z}}\mathbf{V}(\mathbf{z}, t; \mathbf{u})\mathbf{e} + \mathbf{f}(\mathbf{z} + \mathbf{e}, t) \\ &\approx \left[B(\mathbf{z}, t) D_{\mathbf{z}}\mathbf{F}(\mathbf{z}, t) - \frac{1}{\| \mathbf{z}(t) \|} A(\mathbf{z}, t) \right] \mathbf{e}(t) + \mathbf{f}(\mathbf{z} + \mathbf{e}, t), \end{aligned} \tag{217}$$

with A and B defined as in (204). In Section 5.2.1, we derive bounds on the first-order error growth in predicted vehicle position for a representative simple case, where the modeled ocean flow $\mathbf{F}_M$ is constant and the difference $\mathbf{f}$ between real and modeled flow is a function of time only.

5.2.1 Simplest Case: Constant Flow with Constant Bias

For constant flow $\mathbf{F}_M$, it is possible to derive an analytic integral equation for the first-order approximation of the error in the predicted vehicle position; this case is a simple illustration of the dependence of position prediction error growth on ambient flow conditions. We derive exact results in the case where $\mathbf{f}$ is constant "bias" flow in the ocean model.

In the case that $\mathbf{F}_M$ is constant, $D_{\mathbf{z}}\mathbf{F}_M \equiv 0$; α and β are constant scalars; and A is a constant matrix. The following lemma will be used in computing the growth of position prediction error:

Lemma 5.2.4 *Given A defined by (204),* $A^i = \beta^{i-1} A$.

Proof: Let $M = \mathbf{N}\mathbf{N}^T$. For A defined as in (204), $A^2 = [\mathbf{T}\mathbf{F}_M^T M + \alpha \mathbf{T}\mathbf{F}_M^T J M - \beta M]^2$. Expanding this expression and using the fact that $M\mathbf{T} = 0$ and $M^2 = (\mathbf{N}\mathbf{N}^T)^2 = M$ gives

$$A^2 = \beta(\mathbf{T}\mathbf{F}_M^T + \alpha \mathbf{T}\mathbf{F}_M J - \beta I) M = \beta A. \tag{218}$$

Lemma 5.2.4 follows by applying (218) i times.

The growth of position prediction error in the constant flow case is summarized in the following proposition:

Proposition 5.2.5 *Given a vehicle with dynamics described by (4a), operating under flow-canceling station-keeping control, and constant model flow* $\mathbf{F}_M$ *such that* $\|\mathbf{F}_M\| \leq s$*, the first-order error in predicted position of the controlled particle grows as:*

$$\mathbf{e}(t) = \left(I + \frac{t}{\|\mathbf{z}_0\|}A\right)\mathbf{e}(t_0) + \left(I + \frac{t}{\|\mathbf{z}_0\|}A\right)\int_0^t \left(I - \frac{\eta}{\|\mathbf{z}_0\| - \beta\eta}A\right)\mathbf{f}(\mathbf{z}+\mathbf{e}, t)\mathrm{d}\eta \tag{219}$$

for $t \in [0, \|\mathbf{z}_0\|/\beta)$*, where* $A \in \mathbb{R}^2$ *is a constant matrix and* β *is a non-negative constant.*

Proof: Since $\mathbf{F}_M$ is constant, $D_{\mathbf{z}}\mathbf{F}_M \equiv 0$, and α, β, and A are constant,(207) can be written as

$$\frac{\mathrm{d}\mathbf{e}}{\mathrm{d}t} = -\frac{1}{\|\mathbf{z}(t)\|}A\mathbf{e} + \mathbf{f} \tag{220}$$

The time variation is confined to the scalar factor $\frac{1}{\|\mathbf{z}(t)\|}$, so (220) can be solved exactly as:

$$\mathbf{e}(t) = e^{-\int_0^t \frac{1}{\|\mathbf{z}(\tau)\|}A\mathrm{d}\tau}\mathbf{e}(t_0) + e^{-\int_0^t \frac{1}{\|\mathbf{z}(\tau)\|}A\mathrm{d}\tau}\int_0^t e^{\int_0^\eta \frac{1}{\|\mathbf{z}(\tau)\|}A\mathrm{d}\tau}\mathbf{f}\mathrm{d}\eta. \tag{221}$$

Let $\mathbf{z}(t_0) = \mathbf{z}_0$ be the initial position of the simulated vehicle. The vehicle will travel in a straight line toward the origin with speed β, so that $\mathbf{z}(t) = \left(1 - \frac{\beta t}{\|\mathbf{z}_0\|}\right)\mathbf{z}_0$, and $\|\mathbf{z}(t)\| = \|\mathbf{z}_0\| - \beta t$ for $t < \frac{\beta}{\|\mathbf{z}_0\|}$. Then

$$-\int_0^t \frac{1}{\|\mathbf{z}(\tau)\|}A\mathrm{d}\tau = \frac{1}{\beta}\log\left(\frac{\|\mathbf{z}_0\| - \beta t}{\|\mathbf{z}_0\|}\right)A. \tag{222}$$

The exponential of this is given by the series definition:

$$e^{\frac{1}{\beta}\log\left(\frac{\|\mathbf{z}_0\|-\beta t}{\|\mathbf{z}_0\|}\right)A} = \sum_{i=0}^{\infty}\frac{\left(\log\frac{\|\mathbf{z}_0\|-\beta t}{\beta\|\mathbf{z}_0\|}\right)^i A^i}{i!}. \tag{223}$$

Using Lemma 5.2.4 and simplifying the algebraic expression we get:

$$e^{-\int_0^t \frac{1}{\|\mathbf{z}(\tau)\|}A\mathrm{d}\tau} = e^{\frac{1}{\beta}\log\left(\frac{\|\mathbf{z}_0\|-\beta t}{\|\mathbf{z}_0\|}\right)A} = I - \frac{t}{\|\mathbf{z}_0\|}A. \tag{224}$$

Similarly,

$$e^{\int_0^t \frac{1}{\|\mathbf{z}(\tau)\|}A\mathrm{d}\tau} = I + \frac{t}{\|\mathbf{z}_0\| - \beta t}A. \tag{225}$$

Using (224) and (225) in (221) proves the Proposition.

Assuming that the real and simulated vehicles are initialized to the same position, so that $\mathbf{e}(t_0) = 0$, we can consider the growth in position prediction error due to error $\mathbf{f}$ in the ocean model flow prediction. For constant $\mathbf{f}$, corresponding to a constant model bias, (219) evaluates to:

$$\mathbf{e}(t) = \left[t\left(I - \frac{1}{\beta}A\right) - \frac{\| \mathbf{z}_0 \| - \beta t}{\beta^2} \log \frac{\| \mathbf{z}_0 \| - \beta t}{\| \mathbf{z}_0 \|} A \right] \mathbf{f}. \tag{226}$$

It is straightforward to show that the error along the direction of travel, $e_{p,\mathbf{T}} = \mathbf{e}(t)^T \mathbf{T}$, is given by $t f_{\mathbf{T}} - 1/\beta(t + \frac{\| \mathbf{z}_0 \| - \beta t}{\beta} \log \frac{\| \mathbf{z}_0 \| - \beta t}{\| \mathbf{z}_0 \|})(F_{M,\mathbf{N}} - \alpha F_{M,\mathbf{T}}) f_{\mathbf{N}}$, where $f_{\mathbf{T}}$ and $f_{\mathbf{N}}$ denote the components of $\mathbf{f}$ along $\mathbf{T}$ and $\mathbf{N}$, respectively, and similarly, $F_{M,\mathbf{T}}$ and $F_{M,\mathbf{N}}$ denote the components of $\mathbf{F}_M$. As there is no feedback control along the vehicle's direction of travel, the error growth in this direction is dominated by the linear term in t. Normal to the direction of travel, the error $e_{\mathbf{N}} = \mathbf{e}(t)^T \mathbf{N}$ is given by $e_{\mathbf{N}} = -\frac{\| \mathbf{z}_0 \| - \beta t}{\beta} \log \frac{\| \mathbf{z}_0 \| - \beta t}{\| \mathbf{z}_0 \|} f_{\mathbf{N}}$. This error initially grows as the vehicle is pushed off-course by the bias flow, and is later reduced as the vehicle steers toward the station-keeping goal, with bound $|e_{\mathbf{N}}| \leq \frac{\| \mathbf{z}_0 \|}{\beta e} f_{\mathbf{N}}$. We next turn to the case of stochastic error in modeled ocean flow.

5.3 Simulation Results

We use simulations, in which both the modeled and true flow field are known, to analyze the performance of the linearized error growth model under different flow conditions. Specifically, we consider three types of simple modeled flow: zero flow, constant flow, and tidal flow with constant amplitude. We note how the relative angle and magnitude of the flow $\mathbf{F}_M$ (and of the perturbation $\mathbf{f}$) affect growth of error in the predicted vehicle position. We then use these simulations as a basis for analyzing the growth of position-prediction error observed during a field deployment.

5.3.1 Simulation Setup

The simulation was based on our field experiments; accordingly, the simulation setup was chosen to reflect, as closely as possible, the setup used in the field. The simulated vehicles

were Slocum gliders (please see Section 6.1 for a more detailed description of the simulated vehicles). Glider navigation is done by generating trajectories which are then converted to waypoint lists and passed to the glider. The glider uses a proprietary on-board waypoint-following algorithm to follow the desired trajectory.

The simulation was run in the Glider Environment Networked Information System (GENIOS), which includes a simulator module *gsim* and planning module *gplan* that generates desired glider trajectories and converts them to waypoint lists for the glider to follow (see Section 6.3 for a more detailed description of GENIOS). The controller is used for trajectory generation as follows: the glider trajectories are simulated under the desired controller and forecast flow field obtained from the ocean model. The same control input is then used to generate simulated glider trajectories under a zero-flow assumption. These are converted to waypoints and passed to the glider. The net motion of the glider following the given trajectories and the ambient flow gives the desired glider motion. Waypoint lists are generated every time a glider surfacing is detected.

Simplified flow models are used in the simulations (flow is either constant (Simulation I) or tidal (Simulation II) with constant tidal amplitude and a single frequency component).

5.3.2 Simulation I

Glider motion is simulated under a constant-flow ocean model. The goal position is fixed at [32.8948 N, 78.0559 W], and the glider's initial position is [33.1272 N, 78.3028 W], 34.6 km from the goal. The glider moves with through-water speed of 32 cm/s, which matches the speed of the transect-following glider in the real experiment. The "virtual" glider moves in a constant flow field $\mathbf{F}_M$; the "real" glider moves in a flow field $\mathbf{F}_R = \mathbf{F}_M + \mathbf{f}$, where $\mathbf{f}$ is a constant bias flow. The simulation time is 16 hours.

We predict the error in glider position using the first-order error-growth model (226) and compare this with the true offset between the "real" and "virtual" glider trajectories. We vary the magnitude and the direction of $\mathbf{F}_M$ and $\mathbf{f}$ relative to the straight-line trajectory from the glider's initial position to the station-keeping goal to test the conditions under which the

linearized error model matches the observed offset between the "real" and "virtual" vehicle. Results are plotted in Fig. 10, which shows the distributions of the following quantities:

$$E_{\mathbf{T}}^{lin} = \frac{\max_{t\in[0,16\text{ hrs}]} \left| e_{\mathbf{T}}^{lin}(t) - e_{\mathbf{T}}^{sim}(t) \right|}{\max_{t\in[0,16\text{ hrs}]} \left\| \mathbf{e}_p^{sim}(t) \right\|},$$

$$E_{\mathbf{N}}^{lin} = \frac{\max_{t\in[0,16\text{ hrs}]} \left| e_{\mathbf{N}}^{lin}(t) - e_{\mathbf{N}}^{sim}(t) \right|}{\max_{t\in[0,16\text{ hrs}]} \left\| \mathbf{e}_p^{sim}(t) \right\|},$$

and

$$E_{\text{norm}}^{lin} = \frac{\max_{t\in[0,16\text{ hrs}]} \left| \left\| \mathbf{e}_p^{lin}(t) \right\| - \left\| \mathbf{e}_p^{sim}(t) \right\| \right|}{\max_{t\in[0,16\text{ hrs}]} \left\| \mathbf{e}_p^{sim}(t) \right\|},$$

for different values of model flow and constant bias magnitude and direction. Here superscript *lin* indicates values obtained from (221) and *sim* indicates values observed in simulation. $E_{\mathbf{T}}^{lin}$ is the discrepancy between the along-track error predicted by the linearized error model (221) and the along-track error observed in simulation, normalized by $\left\| \mathbf{e}_p^{sim}(t) \right\|$. Similarly, $E_{\mathbf{N}}^{lin}$ is the discrepancy between the cross-track error predicted by (221) and the cross-track error observed in simulation, and $E_{\mathbf{N}}^{lin}$ is the discrepancy between the norm of the error predicted by (221) and the norm of the error observed in simulation.

It can be seen from Fig. 10 that while flow magnitude and constant bias magnitude have little effect on the discrepancy between modeled and observed offset of the real and predicted vehicle positions, the modeled and bias flow angles do significantly affect this discrepancy. The lowest mean and variance as a function of modeled flow angle occur for along-track flows in the direction directly opposite to the glider's desired direction of travel. The mean and variance of the discrepancy increases as the flow is rotated closer to the glider heading direction. The effect of the bias flow angle is also quite noticeable, especially as it affects the discrepancy between modeled and observed error values in cross-track direction. The variance of the observed maximum discrepancy in the cross-track direction increases significantly when bias flow is in the cross-track direction.

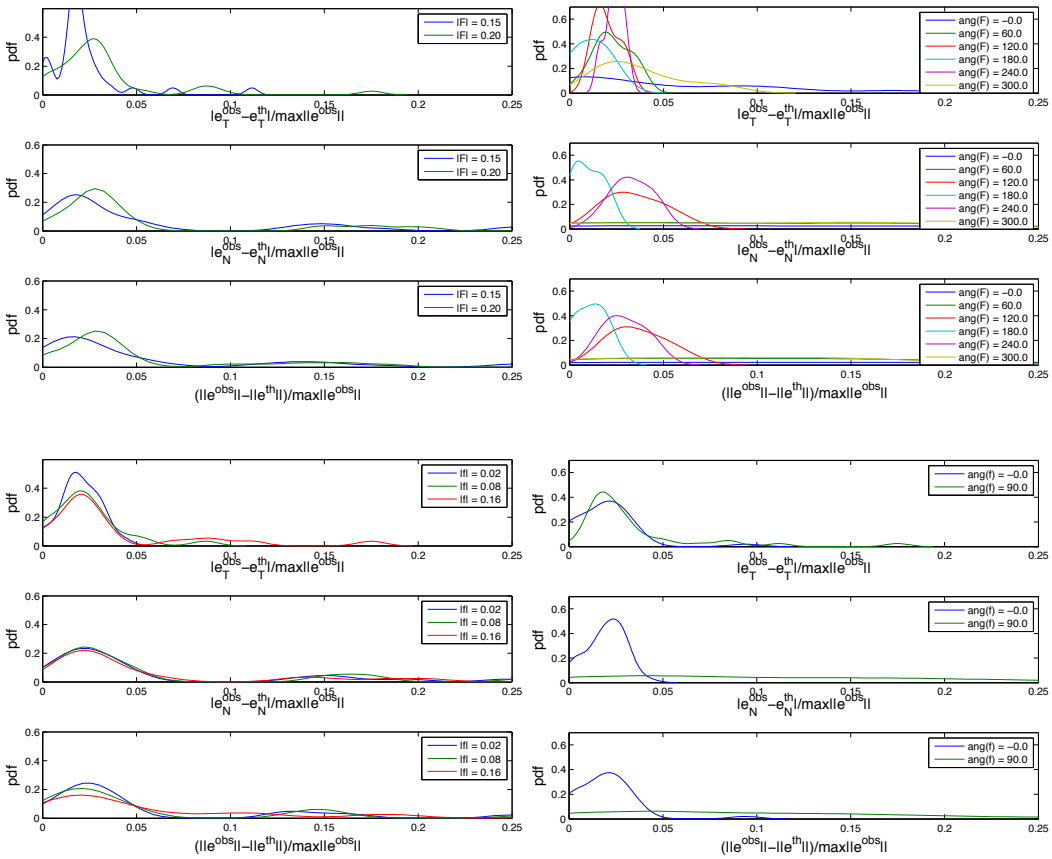

Figure 10: Distribution of $E_{\mathbf{T}}^{lin}$, $E_{\mathbf{N}}^{lin}$, and E_{norm}^{lin}, for different values of modeled flow amplitude (Subfigure 10a) and direction (Subfigure 10b), and for different values of constant bias flow amplitude (Subfigure 10c) and direction (Subfigure 10d).

5.3.3 Simulation II

In the second simulation, we use the same set-up as in Simulation I. This time, however, the flow data F_M is periodic. We use this simulation to verify the performance of the first-order position prediction error model under more realistic flow conditions. The linearized approximation of error is computed by integrating (207) numerically using Euler's method with fixed step size, and, as in Simulation I, is compared with the error (offset between "real" and "virtual" gliders) observed in simulation.

The modeled tidal flow used in this simulation had a single constituent component with period 12.42 hrs., corresponding to M2 (principal lunar), the dominant tidal component in Long Bay. The magnitude and direction of the tidal flow vary over time, so that the tidal

flow vector describes an ellipse with half-length of the major axis F_M and half-length of the minor axis $F_M/2$. We vary F_M, as well as the angle between the major axis of the tidal ellipse and the modeled glider track.

The "real" flow is generated by perturbing the magnitude of the modeled flow, and adding a constant bias flow. We vary the size of the perturbation and the magnitude and direction of the constant bias flow, and compare the along-track and cross-track errors, as well as total error magnitude, obtained from the linearized error model and observed in simulation. The results are shown in Figs. 11-13 (Fig. 11 shows results for bias flow only; Fig. 12 shows results for error in tidal flow magnitude only, and Fig. 13 shows results for error in modeled flow amplitude with added constant flow bias). The magnitudes of error in modeled tidal amplitude, and of constant bias flow, were chosen so as to be comparable with values encountered in the field.

The results of Simulation II demonstrate the limitations of the linearized error model in approximating position-prediction error in a time-varying flow environment. While cross-track error predictions remain, on average, fairly good, the along-track linearized error differs significantly from that observed in simulation. The maximum measured difference between predicted and observed along-track error in the simulation is 1.48 km. In the case of constant bias in the modeled flow field (Fig. 11), the distributions of $E_{\mathbf{T}}^{lin}$, $E_{\mathbf{N}}^{lin}$, and E_{norm}^{lin} vary little with the tidal flow angle and with angle of the added flow bias, but depend strongly on the magnitude of the bias flow, with highest mean and variance corresponding to lower values of the bias flow magnitude. In the case of perturbed tidal amplitude (Fig. 12), the distribution of $E_{\mathbf{T}}^{lin}$ depends strongly on the amplitude of the perturbation, with maximal discrepancy between modeled and observed along-track error occurring for larger error amplitudes. The same factors determine greatest discrepancy between modeled and observed error growth when both bias flow and perturbation of the tidal flow amplitude are present (Fig. 13).

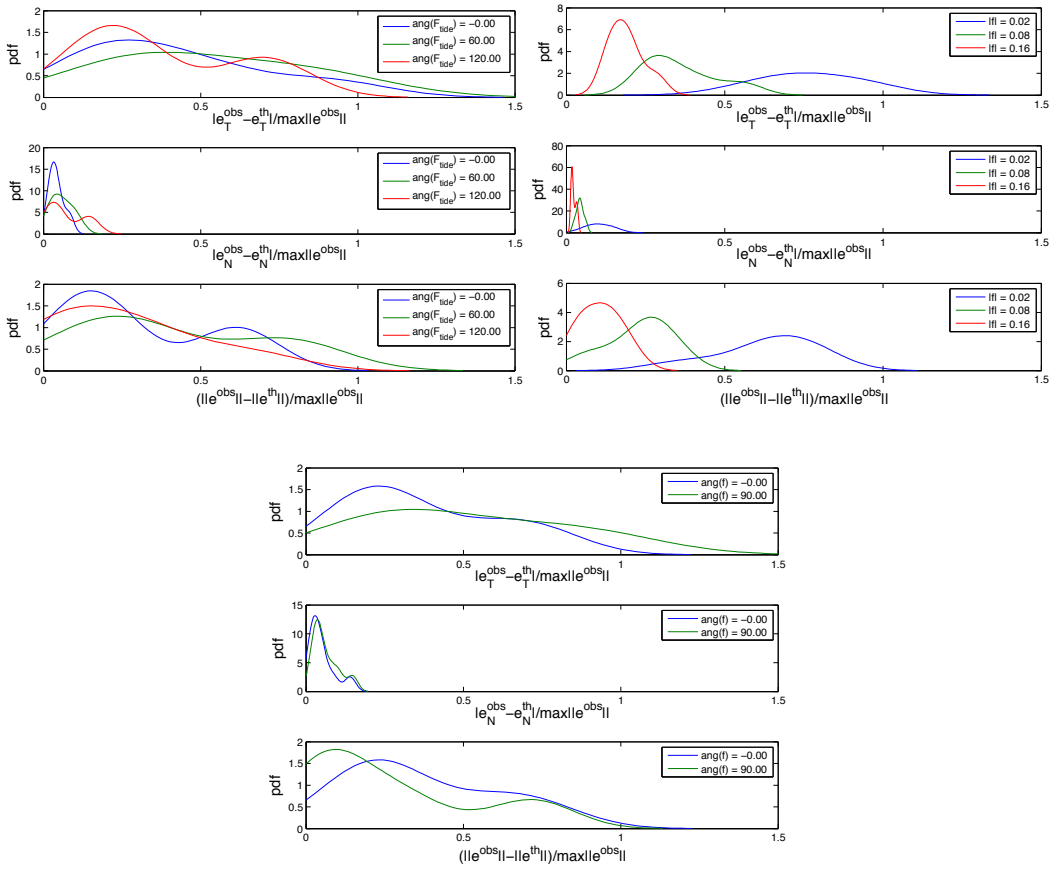

Figure 11: Distribution of $E_{\mathbf{T}}^{lin}$, $E_{\mathbf{N}}^{lin}$, and E_{norm}^{lin}, for different values of angle of modeled tidal ellipse (Subfigure 11a), and for different values of constant bias flow amplitude (Subfigure 11c) and direction (Subfigure 11b). The real tidal flow amplitude is the same as the modeled one (F_M), and is equal to 0.2 m/s.

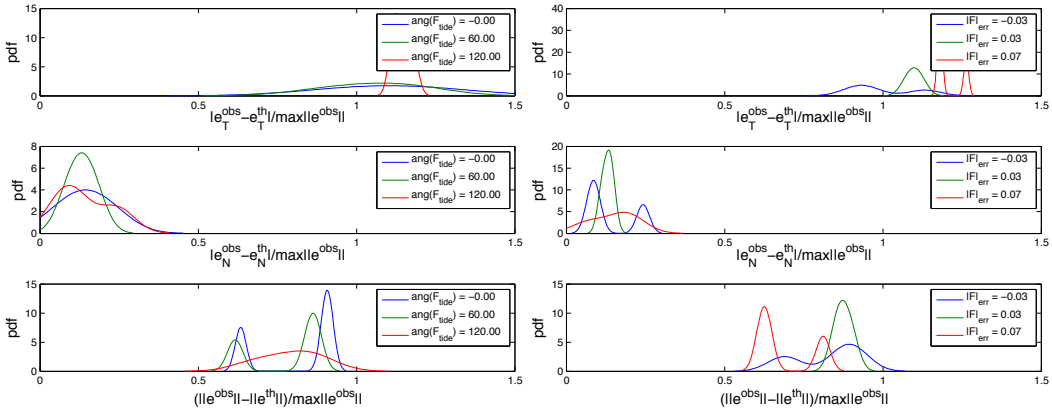

Figure 12: Distribution of $E_{\mathbf{T}}^{lin}$, $E_{\mathbf{N}}^{lin}$, and E_{norm}^{lin}, for different values of angle of modeled tidal ellipse (Subfigure 12a), and for different values of error in the modeled flow amplitude F_M (Subfigure 12b), with no constant bias flow. The real tidal flow amplitude is 0.2 m/s.

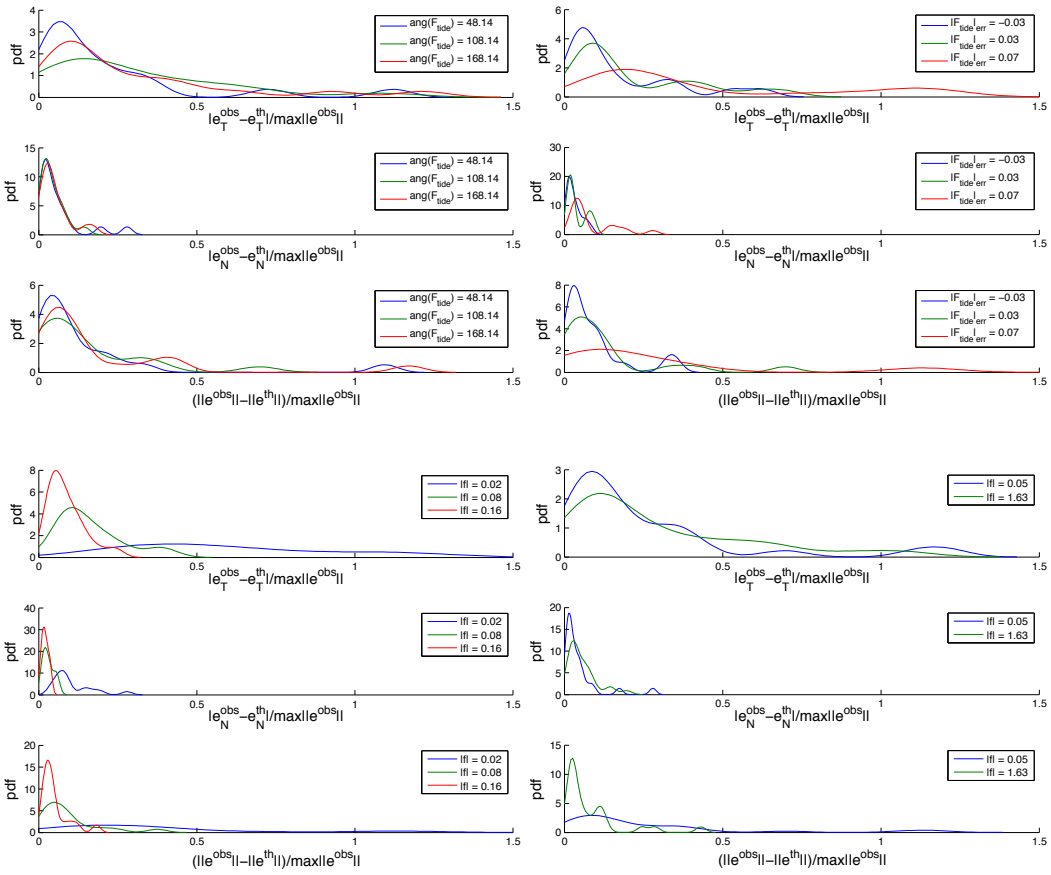

Figure 13: Distribution of $E_{\mathbf{T}}^{lin}$, $E_{\mathbf{N}}^{lin}$, and E_{norm}^{lin}, for different values of angle of modeled tidal ellipse (Subfigure 13a), for different errors in the modeled flow amplitude F_M (Subfigure 13b), and for different values of constant bias flow amplitude (Subfigure 13c) and direction (Subfigure 13d). The real tidal flow amplitude is 0.2 m/s.

CHAPTER 6

GLIDER FIELD DEPLOYMENTS

The theoretical results derived in Chapters 4 and 5 have been verified using data from three field experiments: the ASAP experiment conducted in Monterey Bay, CA, in the summer of 2006; the Long Bay experiment conducted in Long Bay, SC, in the winter of 2012; and a ten-day follow-up study in Long Bay in the winter of 2013. The following section describes the experimental setups used during these deployments.

6.1 Gliders

In both the ASAP and Long Bay experiments, the AUVs used were Slocum battery gliders [65, 56] (see Figure 14). All six gliders deployed in the ASAP experiment had maximal dive depth of 200 m. The two gliders deployed in Long Bay in 2012 had maximal dive depths of 100 m and 200 m, respectively; the follow-up study used a 200 m glider. The horizontal throughwater speed of the gliders depends on the hardware configuration, dive angle, and dive depth; the effective through-water speed of the gliders used in our experiments was approximately 0.3 m/s, though speeds varied from glider to glider and were adjusted accordingly in the glider navigation software.

The gliders have two onboard computers: the science computer, which is used to log all science data, and the flight computer, which is used to run glider missions. Glider operators are not granted direct control over glider sensors or actuators, but are able to set glider operating parameters, and to pass waypoints to the glider. The glider follows the waypoint-specified trajectory using a proprietary onboard waypoint-following algorithm. In both experiments, glider waypoint lists were generated using an onshore controller. The gliders communicated with the onshore controller using an Iridium satellite connection through *dockserver*, a shore-based computer, which collected all glider surfacing data and sent new waypoint lists/commands to the gliders (see Figure 15).

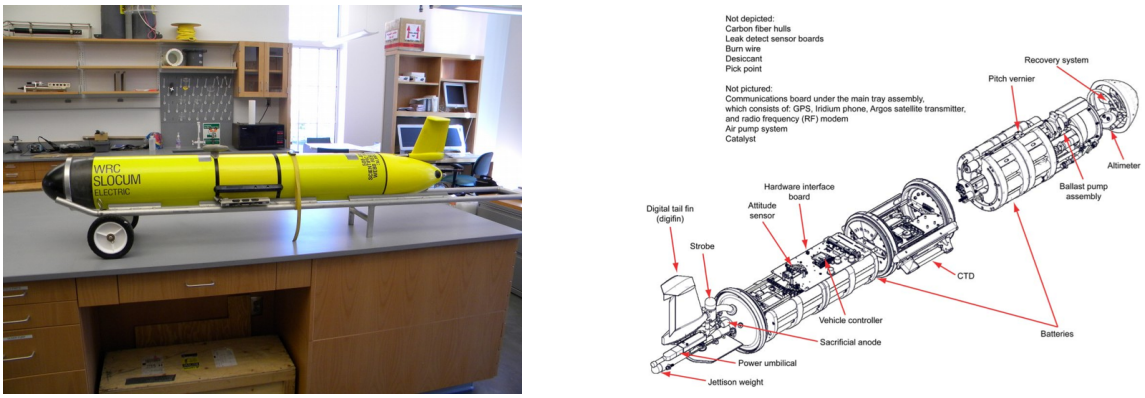

Figure 14: Glider *Ramses* used in the winter 2012 deployment near Long Bay, SC (left). A schematic of the glider hardware is shown on the right. The battery pack can be shifted back and forth to adjust glider pitch angle. The tail fin is used as an active rudder for turning; in addition, the battery pack can be rotated to adjust roll for turning. The glider schematic is taken from "Slocum G2 Glider Operators Manual" [73].

6.1.1 Glider On-Board Flow Estimation

Gliders perform an automatic on-board estimate of the depth-averaged flow velocity over the latest dive period. This estimate was used during our field deployments to add a correction term in the predicted flow speeds obtained from ocean models.

The glider on-board flow estimate is based on the difference between the glider's dead-reckoned estimate of its position at the surfacing time, and the true surfacing position. Consider the k^{th} dive of the mission; we wish to find $\mathbf{F}^k_{\text{glider}}$, the glider estimate of the depth-averaged flow over the k^{th} dive. Let T_{dive} be the glider dive time. During the dive, the glider calculates its vertical speed s_z using measurements of ambient pressure; the vertical speed is converted to an estimate of horizontal speed s by multiplying by the tangent of the angle of attack, α (which is a fixed before deployment in the field). The glider heading is measured directly using an internal compass. The glider's speed and heading are then used to calculate a dead-reckoned position estimate $\hat{\mathbf{x}}(t)$. Let T_{surf} be the surfacing time; $\hat{\mathbf{x}}(T_{\text{surf}})$ is then the dead-reckoned surfacing position. The real glider surfacing position is given by $\mathbf{x}(T_{\text{surf}})$. The depth-averaged flow estimate would be $F^k_{\text{depth.avg'd}} = (\mathbf{x}(T_{\text{surf}} - \hat{\mathbf{x}}(T_{\text{surf}})))/(T_{\text{surf}} - T_{\text{dive}})$; however, the surfacing position cannot be measured directly due to delay in obtaining the first GPS fix. During the time required to establish a GPS position

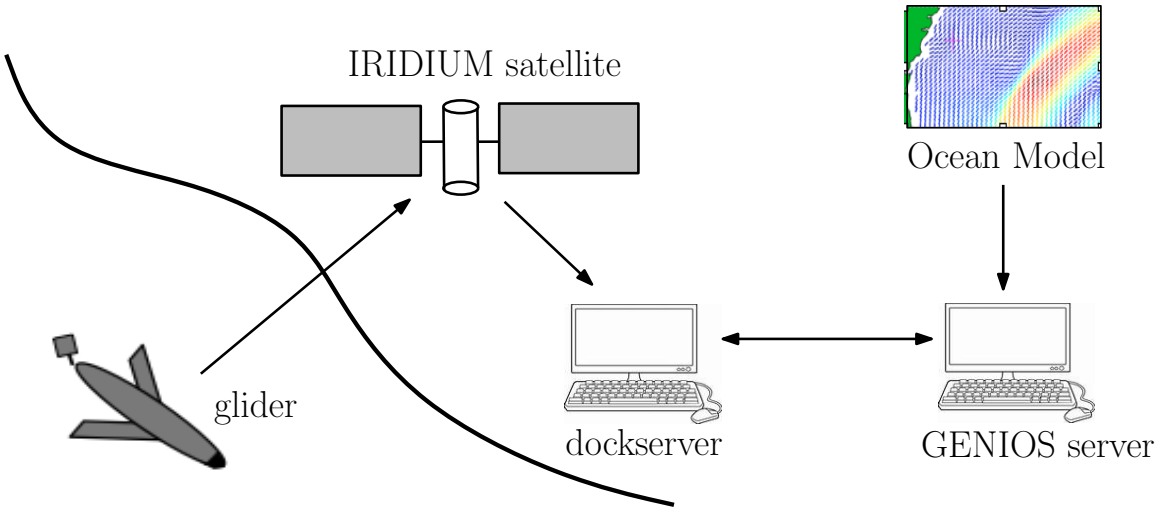

Figure 15: Schematic of glider communication with on-shore controller. The gilder surfaces periodically and receives position information from the global positioning system (GPS). It then transmits its location to a dedicated onshore computer (*dockserver*). The position files on dockserver are polled by the GENIOS server. When a new surfacing is detected, GENIOS generates a new waypoint list for the glider, using forecast flow data from an ocean model, and uploads it to dockserver. The waypoint list is then sent to the glider. All communication between the glider and *dockserver* is done via IRIDIUM satellite linkup.

measurement, the glider is pushed about by surface flows and wind, and drifts from the original surfacing position, so that $\mathbf{x}(T_{\text{GPS}}) \neq \mathbf{x}(T_{\text{surf}})$. To correct for the surface drift, the glider obtains a second GPS fix at time T'_{GPS} (see Figure 16). The drift during over time interval $[T_{\text{GPS}}, T'_{\text{GPS}}]$, $\mathbf{d}'_{\text{surf}} = \mathbf{x}(T'_{\text{GPS}}) - \mathbf{x}(T_{\text{GPS}})$, is used as an estimate of the drift $\mathbf{d}_{\text{surf}}$ over time interval $[T_{\text{surf}}, T_{\text{GPS}}]$ and the time $\Delta T'_{\text{GPS}} = T'_{\text{GPS}} - T_{\text{GPS}}$ is used as an estimate for $\Delta T_{\text{GPS}} = T_{\text{GPS}} - T_{\text{surf}}$. Thus we use the estimate $\mathbf{x}'(T_{\text{surf}}) = \mathbf{x}(T_{\text{GPS}}) - \mathbf{d}'_{\text{surf}}$ for the real surfacing position in the depth-averaged flow velocity calculation (see Figure 17). Then

$$\mathbf{F}^k_{\text{glider}} = (\mathbf{x}'(T_{\text{surf}}) - \hat{\mathbf{x}}(T_{\text{surf}}))/\Delta T'_{\text{GPS}}. \tag{227}$$

It should be noted that Slocum gliders have an option for current correction; using this option enables an on-board flow cancellation algorithm. When operating with current correction, the glider adjusts its heading to cancel the on-board flow estimate based on surfacing data collected for the previous dive. In coastal environments with strong tidal flows

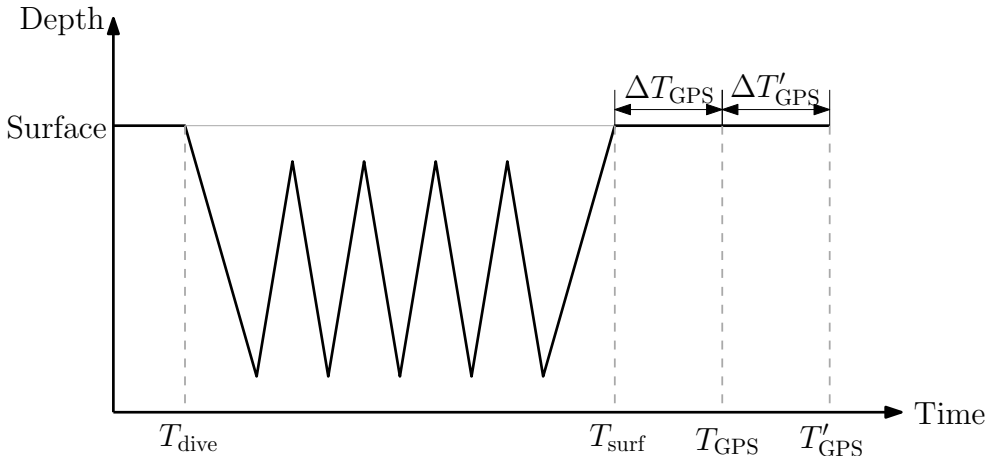

Figure 16: Schematic of glider dive, showing time of last dive (T_{dive}), last surfacing time (T_{surf}), and times T_{GPS} and T'_{GPS} corresponding to the first and second glider GPS fix, respectively.

which change significantly over the glider dive duration, this flow-canceling algorithm generally performs so poorly that it it preferable to have no current corrections. During the ASAP and Long Bay deployments, the on-board current correction was therefore turned off.

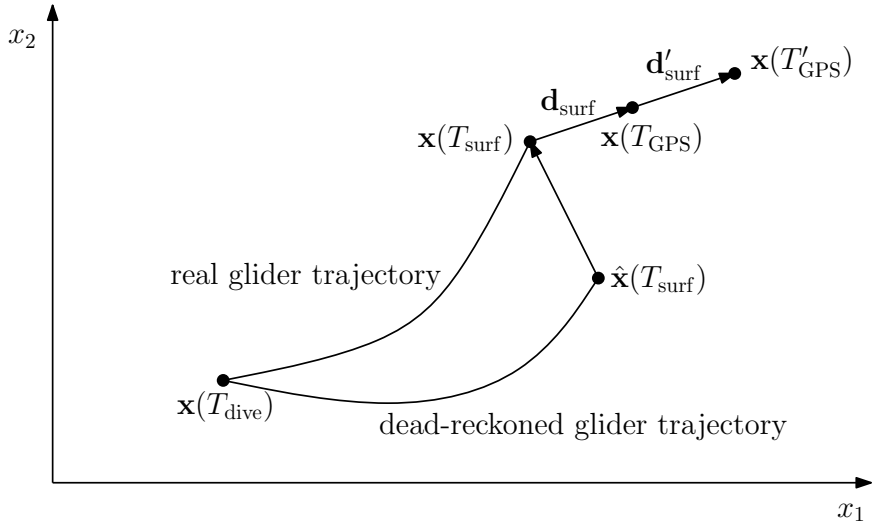

Figure 17: Schematic of the glider's on-board flow estimation algorithm.

6.2 Flow Conditions and Predictive Ocean Models

The ASAP experiment in Monterey Bay, CA, was conducted under relatively light flow conditions. Tidal flows in the region are quite weak. The real vehicles were guided using only on-board flow estimates collected by the entire glider fleet, using a linear estimation technique known as objective analysis (OA) [74], as described in [40]. Glider position predictions were obtained using the following three ocean models: the Navy Coastal Ocean Model (NCOM), the Harvard Ocean Prediction System (HOPS), and the Regional Ocean Modeling System (ROMS) developed by NASA JPL. The NCOM model is a free-surface, primitive-equation model with global global temperature and salinity data assimilation from the Modular Ocean Data Assimilation System (MODAS). The model is discretized on a grid with resolution of approximately 2.24 km over the study site, and provides a 72-hour flow forecast. The HOPS model is a primitive equation model adapted for coastal applications. The ROMS model is a free-surface, terrain-following, primitive equation model with mean gridsize of $1.8 - 2.2$ km over the study domain. The flow values at the glider position for each ocean model were obtained using a linear interpolation of the model flow gridpoint values.

The region around Long Bay is characterized by strong flows; as far as the author is aware, the deployment in Long Bay in 2012 was the first attempt to operate gliders in such difficult flow conditions over an extended period of time. The strong flows are the result of two contributing factors: namely, the tides and the Gulf Stream. According to a 1979 study by Lee *et al.* [75], tidal currents account for approximately 80% of current variability in the cross-shore direction at 50 m water depth, and for approximately 50% at 100 m depth; in the along-shore direction, tidal current variability accounts for approxiamtely 20% of current variability at 50 m water depth, and for approximately 5% at 100 m. Most along-shore variability in flow is due to low-frequency wind-driven or Gulf Stream-induced flows [76], and Gulf Stream flows dominate at depths greater than 100 m.

The flow in the study domain is strongly influenced both by tides and by the Gulf

Stream. The domain is a rectangular region oriented parallel to the shore-line, as shown in Figure 18. The near edge of the domain lies about 82 km off-shore (where water depth is approximately 30 m and tidal flows are dominant). The shelf-break, where the depth begins to increase steeply with off-shore distance, is located approximately 110 km off-shore, at a depth of 75 m. The far edge of the domain lies about 120 km off-shore, at a depth of 176 m, where Gulf Stream influences dominate the flow (see Figure 18).

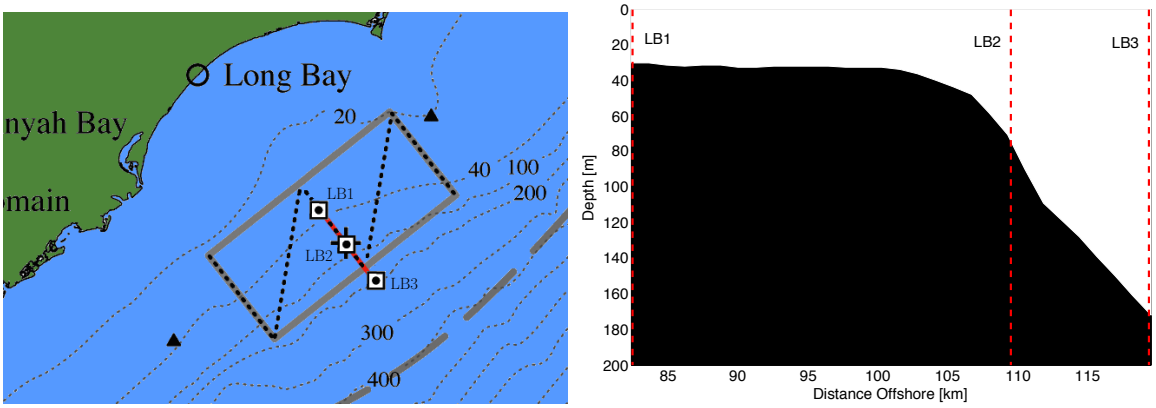

Figure 18: (Left) study domain for Long Bay experiment. (Right) water depth along the cross-shore transect marked by points LB1, LB2, and LB3, showing the gradual depth increase over the continental shelf, and steep drop-off at the shelf break. Tidal influences dominate the flow over the shallow parts of the domain (for depths below approximately 60 m), while Gulf Steam flows dominate in the deep water.

Unfortunately, there is no available high-resolution general circulation model which accurately captures the flow features at the edge of the Gulf Stream. We therefore used an in-house model that combined predictions of tidal flow values with glider on-board flow estimates to obtain a flow forecast.

Tidal flow forecasts were obtained from a database compiled by B. Blanton [76]. The database stores amplitudes and phase angles for 37 tidal constituents at discrete nodes of a finite-element grid over the study domain. The amplitude and phase values are based on a series of simulations run using the Advanced Circulation Ocean Model (ADCIRC), and have been extensively tested and verified [76]. In the Long Bay experiments, we use a subset of the available tidal constituents, as others have negligible influence on the observed

flow velocity; see Table 1 for a list of the tidal constituents used in Long Bay.

Table 1: Tidal constituents used to model tidal flow during the 2012 and 2013 deployments in Long Bay, SC.

Tidal Constituent	Period [hrs]	Description
M2	12.42	Principal lunar semi-diurnal
S2	12.00	Principal solar semi-diurnal
N2	12.66	Larger lunar elliptic semi-diurnal
K1	23.93	Luni-solar diurnal
O1	25.82	Principal lunar diurnal

Additional flow components were computed as follows. It was assumed that the real ocean flow $\mathbf{F}_R(\mathbf{x}, t)$ at the vehicle location $\mathbf{x}(t)$ can be expressed as the superposition of the high-frequency tidal flow $\mathbf{F}_{\text{tidal}}(\mathbf{x}, t)$ modeled in the ADCIRC database, an additional low-frequency flow $\mathbf{F}_{\text{LF}}(\mathbf{x}, t)$ that does not change significantly in space or in time over the duration of a single dive, and some other high-frequency flow components $\mathbf{F}_{\text{HF}}(\mathbf{x}, t)$:

$$\mathbf{F}_R(\mathbf{x}, t) = \mathbf{F}_{\text{LF}}(t) + \mathbf{F}_{\text{tidal}}(\mathbf{x}, t) + \mathbf{F}_{\text{HF}}(\mathbf{x}, t). \tag{228}$$

We consider the low-frequency flows to be those with periods of more than 30 hours along the glider trajectory. The tidal flow is obtained from the ADCRIC database; the low-frequency flow must be estimated based on past glider on-board flow estimates. Let T^k_{dive} be the time of the k^{th} dive, and let T^k_{surf} be the time of the subsequent surfacing. Let $\mathbf{F}^k_{\text{glider}}$ be the glider on-board estimate of the depth-averaged flow over $[T^k_{\text{dive}}, T^k_{\text{surf}}]$, computed as described in Section 6.1.1. Taking the time-average of (228) over $[T^k_{\text{dive}}, T^k_{\text{surf}}]$, we get:

$$\begin{aligned}\mathbf{F}^k_{\text{glider}} &\approx \frac{1}{\Delta T^k}\int_{T^k_{\text{dive}}}^{T^k_{\text{surf}}} \mathbf{F}_R(\mathbf{x}(t), t)\mathrm{d}t \\ &= \frac{1}{\Delta T^k}\int_{T^k_{\text{dive}}}^{T^k_{\text{surf}}} \mathbf{F}_{\text{LF}}(\mathbf{x}(t), t)\mathrm{d}t + \frac{1}{\Delta T^k}\int_{T^k_{\text{dive}}}^{T^k_{\text{surf}}} \mathbf{F}_{\text{tidal}}(\mathbf{x}(t), t)\mathrm{d}t + \frac{1}{\Delta T^k}\int_{T^k_{\text{dive}}}^{T^k_{\text{surf}}} \mathbf{F}_{\text{HF}}(\mathbf{x}(t), t)\mathrm{d}t,\end{aligned} \tag{229}$$

where ΔT^k denotes $T^k_{\text{surf}} - T^k_{\text{dive}}$. Let

$$\bar{\mathbf{F}}^k_{\text{LF}} = \frac{1}{\Delta T^k}\int_{T^k_{\text{dive}}}^{T^k_{\text{surf}}} \mathbf{F}_{\text{LF}}(\mathbf{x}(t), t)\mathrm{d}t \tag{230}$$

denote the time-averaged low-frequency flow over dive k, let

$$\bar{\mathbf{F}}^k_{\text{tidal}} = \frac{1}{\Delta T^k} \int_{T^k_{\text{dive}}}^{T^k_{\text{surf}}} \mathbf{F}_{\text{tidal}}(\mathbf{x}(t), t)\mathrm{d}t \tag{231}$$

denote the time-averaged tidal flow, and let

$$\bar{\mathbf{F}}^k_{\text{HF}} = \frac{1}{\Delta T^k} \int_{T^k_{\text{dive}}}^{T^k_{\text{surf}}} \mathbf{F}_{\text{HF}}(\mathbf{x}(t), t)\mathrm{d}t \tag{232}$$

denote the time-averaged value of other high-frequency flow components. We have that $\bar{\mathbf{F}}^k_{\text{LF}} + \bar{\mathbf{F}}_{\text{HF}} \approx \mathbf{F}^k_{\text{glider}} - \bar{\mathbf{F}}^k_{\text{tidal}}$. However, we $\bar{\mathbf{F}}_{\text{tidal}}$ cannot be computed directly, since the precise underwater position $\mathbf{x}(t)$ of the vehicle is not known on $[T^k_{\text{dive}}, T^k_{\text{surf}}]$. To resolve this problem, we note that tidal flow over the Long Bay domain varies slowly in space (the change in tidal flow amplitude over a 1 km change in position does not exceed 1 cm/s). We therefore query the tidal database at a single location $\mathbf{x}(T^k_{\text{dive}})$ and obtain the estimate

$$\bar{\mathbf{F}}^k_{\text{tidal}} \approx \tilde{\mathbf{F}}^k_{\text{tidal}} = \frac{1}{\Delta T^k} \int_{T^k_{\text{dive}}}^{T^k_{\text{surf}}} \mathbf{F}_{\text{tidal}}(\mathbf{x}(T^k_{\text{dive}}), t)\mathrm{d}t, \tag{233}$$

and use this to estimate the de-tided flow over dive k:

$$\mathbf{F}^k_{\text{detide}} \triangleq \bar{\mathbf{F}}^k_{\text{LF}} + \bar{\mathbf{F}}^k_{\text{HF}} \approx \mathbf{F}^k_{\text{glider}} - \tilde{\mathbf{F}}^k_{\text{tidal}}. \tag{234}$$

To estimate the low-frequency flow, we apply a low-pass filter to the computed flow data. A rectangular window with length of 5 days $W_{5\text{ days}}$ is applied to the data, so that all measurements of $\mathbf{F}_{\text{detide}}$ older than 5 days are set to 0. We use a 4^{th}-order Butterworth filter $BF[\cdot]$ with cutoff frequency $1/30$ hours^{-1} to find the low-frequency flow component:

$$\bar{\mathbf{F}}_{\text{LF}} \approx BF[W_{5\text{ days}}(\mathbf{F}_{\text{detide}})]. \tag{235}$$

Assuming that the low-frequency flow component is approximately constant in time and space over the duration of a single dive, we generate the modeled flow values $\mathbf{F}_M$ at the predicted vehicle position $\mathbf{z}(t)$ over the following dive period $[T^{k+1}_{\text{dive}}, T^{k+1}_{\text{surf}}]$ using the last available value for $\bar{\mathbf{F}}_{\text{LF}}$:

$$\mathbf{F}_M(\mathbf{z}, t) = \bar{\mathbf{F}}^k_{\text{LF}} + \mathbf{F}_{\text{tidal}}(\mathbf{z}, t), \tag{236}$$

where $\mathbf{F}_{\text{tidal}}$ is obtained from the ADCIRC database.

6.2.1 Reconstruction of the Long Bay Flow Field

In order to test the linearized model for growth of error in predicted vehicle position over time given large-scale structure in the modeled flow error (described in Section 5.2), the real ocean flow field $\mathbf{F}_R$ must be known. This flow has to be estimated based on glider on-board measurements of depth-averaged flow, as no other flow data are available at the desired positions over the study domain. To perform the reconstruction, we assume that the flow is spatially invariant, and composed of the three components $\mathbf{F}_{\text{LF}}$, $\mathbf{F}_{\text{tidal}}$, and $\mathbf{F}_{\text{HF}}$, as before. The real flow is approximated as in (236):

$$\mathbf{F}_R(\mathbf{z}, t) \approx \bar{\mathbf{F}}^k_{\text{LF}} + \mathbf{F}_{\text{tidal}}(\mathbf{z}, t), \tag{237}$$

but this time, the time interval is $[T^k_{\text{dive}}, T^k_{\text{surf}}]$. Here $\bar{\mathbf{F}}^k_{\text{LF}}$ and $\mathbf{F}_{\text{tidal}}(\mathbf{z}, t)$ are computed as before.

6.3 GCCS and GENIOS

During the ASAP experiment, the gliders were controlled using the Glider Coordinated Control System (GCCS), a Matlab-based path planning and navigation software, which is described in detail in [40, 41]. In the Long Bay experiment, a significantly modified and expanded version of GCCS, now called Glider-Environment Network Information System (GENIOS), was used. A brief overview of GCCS/GENIOS is given in this section.

The GCCS glider control software was first developed at Princeton University by D. Paley and F. Zhang. GENIOS was developed by D. Chang at Georgia Tech in 2011-2012, using GCCS as a basis. The main part of GCCS is written in Matlab and consists of two modules: a planning module (*gplan*) and a simulator module (*gsim*). GENIOS additionally has an environment handler which directly handles communication between the GCCS and underwater gliders through the dockserver.

The *gplan* module is used to generate glider waypoint lists. *Gplan* can simulate glider motions using either a detailed three-dimensional glider model with flow data from ocean model predictions, or a fast, less accurate two-dimensional particle model. The detailed

glider model is used to predict future glider surfacing positions; the particle model is used to quickly generate glider trajectories, given a glider surfacing position and control algorithm. The glider path is then converted to a list of waypoints which the glider follows to stay on the desired trajectory.

The *gsim* module uses the three-dimensional glider model and flow data from ocean model predictions to simulate the path of each glider. This enables users to test glider control and navigation algorithms under various flow conditions in the lab, prior to deployment in the field. This is a significant advantage, since the cost of glider deployment and recovery can be quite high. During a real glider deployment, the *gsim* module is used to predict future surfacings while a glider is underwater; this is useful for quickly generating desired trajectories for the glider, so that they will be available as soon as the glider comes to the surface. This was done routinely during the ASAP experiment; in Long Bay, on the other hand, trajectories generated from the *gsim*-predicted position were used as "backups"; when the glider surfaced, a trajectory would be computed from its real surfacing location and sent to the glider. If the glider lost communication before the new trajectory had been computed, the "backup" trajectory was used instead.

The *environment handler* in GENIOS was used to detect glider surfacings, as well as to fetch and load ocean model flow data. The glider surfacing positions and times, and ADCIRC flow estimates, were passed to *gplan*. The *environment handler* was also used to upload waypoint lists generated by *gplan* to the gliders. During the ADCIRC experiment, external software was used to handle communications between the glider and GCCS.

The environmental conditions, as well as mission goals, were quite different in the ASAP and the Long Bay experiments. As a result, the GCCS/GENIOS configurations in each experiment differ significantly. The control objective of the ASAP experiment was to coordinate motions of fleet of gliders around closed tracks in a relatively mild flow environment. During the ASAP deployment, therefore, a heavy reliance was placed on *gsim* predictions of glider surfacing positions to achieve coordinated motion between gliders in

spite of asynchronous surfacing time. Flow predictions used by *gplan* were computed by averaging glider on-board flow measurements from previous dives. During the Long Bay experiment, on the other hand, the gliders were not required to coordinate their motions; however, the ambient flow environment was significantly more challenging, because of high tidal flow velocities, and influence from the Gulf Stream. Therefore, desired trajectories were computed at each surfacing based on the latest GPS data available from the glider, and current corrections based on flow obtained from ocean models were incorporated in the trajectory generation in *gplan*. More details about the GCCS/GENIOS configurations used in each experiment are given in the sections describing the individual experiments.

6.4 ASAP 2006

The Adaptive Sampling and Prediction (ASAP) field experiment was conducted in Monterey Bay, CA, in August 2006. The purpose of the experiment was to study the three-dimensional heat and mass transfer dynamics of the coastal upwelling center in the Bay [5, 64]. A 22×40 km control volume was monitored for a period of one month using a heterogeneous ocean sampling network. A fleet of 10 underwater gliders, including 6 Slocum and 4 Spray gliders, was used to take measurements of ocean states.

The gliders moved along predetermined tracks, which were chosen to optimize a user-specified sampling metric (see [70]). The gliders were coordinated through the centralized onshore controller to maintain sufficient inter-agent spacing to ensure good sensor coverage of the region of interest. The control algorithm used is described in detail in [40].

6.4.1 ASAP Field Experiment Results

A virtual glider experiment was run in GCCS *gsim* alongside the physical experiment. The gliders in the virtual fleet were modeled using true glider parameters, and the same proprietary on-board controller as that used by the physical gliders. The virtual gliders were initialized at the same positions as their physical counterparts, and their motions were simulated using flow data from ocean models. The virtual experiment was repeated for

three different models, as described in Section 6.2. Each virtual experiment was run over a period of 24 hours.

A plot of the norm of the error in the position prediction over time (averaged over all gliders and all days for which data is available) obtained using the virtual glider model is shown in Figure 19. Note that the error grows approximately exponentially until a value of about twice the gridsize is reached; past this point, the growth rate slows down. This agrees with the CLPT prediction of expected threshold for exponential growth of the CLPT error, and with the contribution of the stochastic eddy diffusivity term in the Langevin equation.

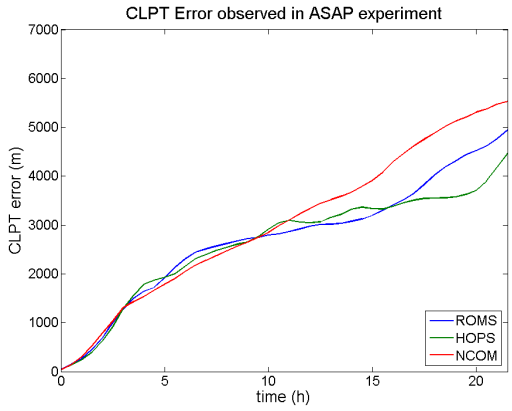

Figure 19: CLPT error for different ocean models observed during ASAP experiment.

6.5 Long Bay 2012

The Long Bay 2012 experiment was conducted off the coast of Long Bay, South Carolina between January 25 and April 4, 2012. The scientific goal of the experiment was to study the physical processes driving the formation of persistent wintertime phytoplankton blooms at the shelf break, in a region where existing ocean models predict low biological productivity. Two Slocum gliders were deployed to monitor the study domain as part of a heterogeneous sampling network. The gliders were assigned to track two predefined trajectories: the first glider, referred to as *Pelagia*, followed a cross-shore transect of length 46.2 km, with endpoints at positions LB1 = [78.3300 W 33.1726 N] and LB3 = [78.0132 W 32.8524 N] (over the course of the deployment, the farshore endpoint was sometimes

shifted inshore as far as LB2 = [78.0945 W 32.9415 N], to avoid strong currents), while the second glider, *Ramses*, performed a station-keeping mission at LB3 (see Figure 20).

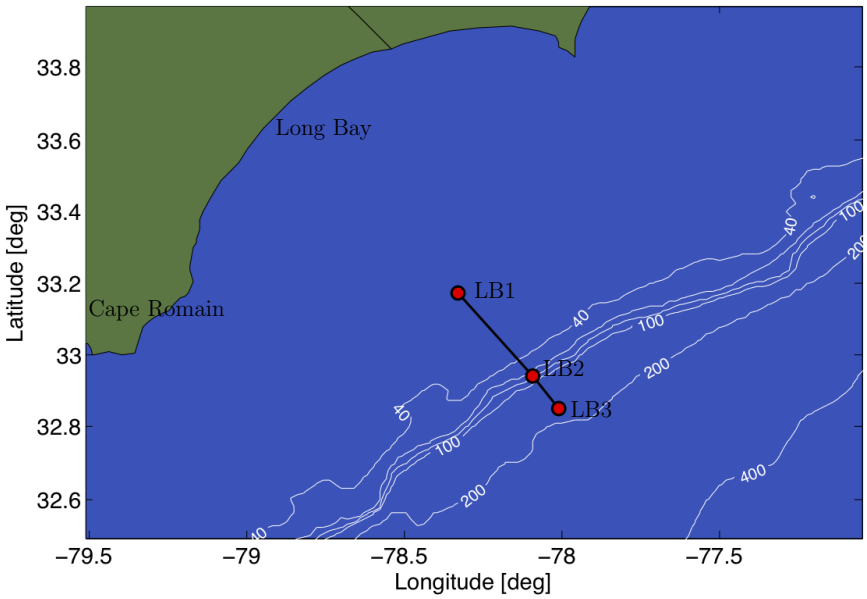

Figure 20: Glider tracks for 2012 deployment in Long Bay, SC. Positions LB1, LB2, and LB3 are marked by red circles. The first glider performed a station keeping mission at LB3, while the second moved on the transect between LB1 and LB3.

Glider navigation was done using GENIOS (see Section 6.3). The desired trajectory for each glider was computed using the station-keeping control law (see Chapter 3.4.3), with modeled flow data computed as described in Section 6.2. To achieve transect-following behavior for the glider *Pelagia*, the station-keeping position was switched between the two transect endpoints.

6.5.1 Long Bay Field Experiment Results

A virtual glider experiment was run alongside the physical experiment, using the simulation module *gsim* on GENIOS. The virtual gliders were initialized at the same positions as their physical counterparts, and their motions were simulated using flow data computed as described as in Section 6.2. The virtual glider experiments were run over periods of 24 hours, described in Table 2.

A plot of the magnitude of the error in the predicted position for each glider over time

Table 2: Simulation start times and positions in Long Bay 2012 deployment.

Start Date and Time (UTC)	Starting Position (Lon, Lat)	Station Keeping Goal
17 Mar, 01:24	78.3544 W 33.1719 N	LB1
18 Mar, 21:23	78.3544 W 33.1719 N	LB2
19 Mar, 13:55	78.3028 W 33.1272 N	LB2
23 Mar, 17:32	78.1546 W 32.9164 N	LB1
25 Mar, 17:52	78.3185 W 33.1586 N	LB2

is shown in Figure 21. Note that for the transect-following glider *Pelagia*, the error grows approximately exponentially until a value of about 1.2 times gridsize is reached; past this point, the growth rate slows down. This agrees with the theoretical threshold for exponential growth of the CLPT error. For the station-keeping glider, the error increases rapidly to about 0.9 km, or roughly $1/4$ of the gridsize, then slows. The CLPT error for both gliders has a periodic variation with period of approximately 6 hours, which is the period corresponding to the M4 tidal component. This periodic variation in CLPT error is consistent with error in modeling of the tidal flows experienced by the gliders. Note also that the transect-following glider had, in reality, a slower-than-modeled effective through-water speed, on account of more frequent inflections as it was swimming in shallower water (with inflections as shallow as 30 m, well below the 100 m dive limit); this accounts for a through-water speed reduction of approximately $15 - 20\%$. This error in modeled velocity in *gplan* may also have led to impaired flow cancellation performance and to tidal variation in the CLPT error for the transect-following glider.

We next compare the output of the linearized model for growth of error in predicted vehicle position (described in Chapter 5.2) with error observed in the field experiment. The error in predicted glider position and the linearized estimate are shown in Figure 23. The theoretical error computation based on linearized error dynamics gives a fairly accurate estimate of the glider cross-track position prediction error, but along-track performance is poor; this is consistent with our observations in the simulations in Section 5.3.3. There are several possible explanations for the discrepancy between modeled and observed errors in

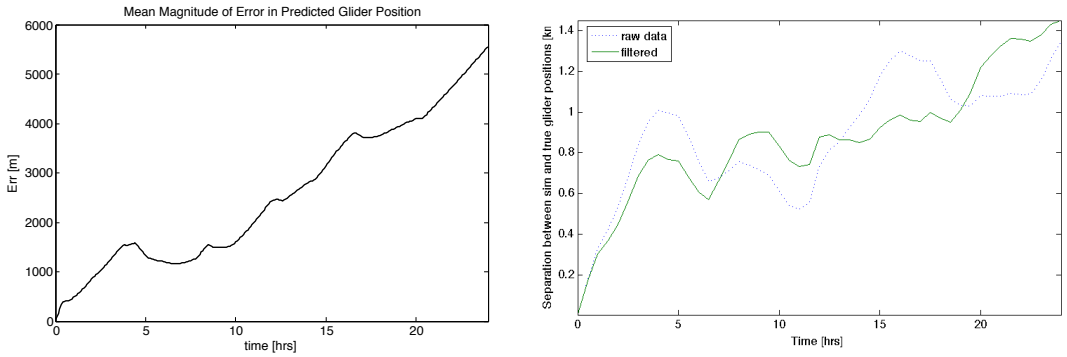

Figure 21: Average CLPT error for transect-following glider (left) station-keeping glider (right).

the predicted vehicle position: first is the fact that the flow model used by the glider was discontinuous, with jumps occurring at glider dive times, while the first-order error growth model assumes continuously varying ocean model flow values. Second, the error in the ocean model flow values is computed based on the reconstruction of ocean flow data as described in Section 6.2.1. This reconstruction technique ignores spatial variation in the real ocean flow and may introduce inaccuracy in the values of $\mathbf{f}$ used in the linearized error growth model.

6.6 Long Bay Follow-Up Deployment 2013

The Long Bay follow-up deployment took place between February 21 and March 1, 2013. A single glider was deployed and performed a transect-following mission, using the station-keeping controller described in Section 3.4.3. The station-keeping position alternated between the transect endpoints, which were located at positions LB+20 = [78.1966 W 33.0367 N] and LB+40 = [78.0559 W 32.8948 N] (see Figure 24).

6.6.1 Follow-Up Field Experiment Results

To analyze position prediction error observed in the field, we run simulations of the virtual glider in the *gsim* module in GENIOS. The real glider position is obtained from GPS measurements of glider surfacing positions. We compare modeled and real glider trajectories over non-overlapping 24-hour prediction periods.

The virtual gliders are simulated in a modeled flow field $\mathbf{F}_M$ computed as in Section 6.2, where depth-averaged flow estimates from the latest real glider surfacing preceding the current simulation time are used to obtain the low-frequency flow components. The magnitude of the error in modeled glider position over three simulations runs (see Table 3), and the magnitude error averaged over the three runs, is shown in Figure 25. The error does not exhibit the characteristic growth observed in the ASAP experiment that was indicative of position prediction error growth caused by stochastic error in the modeled flow predictions; instead, the growth in position prediction error magnitude is approximately linear in time. This is consistent with large-scale, slowly-varying errors in the forecast flow values.

Table 3: Simulation start times and positions in Long Bay 2013 deployment.

Start Date and Time (UTC)	Starting Position (Lon, Lat)	Station Keeping Goal
22 Feb, 21:05	78.2108 W 33.0675 N	LB+40
24 Feb, 04:41	78.0562 W 32.9088 N	LB+20
25 Feb, 12:43	78.1774 W 33.0098 N	LB+40

The real flow experienced by the glider was reconstructed from glider on-board flow measurements as described in Section 6.2.1. The error $\mathbf{f}$ in modeled flow values is obtained by taking the difference of the reconstructed flow and the estimated flow values used during the experiment. Computed values of $\mathbf{f}$ along glider trajectories for the three 24-hour periods described in Table 3 are plotted in Fig. 26.

We next compare the output of the linearized model for growth of error in predicted vehicle position (described in Chapter 5.2) with results obtained in the field. Figure 27 shows the error in predicted glider position, together with the linearized error estimate, decomposed into along-track and cross-track components. The theoretical error computation based on linearized error dynamics gives a fairly accurate estimate of the glider cross-track position prediction error, but along-track performance is poor. This is consistent with our observations in the simulations described in Section 5.3.3. We also note that the flow model

used by the glider was discontinuous, with jumps occurring at glider dive times; this creates inaccuracies in the linearized error model, which assumes continuously varying ocean model flow values. Additionally, the since error in ocean model flow values is computed based on the reconstruction of ocean flow data, there may be some inaccuracy in the values of $\mathbf{f}$ used in the linearized error growth model.

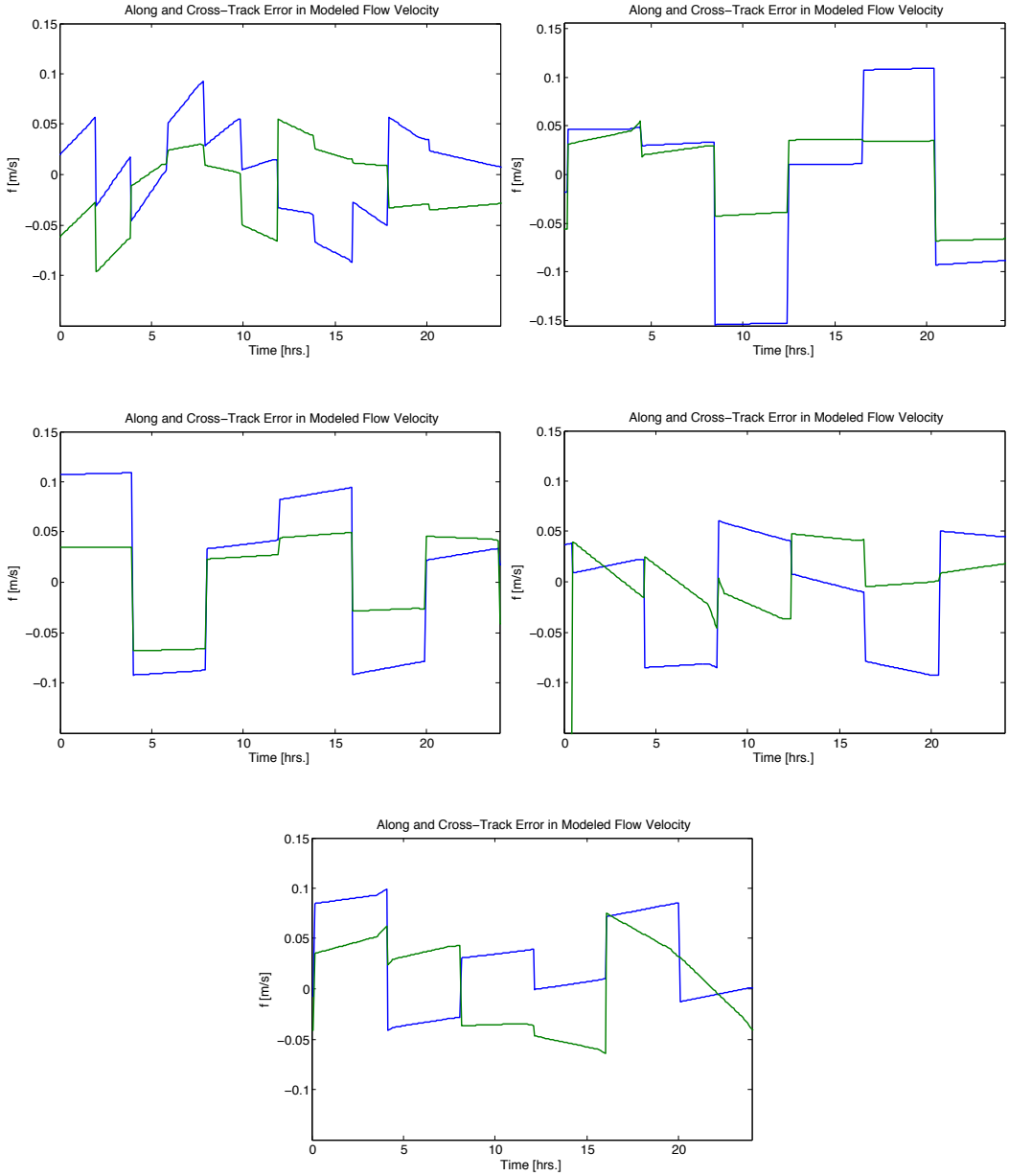

Figure 22: Error in ocean model flow prediction of cross-track (green) and along-track (blue) flow values along three glider transects, in m/sec. Reconstructed flow based on glider on-board depth-averaged flow measurements and ADCIRC tidal flow is used as ground truth.

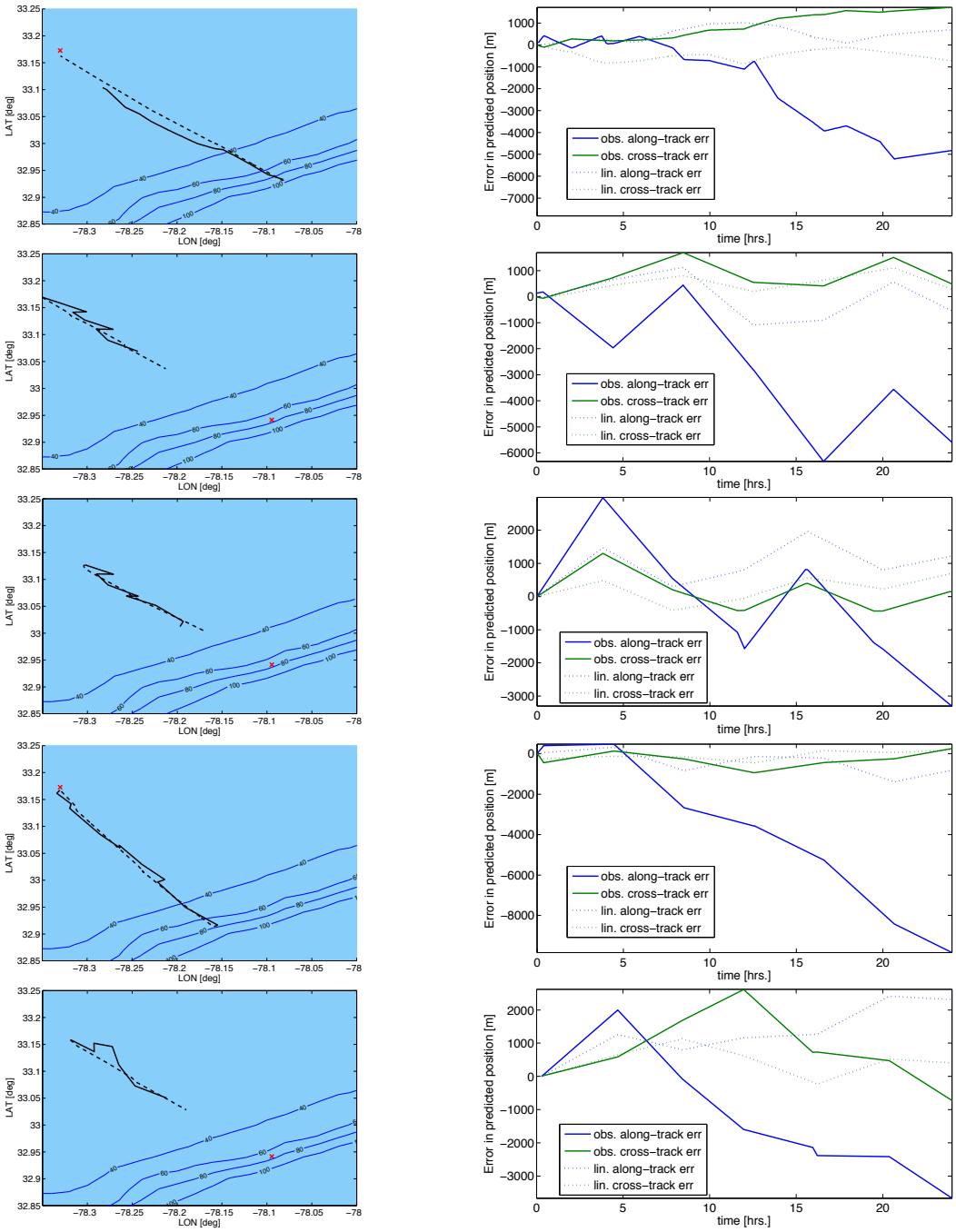

Figure 23: (Left) Trajectories of real (solid line) and virtual (dashed line) station-keeping gliders from a field experiment in Long Bay, SC, in February 2013. (Right) Along-track and cross-track error in predicted glider position over time, observed (solid line) and predicted, based on linearization of error growth equation (dashed line).

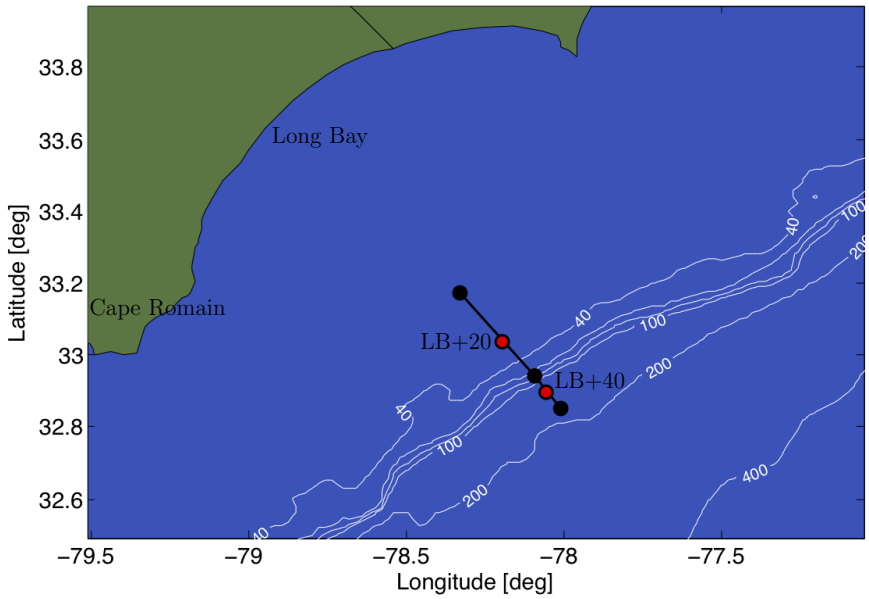

Figure 24: Glider tracks for 2013 follow-up deployment in Long Bay, SC. The deployed glider moved on the transect between positions LB+20 and LB+40, marked by red circles on the map.

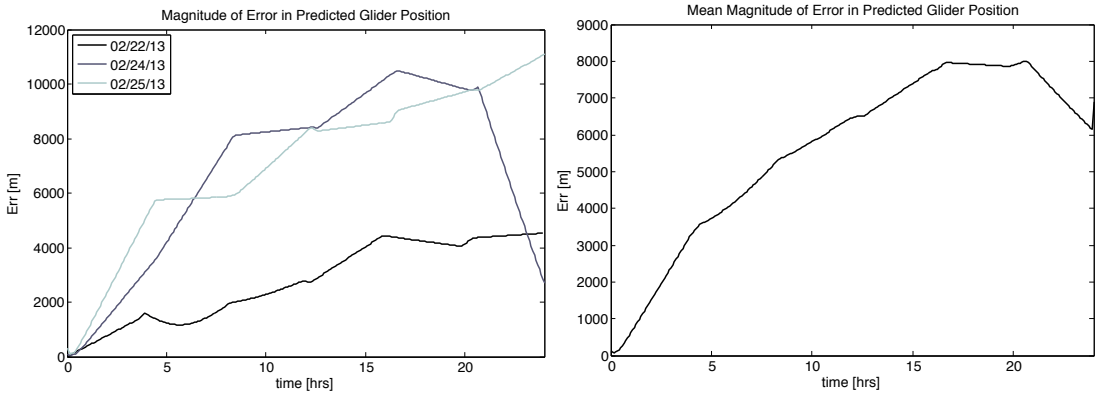

Figure 25: Magnitude of error in simulated glider position over time for three trials run over non-overlapping 24-hour intervals (left), and averaged over the three trials (right).

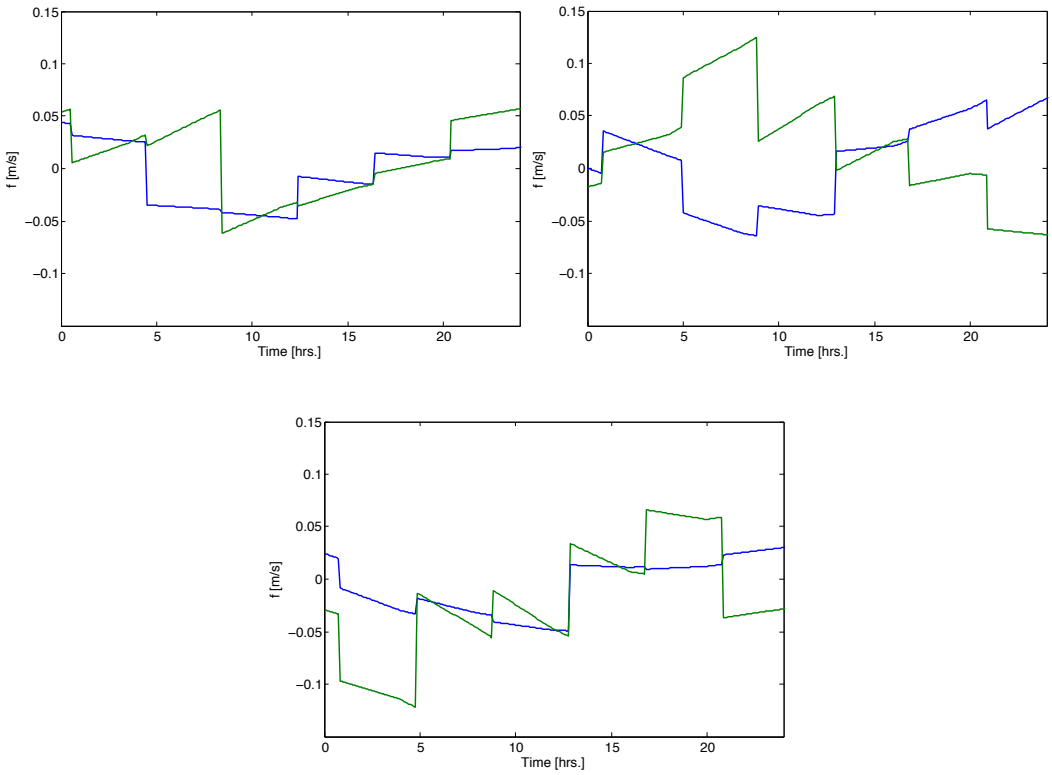

Figure 26: Error in ocean model flow prediction of cross-track (green) and along-track (blue) flow values along three glider transects, in m/sec. Reconstructed flow based on glider on-board depth-averaged flow measurements and ADCIRC tidal flow is used as ground truth.

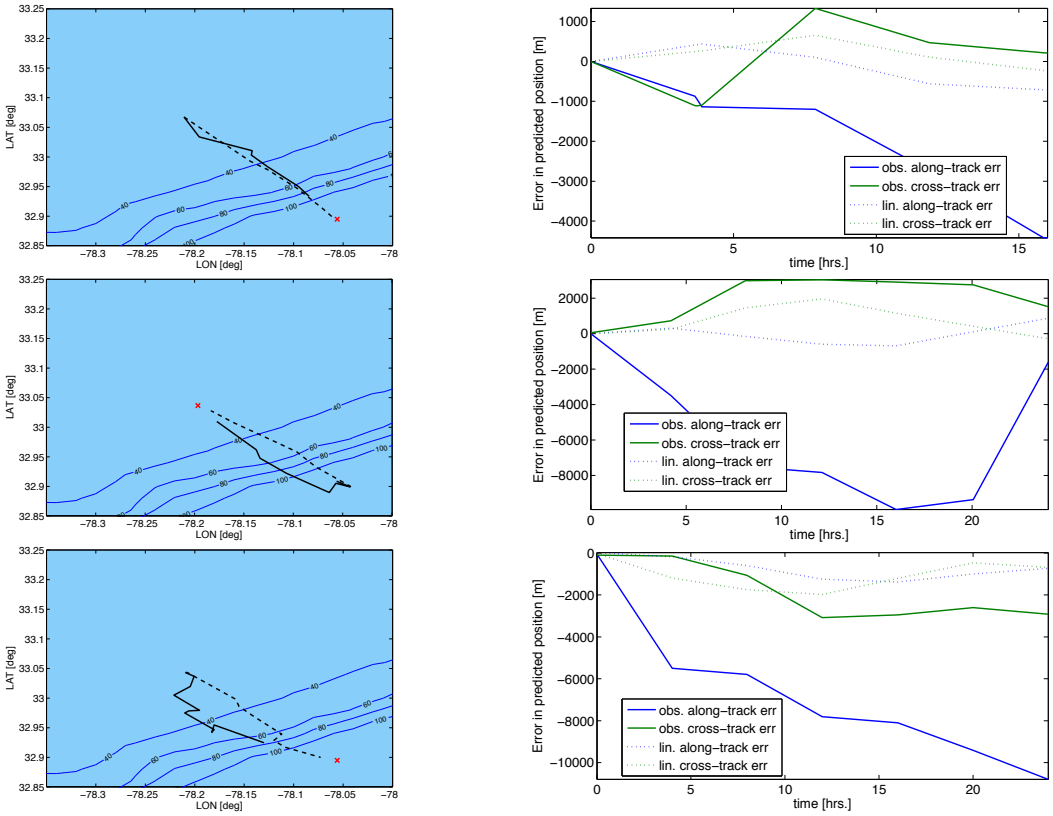

Figure 27: (Left) Trajectories of real (solid line) and virtual (dashed line) station-keeping gliders from a field experiment in Long Bay, SC, in February 2013. (Right) Along-track and cross-track error in predicted glider position over time, observed (solid line) and predicted, based on linearization of error growth equation (dashed line).

CHAPTER 7

CONCLUSION AND FUTURE WORK

This chapter gives a brief review of the work described in this dissertation, and presents a short proposal for related future research directions.

7.1 Conclusion

The main contributions of this dissertation include the derivation of bounds on the growth of error in predicted positions of autonomous underwater vehicles guided by predictive ocean models, under uncertainties in the modeled flow field values; and development of a model for the growth of error in predicted vehicle positions given flow-prediction errors with large-scale spatial structure. The error growth results were verified experimentally in a series of field experiments conduced in Monterey Bay, CA, in 2006, and near Long Bay, SC, in 2012 and 2013. The contributions are summarized in the following bullets:

- *Bounds on growth of error in predicted vehicle position under flow-canceling control:* Expected bounds are computed for error in predicted position of a flow-canceling vehicle with adjustable through-water speed moving in a constant flow field. We have shown that, given a limited-resolution ocean model with Gaussian, zero-mean errors in modeled flow velocity at ocean model gridpoints, the error in predicted vehicle position is approximately 2.5 times the ocean model gridsize.

- *Bounds on growth of cross-track error in predicted vehicle position under transect-following control:* Expected bounds are computed for the cross-track component of error in predicted position of a vehicle with constant through-water speed performing transect-following control with guidance from a predictive ocean model with zero-mean, symmetrically-distributed stochastic errors in flow values at ocean model gridpoints. We show that the cross-track error depends on the ocean model gridsize and increases in time until a steady-state distribution is achieved.

- *Model for growth of error in predicted vehicle position under known continuous perturbations of the modeled ocean flow field:* A model for the growth of error in predicted vehicle position is derived using a first-order Taylor expansion of vehicle dynamics about the modeled vehicle trajectory. This model is used to approximate error growth through complex, time-varying flow fields in the case where error in the modeled ocean flow field can be approximated as a continuous, deterministic function in space and time, as when large-scale flow features are not correctly captured by the ocean model used in the vehicle position prediction. We find an analytic expression for the first-order approximation of error growth in the cross-track direction for the station-keeping controller, under constant flow with constant model bias. In general, error growth depends on the structure of the flow field and the modeling error.

7.2 Future Work

Future work will further explore topics raised during our work on the results presented in this dissertation. Two questions emerge quite naturally from our work on controlled Lagrangian prediction and error modeling:

1. Can data collected by autonomous underwater vehicles be used as feedback in the ocean model to improve the prediction ability for future vehicle trajectories?

2. How does error in predicted vehicle position grow when ambient flow speed matches or exceeds the through-water speed of the vehicle?

The question of using Lagrangian data to improve Eulerian flow models has been around for some time in the field of oceanography; results on assimilation of position data from freely advected floating platforms to improve ocean model flows are presented in [77, 78, 79, 80]. The simulation results in [80] indicate that local errors in modeled flow

values can be minimized by using targeted Lagrangian measurements of individual energetic regions in the flow. Achieving such targeting with freely-advected platforms requires some clever management of deployment times and positions; it can be done much more easily with the use of autonomously controlled vehicles. The energetic regions of the flow are typically characterized by the existence of Lagrangian coherent structures within the flow. We propose to locate and track these structures using local flow measurements from networked groups of autonomous underwater vehicles and to use collected flow data for assimilation back into ocean models. This work will extend the results of Hsieh *at al* on tracking of Lagrangian coherent structures [81].

The use of autonomous vehicles to probe energetic regions in the ocean leads naturally to Question 2. If flow speed matches or exceeds the through-water speed of the vehicle, the vehicle motion depends strongly on the structure of the ambient flow. The future position may be sensitive to the initial position of the vehicle and to small perturbations in the vehicle dynamics in the vicinity of coherent structures. A brief background on these structures is given in the following section.

7.2.1 Coherent Structures in Fluid Flow Fields

The motion of advected particles in fluid flow is frequently chaotic, even in fully deterministic and relatively simple flow fields, so that the separation between neighboring particles grows exponentially over time [79, 80, 82]. As a result, it is often difficult to visually interpret Lagrangian time series data. In such cases, detecting organizing structures which act as repelling or attracting surfaces in the flow can be helpful in understanding the structure of overall motion within the field [83, 82].

Given a time-invariant flow

$$\frac{\mathrm{d}\mathbf{x}}{\mathrm{d}t} = f(\mathbf{x}), \tag{238}$$

the coherent structures can be identified with the stable and unstable manifolds associated with the hyperbolic fixed points of the system dynamics. These manifolds frequently act as

separatrices, partitioning regions characterized by qualitatively different dynamical behavior [82, 84], and give a "skeletal" view of the overall system dynamics.

There is no general consensus in the literature, however, on how coherent structures should be defined for systems with non-autonomous (time-varying) dynamics. There have been several proposed definitions for Lagrangian coherent structures for periodic and quasi-periodic flows, ex. as exponential dichotomies [85] or lobes [86, 87]. In most practical applications, however, the flow has a general aperiodic time variation; furthermore, it may only be available as a discrete data set over a finite time window. In this case, one cannot directly apply analytic results from dynamical systems theory, and there is considerable ambiguity in the definition of organizing coherent structures.

Attempts have been made to characterize coherent structures from both the Eulerian and Lagrangian points of view. The Eulerian approach defines coherent structures as regions of high vorticity [88], maximal vorticity gradient [89], or high vorticity-strain ratio [90, 91, 92, 93]. However, as shown in [94], information derived from the instantaneous velocity field in time-varying systems can give misleading results.

The Lagrangian approach may be understood in terms of the following "physical" definition of Lagrangian coherent structures (LCS) given by George Haller in [95]: "A hyperbolic LCS over a finite time interval ℓ [...] is a locally strongest repelling or attracting material surface over ℓ". In a series of papers published between 1998 and 2001 [96, 97, 98, 99], Haller develops a rigorous definition of LCS that supports the above intuitive understanding of LCS.

The heuristic explanation of LCS is based on the notion of hyperbolicity in dynamical systems theory. A hyperbolic trajectory is one that is locally either repelling or attracting; that is, if the system is linearized about the trajectory, the fundamental solutions of the resulting linear system are all either exponentially growing or decaying.

Characterizing the hyperbolicity of material surfaces in aperiodic flow fields is a matter

that has been treated in a number of ways. Haller's early analysis was based on examining the instantaneous stable and unstable manifolds associated with hyperbolic stagnation points in a flow; hyperbolic trajectories of the time-varying system were derived by adding slow time variation to the instantaneous dynamics [96]. A similar approach is taken by K. Ide *et al* in [94]. Ide's paper presents a method for computing "distinguished hyperbolic trajectories" in time-varying flow using the notion of exponential dichotomies. In [97], on the other hand, LCS are defined as material lines with locally maximal hyperbolicity times. Other alternative measures of hyperbolicity have been used to define LCS in the literature, including the finite-size Lyapunov exponent (FSLE), which measures the time necessary for neighboring particles to reach a given separation [100, 101, 102], and the finite-strain field [103]. A computationally convenient definition of the LCS in terms of the finite time Lyapunov exponent field is suggested by Haller in [99] and further developed by S. C. Shadden *et al* in [104, 82] and by F. Lekien *et al* in [105]. This is the definition which will be used in the proposed work.

Lyapunov exponents may be used to characterize the stability of trajectories of nonlinear systems, as well as to note the emergence of chaos, provided that the system being analyzed satisfies certain regularity conditions [106, 107]. In classical systems theory, the Lyapunov exponent is defined as the exponential expansion/contraction rate about a trajectory of a possibly nonlinear system [106]. Finding the Lyapunov exponent requires that the system be integrable and known for all time; this is often not true for ocean flows, which are computed using numerical models over a finite time horizon. The finite-time Lyapunov exponent (FTLE) is a generalization of the Lyapunov exponent and is defined as the exponential expansion rate about a system trajectory over a finite time window [104]. The FTLE measures the amount of "stretching" of neighboring particles about a given trajectory over a finite time window.

For computational purposes, the LCS may be defined as local maxima, or ridges in the FTLE field [104, 82, 105, 83, 108]. The LCS computed in this way generally agree

well with the material surfaces of maximal expansion/contraction described by Haller [82], however [95] presents a number of important counterexamples. An important problem is that ridges in the FTLE may correspond to trajectories with locally maximal shear (that is, stretching along the trajectory), while in most applications, one is interested in the stretching normal to the trajectory. Therefore, when computing LCS, one should verify that ridges in the FTLE field correspond to maxima in the normal expansion/contraction.

In spite of the various technical challenges associated with defining coherent structures in a general time-varying flow field, these structures can be very useful in revealing the framework of mixing and transport in the flow. Moreover, coherent structures derived from Lagrangian particle trajectories are quite robust to discretization of the flow data and integration schemes used to simulate Lagrangian particles [97, 109, 105, 83, 82, 110]. Robustness results are explicitly derived in [84], in which it is shown that computations of LCS are robust to short-duration perturbations in the flow field, even while Lagrangian particle trajectories deviate exponentially from the unperturbed trajectories.

7.2.2 Future Work Plan

Autonomous vehicles will be used to sample along coherent structures in the flow. A small network of autonomous surface vehicles will be used to identify and track Lagrangian coherent structures (LCS) in ocean flow fields using data from both predictive ocean models and local measurements. In the second part of the future work, a swarm of networked autonomous vehicles will be used to continuously monitor a user-specified area of interest in the ocean. Vehicle density over the area will be modeled and energy-efficient control strategies will be designed to maintain a desired distribution of vehicles. In both parts of the proposed work, the effects of ambient flow on vehicle motion will be taken into account, and of limits on communication such as range restrictions, noise, and packet loss.

CHAPTER 8

PUBLICATIONS

[1] K. Szwaykowska and F. Zhang, "Trend and Bounds for Error Growth in Controlled Lagrangian Particle Tracking," *IEEE Journal of Oceanic Engineering (in print, available online)*.

[2] K. Szwaykowska and F. Zhang, "Controlled Lagrangian Particle Tracking Error Under Biased Flow Prediction," *Proc. 2013 American Control Conference*, 2013.

[3] K. Szwaykowska and F. Zhang, "A lower bound on navigation error for marine robots guided by ocean circulation models," *2011 IEEE/RSJ International Conference on Intelligent Robots and Systems*, pp. 3583-3588, 2011.

[4] K. Szwaykowska and F. Zhang, "A lower bound for controlled Lagrangian particle tracking error," *49th IEEE Conference on Decision and Control (CDC)*, pp. 4353-4358, 2010.

[5] K. Szwaykowska, F. Zhang, and W. Wolf, "Tracking Error under Time Delay and Asynchronicity in Distributed Camera Systems," *Proc. 2009 American Control Conference (ACC 2009)*, pp. 4886-4891, 2009.

[6] F. Zhang, K. Szwaykowska, V. Mooney, and W. Wolf, "Task Scheduling for Control Oriented Requirements for Cyber-Physical Systems," *Proc. IEEE Real-Time Systems Symposium*, pp. 47-56, 2008.

CHAPTER 9

APPENDICES

9.1 Appendix A: Notation

AUV	Autonomous Underwater Vehicle
$\mathcal{D}$	Spatial domain of vehicle position, $\mathcal{D} \subset \mathbb{R}^2$
$\mathbf{F}_M$	Modeled value of deterministic component of ocean flow in the random-flight model
$\mathbf{F}_R$	True value of deterministic component of ocean flow in the random-flight model
$\mathbf{f}$	Error in modeled value of deterministic component of ocean flow ($\mathbf{f} \triangleq \mathbf{F}_R - \mathbf{F}_M$)
iid	Independent, identically distributed (used in reference to random variables)
ℓ	For transect-following controller, ℓ denotes the transect
$\mathbf{N}$	Unit vector pointing normal to the transect (in transect-following controller) or normal to the direction of the station-keeping goal (station-keeping controller)
$\mathbf{p}$	For transect-following controller, an arbitrary point on the transect
$\mathbf{Pr}(X)$	Probability of event X
$\mathbb{R}$	Set of real numbers
$s(\zeta, t)$	AUV speed at position $\zeta \in \mathbb{R}^2$ and time $t \in \mathbb{R}$
$\mathbf{T}$	Unit vector pointing along the transect (in transect-following controller) or in the direction of the station-keeping goal (station-keeping controller)
$\mathbf{u}(\zeta, t)$	Control input (commanded heading, speed, etc.) at position $\zeta \in \mathbb{R}^2$ and time $t \in \mathbb{R}$
$\mathbf{v}(\zeta, t)$	Throughwater speed of AUV at position $\zeta \in \mathbb{R}^2$ and time $t \in \mathbb{R}$
$\mathbf{x}$	Position of AUV
$\mathbb{Z}$	Set of all integers
$\mathbf{z}$	Predicted position of AUV
ν	Stochastic component of ocean flow in the random-flight model
ξ	Used to denote stochastic values of error in modeled flow values at ocean model gridpoints
$\rho(\cdot)$	Used to denote probability density function (pdf)

REFERENCES

[1] E. Ferreira-Coelho and M. Rixen, "Maritime rapid environmental assessment new trends in operational oceanography," *Journal of Marine Systems*, vol. 69, pp. 1–2, Jan. 2008.

[2] M. Ghil and P. Malanotte-Rizzoli, "Data assimilation in meteorology and oceanography," *Advances in Geophysics*, vol. 33, pp. 141–266, 1991.

[3] G. Korres, I. Hoteit, and G. Triantafyllou, "Data assimilation into a Princeton Ocean Model of the Mediterranean Sea using advanced Kalman filters," *Journal of Marine Systems*, vol. 65, pp. 84–104, Mar. 2007.

[4] N. E. Leonard, "Cooperative vehicle environmental monitoring," in *Handbook of Ocean Engineering, Part B: Autonomous Ocean Vehicles, Systems and Control* (T. B. Curtin, ed.), ch. 9, New York, New York, USA: Springer, 2013.

[5] D. L. Rudnick, R. E. Davis, C. C. Eriksen, D. M. Fratantoni, and M. J. Perry, "Underwater gliders for ocean research," *Marine Technology Society Journal*, vol. 38, pp. 73–84, June 2004.

[6] D. R. Thompson, S. Chien, M. Arrott, A. Balasuriya, Y. Chao, P. P. Li, M. Meisinger, S. Petillo, and O. Schofield, "Mission planning in a dynamic ocean Sensorweb," in *ICAPS SPARK*, vol. 91109, 2009.

[7] T. Inanc, S. C. Shadden, and J. E. Marsden, "Optimal trajectory generation in ocean flows," in *Proceedings of the 2005 American Control Conference*, no. 2, pp. 674–679, IEEE, 2005.

[8] R. N. Smith, Y. Chao, P. P. Li, D. A. Caron, B. H. Jones, and G. S. Sukhatme, "Planning and implementing trajectories for autonomous underwater vehicles to track evolving ocean processes based on predictions from a regional ocean model," *International Journal of Robotics Research*, vol. 29, pp. 1475–1497, Aug. 2010.

[9] R. N. Smith, A. Pereira, P. P. Li, D. A. Caron, B. H. Jones, and G. S. Sukhatme, "Autonomous underwater vehicle trajectory design coupled with predictive ocean models: a case study," in *2010 IEEE International Conference on Robotics and Automation*, pp. 4770–4777, Ieee, May 2010.

[10] J. J. Leonard, A. A. Bennett, C. M. Smith, and H. J. S. Feder, "Autonomous underwater vehicle navigation," 1998.

[11] B. Garau, M. Bonet, A. Alvarez, and S. Ruiz, "Path planning for autonomous underwater vehicles in realistic oceanic current fields: application to gliders in the western Mediterranean Sea," *Journal of Maritime Research*, vol. 6, no. 2, pp. 5–22, 2009.

[12] J. G. Graver, *Underwater gliders: dynamics, control and design*. Phd, Princeton University, 2005.

[13] H. Lamb, *Hydrodynamics*. Cambridge: Cambridge University Press, 1895.

[14] R. Lumpkin and M. Pazos, "Measuring surface currents with Surface Velocity Program drifters: the instrument, its data, and some recent results," in *Lagrangian Analysis and Prediction of Coastal and Ocean Dynamics* (A. Mariano, T. Rossby, and D. Kirwan, eds.), ch. 2, Cambridge: Cambridge University Press, 2001.

[15] J. W. Dippner, "Mathematical modeling of the transport of pollution in water," in *Hydrological Systems Modeling* (L. S. Kuchment and V. P. Singh, eds.), vol. II, EOLSS Publishers Co Ltd, 2009.

[16] T. M. Özgökmen, A. Griffa, A. J. Mariano, and L. I. Piterbarg, "On the predictability of Lagrangian trajectories in the ocean," *Journal of Atmospheric and Oceanic Technology*, vol. 17, pp. 366–383, Mar. 2000.

[17] F. Hubacz, "NOAA Teacher at Sea Blog Online at http://teacheratsea.wordpress.com/tag/heterotrophic/," 2013.

[18] M. Gomez-Gesteira, P. Montero, R. Prego, J. J. Taboada, P. Leitao, M. Ruiz-Villarreal, R. Neves, and V. Perez-Villar, "A two-dimensional particle tracking model for pollution dispersion in A Coruña and Vigo Rias (NW Spain)," *Oceanologica Acta*, vol. 22, pp. 167–177, Mar. 1999.

[19] M. Cerejo and J. M. Dias, "Tidal transport and dispersal of marine toxic microalgae in a shallow, temperate coastal lagoon," *Marine environmental research*, vol. 63, pp. 313–40, May 2007.

[20] H. Havens, M. E. Luther, S. D. Meyers, and C. A. Heil, "Lagrangian particle tracking of a toxic dinoflagellate bloom within the Tampa Bay estuary," *Marine pollution bulletin*, vol. 60, pp. 2233–41, Dec. 2010.

[21] A. Lugo-Fernandez, K. J. P. Deslarzes, J. M. Price, G. S. Boland, and M. V. Morin, "Inferring probable dispersal of Flower Garden Banks Coral Larvae (Gulf of Mexico) using observed and simulated drifter trajectories," *Continental Shelf Research*, vol. 21, no. 1, pp. 47–67, 2001.

[22] E. Staaterman, C. B. Paris, and J. Helgers, "Orientation behavior in fish larvae: a missing piece to Hjort's critical period hypothesis.," *Journal of theoretical biology*, vol. 304, pp. 188–96, July 2012.

[23] L. C.-M. Lebreton, S. D. Greer, and J. C. Borrero, "Numerical modelling of floating debris in the world's oceans," *Marine pollution bulletin*, vol. 64, pp. 653–61, Mar. 2012.

[24] A. Griffa, "Applications of stochastic particle models to oceanographic problems," in *Stochastic Modeling in Physical Oceanography* (R. J. Adler, P. Müller, and B. Rozovskii, eds.), pp. 113–140, Boston: Birkhäuser, 1996.

[25] G. I. Taylor, "Diffusion by continuous movements," *Proceedings of the London Mathematical Society*, vol. 20, pp. 373—-416, Jan. 1921.

[26] F. B. Smith, "Conditioned particle motion in a homogeneous turbulent field," *Atmospheric Environment*, vol. 2, no. 5, pp. 491–508, 1968.

[27] H. van Dop, F. T. M. Nieuwstadt, and J. C. R. Hunt, "Random walk models for particle displacements in inhomogeneous unsteady turbulent flows," *Physics of Fluids*, vol. 28, no. 6, pp. 1639–1653, 1985.

[28] D. J. Thomson, "A random walk model of dispersion in turbulent flows and its application to dispersion in a valley," *Quarterly Journal of the Royal Meteorological Society*, vol. 112, pp. 511–530, Apr. 1986.

[29] B. L. Sawford, "Reynolds number effects in Lagrangian stochastic models of turbulent dispersion," *Physics of Fluids A: Fluid Dynamics*, vol. 3, no. 6, pp. 1577–1586, 1991.

[30] I. Benczik, Z. Toroczkai, and T. Tél, "Selective sensitivity of open chaotic flows on inertial tracer advection: catching particles with a stick," *Physical Review Letters*, vol. 89, pp. 14–17, Sept. 2002.

[31] A. C. Haza, L. I. Piterbarg, P. Martin, T. M. Özgökmen, and A. Griffa, "A Lagrangian subgridscale model for particle transport improvement and application in the Adriatic Sea using the Navy Coastal Ocean Model," *Ocean Modelling*, vol. 17, pp. 68–91, Jan. 2007.

[32] A. Griffa, L. I. Piterbarg, and T. M. Özgökmen, "Predictability of Lagrangian particle trajectories: effects of smoothing of the underlying Eulerian flow," *Journal of Marine Research*, vol. 62, pp. 1–35, Jan. 2004.

[33] C. V. Caldwell, *A Sampling-Based Model Predictive Control Approach to Motion Planning for Autonomous Underwater Vehicles*. Doctoral dissertation, Florida State University, 2011.

[34] G. Marafioti, R. B. Bitmead, and M. Hovd, "Model Predictive Control with State Dependent Input Weight: An Application to Underwater Vehicles," in *Proceedings of the 17th IFAC World Congress* (C. Myung, ed.), pp. 15979–15984, July 2008.

[35] L. Medagoda and S. B. Williams, "Model predictive control of an autonomous underwater vehicle in an in situ estimated water current profile," in *2012 Oceans - Yeosu*, pp. 1–8, IEEE, May 2012.

[36] A. Molero, R. Dunia, J. Cappelletto, and G. Fernandez, "Model predictive control of remotely operated underwater vehicles," in *IEEE Conference on Decision and Control and European Control Conference*, pp. 2058–2063, Ieee, Dec. 2011.

[37] W. Naeem, R. Sutton, J. Chudley, F. R. Dalgleish, and S. Tetlow, "A genetic algorithm-based model predictive control autopilot design and its implementation in an autonomous underwater vehicle," *Proceedings of the Institution of Mechanical Engineers, Part M: Journal of Engineering for the Maritime Environment*, vol. 218, pp. 175–188, Jan. 2004.

[38] D. Q. Mayne, J. B. Rawlings, C. V. Rao, and P. O. M. Scokaert, "Constrained model predictive control: stability and optimality," *Automatica*, vol. 36, pp. 789–814, 2000.

[39] A. Jadbabaie, *Receding Horizon Control of Nonlinear Systems: A Control Lyapunov Function Approach*. PhD thesis, California Institute of Technology, 2000.

[40] D. A. Paley, *Cooperative control of collective motion for ocean sampling with autonomous vehicles*. Phd thesis, Princeton University, 2007.

[41] D. A. Paley, F. Zhang, and N. E. Leonard, "Cooperative control for ocean sampling: the Glider Coordinated Control System," *IEEE Transactions on Control Systems Technology*, vol. 16, pp. 735–744, July 2008.

[42] B. Garau, A. Alvarez, and G. Oliver, "Path planning of autonomous underwater vehicles in current fields with complex spatial variability: an A* approach," in *Proceedings of the 2005 IEEE International Conference on Robotics and Automation*, no. April, pp. 194–198, IEEE, 2005.

[43] C. Pêtrès, Y. Pailhas, P. Patrón, Y. Petillot, J. Evans, and D. Lane, "Path planning for autonomous underwater vehicles," *IEEE Transactions on Robotics*, vol. 23, pp. 331–341, Apr. 2007.

[44] M. Soulignac, P. Taillibert, and M. Rueher, "Adapting the wavefront expansion in presence of strong currents," in *2008 IEEE International Conference on Robotics and Automation*, vol. 2008, pp. 1352–1358, IEEE, May 2008.

[45] M. Soulignac, P. Taillibert, and M. Rueher, "Time-minimal path planning in dynamic current fields," in *2009 IEEE International Conference on Robotics and Automation*, pp. 2473–2479, IEEE, May 2009.

[46] W. Zhang, T. Inanc, S. Ober-bl, and J. E. Marsden, "Optimal trajectory generation for a glider in time-varying 2D ocean flows B-spline model," in *2008 IEEE International Conference on Robotics and Automation*, (Pasadena, CA), pp. 1083–1088, 2008.

[47] K. Sugihara and J. Yuh, "GA-based motion planning for underwater robotic vehicles," in *Proc. 10th International Symp. on Unmanned Untethered Submersible Technology*, pp. 406–415, 1996.

[48] J. C. Rubio and S. Kragelund, "The trans-pacific crossing: long range adaptive path planning for UAVs through variable wind fields," in *22nd Digital Avionics Systems Conference Proceedings (Cat No 03CH37449) DASC-03*, vol. 2, pp. 8.B.4–1–12, IEEE, 2003.

[49] A. Alvarez, A. Caiti, and R. Onken, "Evolutionary path planning for autonomous underwater vehicles in a variable ocean," *IEEE Journal of Oceanic Engineering*, vol. 29, no. 2, pp. 418–429, 2004.

[50] C. Vasudevan and K. Ganesan, "Case-based path planning for autonomous underwater vehicles," *Autonomous Robots*, vol. 3, no. 2-3, pp. 79–89, 1996.

[51] M. Greytak and F. S. Hover, "Analytic error variance predictions for planar vehicles," *2009 IEEE International Conference on Robotics and Automation*, pp. 471–476, May 2009.

[52] M. Greytak and F. S. Hover, "Motion planning with an analytic risk cost for holonomic vehicles," *Proceedings of the 48h IEEE Conference on Decision and Control (CDC) held jointly with 2009 28th Chinese Control Conference*, pp. 5655–5660, Dec. 2009.

[53] R. Grasso, D. Cecchi, M. Cococcioni, C. Trees, M. Rixen, A. Alvarez, and C. Strode, "Model based decision support for underwater glider operation monitoring," in *Oceans 2010 MTS/IEEE Seattle*, pp. 1–8, Ieee, Sept. 2010.

[54] L. Blackmore, "A Probabilistic Particle Control Approach to Optimal, Robust Predictive Control," in *Proceedings of the AIAA Guidance, Navigation and Control Conference*, no. 10, 2006.

[55] L. Blackmore and B. C. Williams, "Optimal, Robust Predictive Control of Nonlinear Systems under Probabilistic Uncertainty using Particles," in *2007 American Control Conference*, pp. 1759–1761, Ieee, July 2007.

[56] R. Bachmayer, N. E. Leonard, J. G. Graver, E. Fiorelli, P. Bhatta, and D. A. Paley, "Underwater gliders: recent developments and future applications," in *IEEE International Symposium on Underwater Technology*, 2004.

[57] S. X. Wang, X. J. Sun, J. G. Wu, X. M. Wang, and H. W. Zhang, "Motion characteristic analysis of a hybrid-driven underwater glider," in *Oceans 2010 IEEE Sydney*, pp. 1–9, IEEE, May 2010.

[58] I. Khalid and M. R. Arshad, "Motion simulation for propeller-driven USM underwater glider with controllable wings and rudder," in *2nd International Conference on Instrumentation Control and Automation*, no. November, pp. 316–321, 2011.

[59] J. Yuh and M. West, "Underwater robotics," *Advanced Robotics*, vol. 15, no. 5, pp. 609–639, 2001.

[60] "Autonomous Undersea Vehicle Applications Center Database. Online: http://auvac.org/explore-database," 2013.

[61] C. C. Eriksen, T. J. Osse, R. D. Light, T. Wen, T. W. Lehman, P. L. Sabin, J. W. Ballard, and A. M. Chiodi, "Seaglider: a long-range autonomous underwater vehicle for oceanographic research," *IEEE Journal of Oceanic Engineering*, vol. 26, no. 4, pp. 424–436, 2001.

[62] R. McEwen, H. Thomas, D. Weber, and F. Psota, "Performance of an AUV navigation system at Arctic latitudes," *IEEE Journal of Oceanic Engineering*, vol. 30, pp. 443–454, Apr. 2005.

[63] S. D. McPhail, M. E. Furlong, J. R. Perrett, P. Stevenson, A. Webb, D. White, and M. Pebody, "Exploring beneath the PIG Ice Shelf with the Autosub3 AUV," in *OCEANS 2009-EUROPE*, no. January, pp. 1–8, IEEE, May 2009.

[64] N. E. Leonard, D. A. Paley, R. E. Davis, D. M. Fratantoni, F. Lekien, and F. Zhang, "Coordinated control of an underwater glider fleet in an adaptive ocean sampling field experiment in Monterey Bay," *Journal of Field Robotics*, vol. 27, pp. 718–740, Nov. 2010.

[65] J. Kohut, D. Aragon, L. Creed, J. Graver, C. Haldeman, J. Kerfoot, H. Roarty, C. Jones, D. Webb, and S. Glenn, "Slocum Gliders: Robust and Ready," *Journal of Field Robotics*, vol. 24, no. 6, pp. 473–485, 2007.

[66] R. N. Smith, Y. Chao, B. H. Jones, D. A. Caron, P. P. Li, and G. S. Sukhatme, "Trajectory design for autonomous underwater vehicles based on ocean model predictions for feature tracking," in *Proceedings of the 7th International Conference on Field and Service Robotics*, (Cambridge, MA), pp. 1–10, 2009.

[67] J. Das, K. Rajan, S. Frolov, F. Py, J. Ryan, D. A. Caron, and G. S. Sukhatme, "Towards marine bloom trajectory prediction for AUV mission planning," *2010 IEEE International Conference on Robotics and Automation*, pp. 4784–4790, 2010.

[68] P. Bhatta, E. Fiorelli, F. Lekien, N. E. Leonard, D. A. Paley, F. Zhang, R. Bachmayer, D. M. Fratantoni, R. E. Davis, and R. J. Sepulchre, "Coordination of an underwater glider fleet for adaptive sampling," in *Proceedings of the International Workshop on Underwater Robotics*, no. August, pp. 61–69, 2005.

[69] F. Zhang, D. M. Fratantoni, D. A. Paley, J. M. Lund, and N. E. Leonard, "Control of coordinated patterns for ocean sampling," *International Journal of Control*, vol. 80, pp. 1186–1199, July 2007.

[70] N. E. Leonard, D. A. Paley, F. Lekien, R. J. Sepulchre, D. M. Fratantoni, and R. E. Davis, "Collective motion, sensor networks, and ocean sampling," *Proceedings of the IEEE*, vol. 95, pp. 48–74, Jan. 2007.

[71] P. Falco, A. Griffa, P.-M. Poulain, and E. Zambianchi, "Transport properties in the Adriatic Sea as deduced from drifter data," *Journal of Physical Oceanography*, vol. 30, pp. 2055–2071, Aug. 2000.

[72] H. K. Khalil, *Nonlinear Systems*. Upper Saddle River, NJ: Pearson Education International Inc., 3 ed., 2000.

[73] T. W. Research, "Slocum G2 Glider Operators Manual," 2012.

[74] F. P. Bretherton, R. E. Davis, and C. Fandry, "A technique for objective analysis and design of oceanographic experiments applied to MODE-73," *Deep Sea Research and Oceanographic Abstracts*, vol. 23, pp. 559–582, July 1976.

[75] T. N. Lee and D. A. Brooks, "Initial observations of current, temperature, and coastal sea level response to atmospheric and Gulf Stream forcing on the Georgia shelf," *Geophysical Research Letters*, vol. 6, no. 4, 1979.

[76] B. O. Blanton, "Barotropic tides in the South Atlantic Bight," *Journal of Geophysical Research*, vol. 109, no. C12, 2004.

[77] L. Kuznetsov, K. Ide, and C. K. R. T. Jones, "A method for assimilation of lagrangian data," *Monthly Weather Review*, vol. 131, pp. 2247–2260, Dec. 2003.

[78] A. J. Mariano, A. Griffa, T. M. Özgökmen, and E. Zambianchi, "Lagrangian analysis and predictability of coastal and ocean dynamics 2000," *Journal of Atmospheric and Oceanic Technology*, vol. 19, no. 7, pp. 1114–1126, 2002.

[79] H. Salman, L. Kuznetsov, C. K. R. T. Jones, and K. Ide, "A method for assimilating Lagrangian data into a shallow-water-equation ocean model," *Monthly Weather Review*, vol. 134, pp. 1081–1101, Apr. 2006.

[80] H. Salman, K. Ide, and C. K. R. T. Jones, "Using flow geometry for drifter deployment in Lagrangian data assimilation," *Tellus A*, vol. 60, pp. 321–335, Mar. 2008.

[81] M.-y. A. Hsieh, E. Forgoston, T. W. Mather, and I. B. Schwartz, "Robotic manifold tracking of coherent structures in flows," 2012.

[82] S. C. Shadden, "Lagrangian coherent structures," in *Transport and Mixing in Laminar Flows: From Microfluidics to Oceanic Currents* (R. Grigoriev, ed.), no. 1, pp. 1–29, Wiley-VCH, 2011.

[83] P. C. du Toit and J. E. Marsden, "Horseshoes in hurricanes," *Journal of Fixed Point Theory and Applications*, vol. 7, pp. 351–384, Sept. 2010.

[84] G. Haller, "Lagrangian coherent structures from approximate velocity data," *Physics of Fluids*, vol. 14, no. 6, pp. 1851–1861, 2002.

[85] A. M. Mancho, D. Small, S. Wiggins, and K. Ide, "Computation of stable and unstable manifolds of hyperbolic trajectories in two-dimensional, aperiodically time-dependent vector fields," *Physica D: Nonlinear Phenomena*, vol. 182, pp. 188–222, Aug. 2003.

[86] P. D. Miller, C. K. R. T. Jones, A. M. Rogerson, and L. J. Pratt, "Quantifying transport in numerically generated velocity fields," *Physica D: Nonlinear*, vol. 110, pp. 105–122, 1997.

[87] A. M. Rogerson, P. D. Miller, and L. J. Pratt, "Lagrangian motion and fluid exchange in a barotropic meandering jet," *Journal of Physical Oceanography*, vol. 29, no. 10, pp. 2635–2655, 1999.

[88] R. Benzi, S. Patarnello, and P. Santangelo, "Self-similar coherent structures in two-dimensional decaying turbulence," *Journal of Physics A: Mathematical and General*, vol. 21, pp. 1221–1237, Mar. 1988.

[89] M. N. Juckes and M. E. McIntyre, "A high-resolution one-layer model of breaking planetary waves in the stratosphere," *Nature*, vol. 328, no. 13, pp. 590–596, 1987.

[90] J. C. McWilliams, "The emergence of isolated coherent vortices in turbulent flow," *Journal of Fluid Mechanics*, vol. 146, pp. 21–43, Apr. 1984.

[91] M. E. Brachet, M. Meneguzzi, H. Politano, and P. L. Sulem, "The dynamics of freely decaying two-dimensional turbulence," *Journal of Fluid Mechanics*, vol. 194, pp. 333–349, Apr. 1988.

[92] J. Weiss, "The dynamics of enstrophy transfer in two-dimensional hydrodynamics," *Physica D: Nonlinear Phenomena*, vol. 48, pp. 273–294, Mar. 1991.

[93] C. Basdevant and T. Philipovitch, "On the validity of the Weiss criterion in two-dimensional turbulence," *Physica D: Nonlinear Phenomena*, vol. 73, pp. 17–30, May 1994.

[94] K. Ide, D. Small, and S. Wiggins, "Distinguished hyperbolic trajectories in time-dependent fluid flows: analytical and computational approach for velocity fields defined as data sets," *Nonlinear Processes in Geophysics*, vol. 9, no. 3/4, pp. 237–263, 2002.

[95] G. Haller, "A variational theory of hyperbolic Lagrangian coherent structures," *Physica D: Nonlinear Phenomena*, vol. 240, pp. 574–598, Mar. 2011.

[96] G. Haller and A. C. Poje, "Finite time transport in aperiodic flows," *Physica D: Nonlinear Phenomena*, vol. 119, pp. 352–380, Aug. 1998.

[97] G. Haller and G. Yuan, "Lagrangian coherent structures and mixing in two-dimensional turbulence," *Physica D: Nonlinear Phenomena*, vol. 147, pp. 352–370, Dec. 2000.

[98] G. Haller, "Finding finite-time invariant manifolds in two-dimensional velocity fields," *Chaos*, vol. 10, pp. 99–108, Mar. 2000.

[99] G. Haller, "Distinguished material surfaces and coherent structures in three-dimensional fluid flows," *Physica D: Nonlinear Phenomena*, vol. 149, pp. 248–277, Mar. 2001.

[100] T.-Y. Koh and B. Legras, "Hyperbolic lines and the stratospheric polar vortex," *Chaos*, vol. 12, pp. 382–394, June 2002.

[101] E. Aurell, G. Boffetta, A. Crisanti, G. Paladin, and A. Vulpiani, "Predictability in the large: an extension of the concept of Lyapunov exponent," *Journal of Physics A: Mathematical and General*, vol. 30, pp. 1–26, Jan. 1997.

[102] F. D'Ovidio, V. Fernández, E. Hernández-García, and C. López, "Mixing structures in the Mediterranean Sea from finite-size Lyapunov exponents," *Geophysical Research Letters*, vol. 31, pp. 1–4, Sept. 2004.

[103] K. P. Bowman, "Manifold geometry and mixing in observed atmospheric flows," 1999.

[104] S. C. Shadden, F. Lekien, and J. E. Marsden, "Definition and properties of Lagrangian coherent structures from finite-time Lyapunov exponents in two-dimensional aperiodicflows," *Physica D: Nonlinear Phenomena*, vol. 212, pp. 271–304, Dec. 2005.

[105] F. Lekien, S. C. Shadden, and J. E. Marsden, "Lagrangian coherent structures in n-dimensional systems," *Journal of Mathematical Physics*, vol. 48, no. 6, p. 065404, 2007.

[106] L. Barreira and Y. B. Pesin, *Lyapunov exponents and smooth ergodic theory*. Providence, Rhode Island: American Mathematical Society, 2001.

[107] G. A. Leonov and N. V. Kuznetsov, "Time-varying linearization and the perron effects," *International Journal of Bifurcation and Chaos*, vol. 17, no. 04, pp. 1079–1107, 2007.

[108] M. Mathur, G. Haller, T. Peacock, J. Ruppert-Felsot, and H. Swinney, "Uncovering the Lagrangian skeleton of turbulence," *Physical Review Letters*, vol. 98, pp. 1–4, Apr. 2007.

[109] G. Haller, "Lagrangian structures and the rate of strain in a partition of two-dimensional turbulence," *Physics of Fluids A*, vol. 13, no. 11, pp. 3365–3385, 2001.

[110] M. Farazmand and G. Haller, "Computing Lagrangian coherent structures from their variational theory," *Chaos*, vol. 22, Mar. 2012.